Measurement of the cross-section for b jets produced in association with a Z boson at $\sqrt{s}$ = 7 TeV with the ATLAS detector

Thesis submitted in accordance with the requirements of
the University of Liverpool for the degree of Doctor in Philosophy
by

Aaron Colin Bundock

September 2013

For my parents Colin and Jenny, who have provided endless support, inspiration, and love

"Physics has at its essence the study of the symmetries observed in nature, and these symmetries, in turn, give rise to conservation laws and the properties of particles. Yet these symmetries are not enough, for without the breaking of symmetries, there would not be a universe that could observe them."

- A. Greentree

Abstract

In this thesis, 4.7 fb^{-1} of data taken in 2011 by the ATLAS Experiment of proton-proton collisions at $\sqrt{s}$ = 7 TeV delivered by the Large Hadron Collider at CERN is used to measure the integrated and differential cross sections for the production of electroweak Z bosons in associaton with b quark jets. Z bosons are identified by reconstructing the electron and muon decay modes, and the fraction of b quark jets in the Z sample is estimated by fitting the neural network output of a specialised heavy flavour tagging algorithm in data with light + charm and bottom flavour templates derived from Monte Carlo simulation. The integrated $Z + b$ jet cross section is measured to be 5.04 $\pm$ 0.17 stat $\pm$ 0.83 syst pb. The ratio of the integrated $Z + b$ jet cross section to the inclusive Z production cross section is measured to be (5.26 $\pm$0.18 stat $\pm$0.89 syst) $\times 10^{-3}$. The integrated $Z+b$ jet cross section is also measured differentially in bins of b jet transverse energy, b jet rapidity, and Z boson transverse momentum. These measurements are compared to predictions from leading order Monte Carlo generators and next-to-leading-order QCD calculations.

Also contained within this thesis are contributions to the commissioning of the ATLAS detector with early data, and studies produced for the calibration of software algorithms used in the tagging of heavy flavour jets. The resolution of the ATLAS inner detector is measured using data recorded by ATLAS in 2009. Systematic effects resulting in discrepancies between the efficiency to identify heavy flavour jets in data and simulation are measured using 2010 ATLAS data.

Acknowledgement

The author wishes to thank the University of Liverpool High Energy Physics Department and STFC for facilitating this research. Members of the department I wish to thank personally are Carl Gwilliam, Paul Laycock, and Andrew Mehta, for help and support with this work and ways to approach it, and Helen Hayward and Barry King for their moral guidance. I also express my gratitude towards my siblings for all their love and support, and to my friends for their reassurance and entertainment. I would also like to thank Marlon, Rob and the rest of the Scientific Wax family for providing the sonic inspiration to see this work through to completion. Most of all, I would like to thank Jah, Allah, God, the Buddha, Krishna, Vishnu, Shiva, etc. for doing whatever they do so we can all continue to be mesmerised by this quite fascinating and sometimes overwhelming experience called life.

Contents

List of Figures

Chapter 1

Introduction

The notion of a fundamental and indivisible unit of matter can be dated back to the 6th Century BC. In India, the Ajivika, Carvaka and Jain schools of philosophy are thought to have developed the idea of atomism, and later, the Nyaya and Vaisheshika schools produced theories on how atoms combine into more complex objects. In the Bhagavad Ghita [1], an ancient Hindu scripture that was famously quoted by theoretical physicist J. Robert Oppenheimer, some concept of the 'atom' is mentioned:

कअवइट्ठङ्घङ्ख पउरक्कत्तट्ठङ्घक्कअम अनउक्त्यण्णक्कत्तसइतक्कत्तरअम अट्ठङ्घक्कोर
अट्ठङ्घक्कक्कष्ट्ठयक्कत्तट्ठङ्घङ्खसअम अनउसमअरएद यअट्ठङ्घल्ल सअरवअसयअ
दहक्कत्ततक्कत्तरअम अचइनतयअस्रक्त्यष्ट्ठपअम क्कत्तदइतयअस्वअरट्ठङ्घक्कअट्ठङ्घङ्ख
तअमअसअट्ठङ्घल्ल पअरअसतक्कत्तत

> One meditates on the omniscient, primordial, the controller, smaller than the atom, yet the maintainer of everything; whose form is inconceivable, resplendent like the sun and totally transcendental to material nature

Later, in the 5th Century BC, ancient Greek philosophy proposed that all matter is composed of fundamental and invariant atoms, and that the phenomena we perceive are actually composite forms. In the 1st Century BC, Lucretius wrote that the atoms and 'the void' are eternal and in constant motion, and that atomic collisions create objects [2]. He suggested these objects are essentially composed of the same eternal atoms, whose motion, on a temporary basis, is incorporated into the created entity. The fundamental understanding of physical matter in the ancient world shows that clearly the investigation into the nature of material reality has long been a focus of our human curiosity.

In the modern age, this quest is continued by high energy physics experiments that collide sub-atomic particles to study the intrinsic properties of matter and how it transforms. The Large Hadron Collider at CERN in Geneva, Switzerland, began operation in 2009, and was constructed to investigate phenomena such as the nature of mass and the Higgs boson, the imbalance of matter and antimatter in the observable universe, the nature of gravity, and the 'dark matter' that seems to hold galaxies together against their rapid rotation. Since 2009, particle detectors at the LHC have recorded large datasets that are analysed by thousands of physicists for the sole purpose of building a clearer picture of the sub-atomic world.

In this thesis, data recorded by the ATLAS Experiment in 2011 is analysed to measure the probability of proton collision events containing the production of the electroweak Z boson in association with b quark jets. The purpose of making this measurement is to help verify and improve theoretical models of heavy quarks interacting via the strong nuclear force, and to improve estimates of background processes to Higgs boson decays that will help refine measurements of this elusive particle.

The structure of this thesis is as follows: Chapter 2 introduces the Standard Model of particle physics, and discusses the current theoretical description of proton collisions; Chapter 3 gives a summary of the ATLAS detector and its subsystems that perform particle measurements; Chapter 4 contains information on how collision events are reconstructed by the ATLAS software framework and how particles are identified; Chapter 5 contains studies produced for the commissioning of the ATLAS detector and of software algorithms used to identify heavy flavour quark jets; Chapter 6 is a study of systematic effects that modify the efficiency of such algorithms to identify heavy flavour jets; Chapter 7 contains the analysis of 2011 ATLAS data to measure the $Z + b$ jet production cross-section and gives a comparison to current theoretical models; Chapter 8 summarizes the information contained within this body of work. The analyses shown in Chapters 4,5, and 6 were completed individually by the author, whereas the $Z + b$ jet analysis shown in Chapter 7 was completed as a contribution to the ATLAS $Z + b$ jet analysis group, with the authors individual analysis used to cross-check results with the rest of the group.

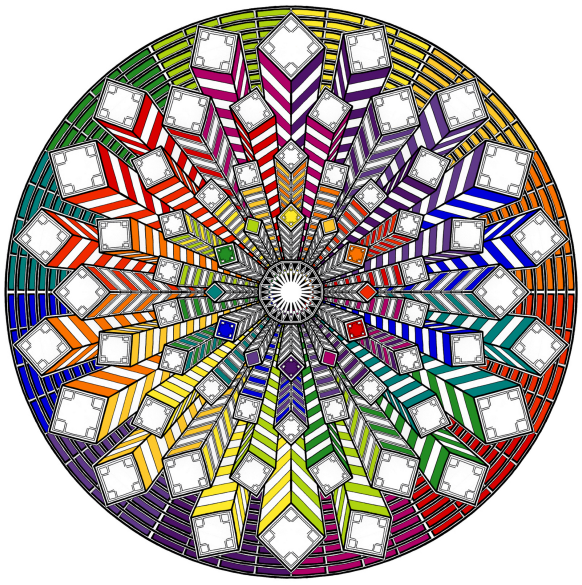

Figure 1: "Mandala 38", J. Gogarty, 2012. Drawn by hand and coloured using computer software.

Chapter 2

Theory

2.1 The Standard Model of particle physics

Since the discovery of the electron in 1897, understanding the dynamics of the elementary particles of nature has been one of the primary goals of physics. The 20th Century provided a plethora of new particles for physicists to study. This began with probing the structure of the atom, and the discoveries of the proton and neutron. In the following decades, with the discovery of the muon, the pion, kaon and lambda particles, and the electron and muon neutrinos, a more intricate picture of the subatomic world began to unfold. The development of bubble chambers and particle accelerators in the 1950s provided a platform for the rapid growth of experimental particle physics and the construction of one of the most effective theories of modern science.

The Standard Model of particle physics is currently the most complete theory for describing the constituents of subatomic matter and their interactions. Over the last 60 years, it has been very successful in explaining the fundamental processes underlying new experimental observations, and has made accurate predictions that have been later verified by precision measurements. It is a theory of interacting quantum fields generated by half-integer spin fermions and mediated by integer spin bosons.

All of the matter we currently observe in the universe is composed of fermions, which come in 3 generations of quarks and leptons, with the first generation forming the basis of ordinary matter. Quarks interact via all three forces in the Standard Model: the strong, weak, and electromagnetic forces, while leptons only experience the weak and electromagnetic interactions. Gravity is not described in the Standard Model, and developing a framework which unites it with the other three fundamental forces is one of the main goals of modern theoretical particle physics. The strong interaction is transmitted via gluons, the weak interaction is carried by the $W^{\pm}$ and Z bosons, and the electromagnetic interaction is mediated via the exchange of photons. Leptons propagate freely through space, whereas quarks only exist in bound states, and are not observed in isolation. This is due to low energy confinement in the strong interaction, where the force between quarks increases rather than decreases with separation. Instead, they form the constituents of baryons (three quarks) and mesons (quark-antiquark), which are collectively termed hadrons. The particles of the Standard Model are summarised in Figure 2 [4].

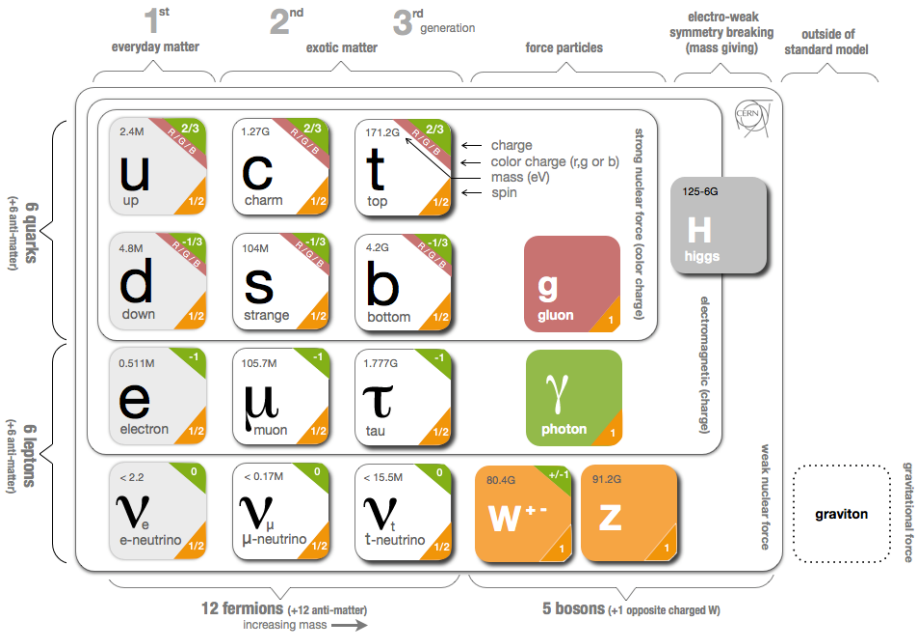

Figure 2: The fundamental constituents of subatomic matter and force-carrying particles described by the Standard Model, with their intrinsic properties.

The first steps towards the formulation of the Standard Model began with the unification of the electromagnetic and weak interactions in 1960 by Glashow [5]. Gauge invariance in the theory predicted massless bosons resulting in the weak force having an infinite range, which clearly contradicted experimental observations. A solution to this problem was proposed in the form of the Higgs field, with an associated Higgs boson predicted in 1964 [6], which allows the gauge bosons to acquire non-zero mass through electroweak symmetry breaking. The Higgs mechanism was integrated into the Electroweak Theory by Weinberg and Salam in 1967 [8], and this led to the prediction of the W and Z weak bosons in 1968, which were subsequently discovered by the UA1 experiment at CERN particle physics laboratory in 1983 [9, 10]. The tau lepton was discovered in 1975 [11] and the tau neutrino in 2001 [12].

Alongside these developments, progress was also being made with the theory of the strong interaction. In 1964, Gell-Mann [13] and Zweig [14] discovered that the observed pattern of baryons can be understood in terms of particles formed from a bound state of three constituent quarks. The semi-quantitative Quark Model was seen as a mathematical tool rather than a true description of the structure of hadrons, since they had not been observed experimentally, until in 1968 when the proton was observed to contain point-like objects in deep inelastic scattering experiments at Stanford Linear Accelerator Cen-

tre [15]. These experiments also verified the existence of the strange quark. The Quark Model was then developed further into the gauge theory of Quantum Chromodynamics, with the strong force mediated by massless gauge bosons [16]. By 1973, there totalled six quarks in the new model. The charm and bottom quarks were discovered in 1974 and 1978 in bound quark-antiquark states, the J/ψ and Υ mesons [17, 18] respectively, and the top quark was found later in 1995 from top quark pairs decaying into $W^+bW^-\bar{b}$ [19].

With the discovery of the tau neutrino the Standard Model was complete, except for the elusive Higgs boson, produced by the quantisation of the Higgs field that is reponsible for electroweak symmetry breaking and the origin of mass. In 2012, a particle was discovered at CERN that is compatible with the production and decay of the Standard Model Higgs boson [20]. Recently [21], measurements have confirmed that the new particle is indeed a Higgs boson that completes the Standard Model framework. Future measurements will ascertain whether it belongs to a family of Higgs bosons that arise from a deeper formulation of the dynamics of matter.

The theoretical formulation of the Standard Model is founded on the unification of special relativity and quantum mechanics such that particles are treated as excitations of relativistic quantum fields, and the interactions between them are described by renormalisable Lagrangian operators that are invariant under specific local transformations. The interactions take the form of vector gauge fields that arise from invariance of the Standard Model Lagrangian under transformations of the symmetry group $SU(3)_C \otimes SU(2)_I \otimes U(1)_Y$ [7].

The strong interaction is represented by the colour group $SU(3)$, with 8 massless vector gauge fields corresponding to the 8 coloured gluons. The non-Abelian nature of this group results in the direct self-coupling of gluon fields. The electroweak interaction is represented by the $SU(2)\otimes U(1)$ group, with four massless spin-1 vector fields. This symmetry is spontaneously broken through the Higgs mechanism into the electromagnetic gauge group of Quantum Electrodynamics (QED), $U(1)_{EM}$, generating mass terms for the $W^{\pm}$ and Z weak vector bosons, the Higgs boson, and all fermions. The $U(1)_{EM}$ symmetry is preserved, leaving the photon massless.

Gauge invariance of the Lagrangian operators leads to conservation of one or more charges carried by the particle fields, represented by the subscripts C, I and Y, corresponding to colour charge, weak isospin, and weak hypercharge respectively. These conserved charges are the generators of the symmetry groups. The strength of the interactions are quantified by dimensionless running coupling constants that vary in different ways with the energy of the interaction, which corresponds to the scale of renormalisation of the Lagrangian. They are free parameters in the Standard Model, and must be determined experimentally.

2.1.1 Electroweak interaction

The irreducible representations of the electroweak group $SU(2) \otimes U(1)$ are the fundamental fermions, consisting of left-handed doublets and right handed singlets of leptons and quarks. It is a chiral gauge theory, and violates charge-parity symmetry, with the $W^{\pm}$ bosons coupling only to left handed fermions and right handed antifermions. The charged currents connect up with down type quarks and charged leptons with neutrinos. There is no mixing between quarks and leptons, as the electromagnetic and weak interactions do not change colour, and no mixing between left (L) and right (R) handed fields, which would violate Lorentz symmetry. This phenomenology is represented by the $SU(2)_I$ multiplets ψ^j:

$$\psi_L^j = \begin{pmatrix} \psi_{L+}^j \\ \psi_{L-}^j \end{pmatrix}, \quad \psi_{R\sigma}^j, \tag{1}$$

with $\sigma = \pm$ denoting up-type fermions (+) and down-type fermions (−).

The quantum numbers that classify these representations are the weak isospin I, which is quantised along the third axis, I_3, and weak hypercharge Y. The doublets are formed from left-handed fields with $I = \frac{1}{2}$ and singlets from right-handed fields with $I = 0$. These quantum numbers are eigenvalues of the generators of $SU(2)$ and $U(1)$, the isospin operators $T_a = I_a$ ($a = 1, 2, 3$) and hypercharge $T_4 = Y$, and are related to the electric charge, Q, by:

$$Q = I_3 + \frac{Y}{2}\,. \tag{2}$$

Each generator has an associated vector field: the triplet $W_\mu^{1,2,3}$ for $I_{1,2,3}$, and the singlet B_μ for Y. These fields are used to build a covariant derivative $D_\mu^{L,R}$ to induce the fermion gauge field interaction, $\mathcal{L}_F$, and to derive field strength tensors $W_{\mu\nu}^a$ and $B_{\mu\nu}$ for the construction of the pure gauge-field Lagrangian, $\mathcal{L}_G$:

$$\mathcal{L}_F = \sum_j \overline{\psi}_L^j \, i\gamma^\mu D_\mu^L \psi_L^j + \sum_{j,\sigma} \overline{\psi}_{R\sigma}^j \, i\gamma^\mu D_\mu^R \psi_{R\sigma}^j\,, \tag{3}$$

$$\mathcal{L}_G = -\frac{1}{4} W_{\mu\nu}^a W^{\mu\nu,a} - \frac{1}{4} B_{\mu\nu} B^{\mu\nu}\,, \tag{4}$$

where γ^μ are the Dirac matrices. Neither $\mathcal{L}_F$ or $\mathcal{L}_G$ contain any mass terms, which would break the local gauge invariance of the $SU(2)$ symmetry by mixing the left- and right-handed fields. Instead, the masses of the weak bosons and all fermions are generated via the Higgs mechanism, which spontanously breaks the $SU(2)_I \otimes U(1)_Y$ symmetry while retaining gauge invariance of the Lagrangian.

2.1.2 Higgs mechanism

The Higgs mechanism introduces a scalar boson field Φ with $Y = 1$, in the form of a $SU(2)$ doublet $\Phi(x)$, constructed from complex scalar fields ϕ:

$$\Phi(x) = \begin{pmatrix} \phi^+(x) \\ \phi^0(x) \end{pmatrix} = \frac{1}{\sqrt{2}} \begin{pmatrix} \phi_1(x) + i\phi_2(x) \\ \phi_3(x) + i\phi_4(x) \end{pmatrix}. \tag{5}$$

The dynamics of this doublet are described by the Lagrangian density $\mathcal{L}_H$, contaning a kinematic term $|D_\mu \Phi|^2$ for the interaction of the Higgs field with the electroweak vector gauge fields, and the Higgs potential $V(\Phi)$ for the Higgs self-coupling, which is parametrised by the constants μ and λ:

$$\mathcal{L}_H = (D_\mu \Phi)^\dagger (D^\mu \Phi) - V(\Phi) = (D_\mu \Phi)^\dagger (D^\mu \Phi) + \mu^2 \phi^\dagger \phi - \lambda (\phi^\dagger \phi)^2 . \tag{6}$$

This potential has a highly degenerate ground state, the vacuum, with infinite non-vanishing solutions when $\mu^2, \lambda > 0$. These are the field configurations $\Phi^\dagger \Phi = 2\mu^2/\lambda$. By requiring the Higgs field is real and electrically neutral, a non-zero vacuum expectation value, v, is obtained:

$$\langle \Phi \rangle = \frac{1}{\sqrt{2}} \begin{pmatrix} 0 \\ v \end{pmatrix} \quad \text{with} \quad v = \frac{2\mu}{\sqrt{\lambda}} . \tag{7}$$

In contrast to $\mathcal{L}_H$, the vacuum configuration $\langle \Phi \rangle$ is not symmetric under gauge transformations of the $SU(2)_I \otimes U(1)_Y$ group, and this results in the symmetry being spontaneously broken. The electromagnetic gauge symmetry is left unbroken since $\langle \Phi \rangle$ is symmetric under $U(1)_{EM}$ transformations, and so the photon remains massless. The invariance of $\mathcal{L}_H$ allows the Higgs doublet to be transformed into the unitary gauge, eliminating three of the four degrees of freedom, and the Higgs field can be written as:

$$\Phi(x) = \frac{1}{\sqrt{2}} \begin{pmatrix} 0 \\ v + H(x) \end{pmatrix}, \tag{8}$$

where $H(x)$ is a neutral scalar particle, the Higgs boson, with a mass of $M_H = \sqrt{2}\mu$. By substituting Equation 8 into Equation 6, the non-zero vacuum expectation value generates mass terms involving the W_μ and B_μ gauge fields. The physical electroweak bosons are the mass and charge eigenstates of these fields. The fermion masses, m_f, proportional to the vacuum expectation value, are generated by Yukawa interactions between the Higgs field and the fermion fields, described by the gauge invariant Yukawa Lagrangian density:

$$\mathcal{L}_Y = -\sum_f m_f \overline{\psi}_f \psi_f - \sum_f \frac{m_f}{v} \overline{\psi}_f \psi_f H . \tag{9}$$

The full electroweak Lagrangian is given by $\mathcal{L}_{\mathrm{EW}} = \mathcal{L}_G + \mathcal{L}_H + \mathcal{L}_F + \mathcal{L}_Y$. It describes the electroweak interaction between fermions, mediated by the massive $W^{\pm}$ and Z bosons, and includes mass terms for all fermions except neutrinos, which are treated as massless in the current formulation of the Standard Model.

There are a number of free parameters in the electroweak sector that must be determined experimentally if theorectical predictions are to be made. These are the gauge coupling constants of the fermions to the W_μ and B_μ vector fields, g_2 and g_1, the Yukawa coupling constants of the fermions to the Higgs field, $G_{l,d,u}$, and the Higgs self-couplings, λ and μ. They can be replaced by a set of more physical parameters that can be measured directly: the $U(1)_{EM}$ coupling constant e, the masses of the weak bosons M_W and M_Z, the mass of the Higgs boson M_H, the fermion masses m_f, and the 3 mixing angles and phase of the CKM matrix, V_{CKM}. These mixing angles relate the mass eigenstates to the weak eigenstates, and describe the transition probability between two quark flavours. The complex phase of V_{CKM} induces CP violation. All of these parameters have been measured with high precision, now including the mass of the Higgs boson, which is measured to a precision of around 1 GeV.

2.1.3 Quantum chromodynamics

The fundamental representations of the symmetry group $SU(3)$ are the six quarks, each with three different colour states, described by colour-triplets of fermion fields, $\Psi = (q_r, q_g, q_b)^T$. These triplets are invariant under the $SU(3)$ colour-space transformations, and so the conserved charges for the strong interaction are the three colour charges r, g, b. The existence of colour charge allows quarks to co-exist inside hadrons without violating the Pauli exclusion principle. $SU(3)$ has eight generators T_a, which are expressed in terms of the eight 3×3 Gell-Mann matrices, λ_a, in the triplet representation:

$$T_a = \frac{1}{2}\lambda_a\,, \quad a = 1, \ldots 8\,. \tag{10}$$

These generators correspond directly to the eight coloured gluons. The covariant derivative D_μ that acts on the quark triplets Ψ is built from the generators T_a and the eight gluon fields G^a_μ, and contains the strong coupling constant g_s:

$$D_\mu = \partial_\mu - ig_s \frac{\lambda_a}{2} G^a_\mu\,. \tag{11}$$

The gluon fields also appear in the field strength tensor, $G^a_{\mu\nu}$, which is similar to the abelian result in QED, but with an additional non-Abelian term, f^{abc}, proportional to the structure constants of the group.

These structure functions are responsible for the colour charge of the gluon and the self-coupling of the gluon fields, and determine the running of the coupling strength of the strong interaction with energy. The field strength tensor is given by:

$$G^a_{\mu\nu} = \partial_\mu G^a_\nu - \partial_\nu G^a_\mu + g_s\, f_{abc}\, G^b_\mu G^c_\nu \,. \tag{12}$$

The covariant derivative and field strength tensor are used to construct the Lagrangian density $\mathcal{L}_{\mathrm{QCD}}$, which describes the interactions of the quark fermion fields with the gluon fields, and contains the gluon density, $\mathcal{L}_{\mathrm{G}}$, for the triple and quartic gluon self-interactions:

$$\begin{aligned} \mathcal{L}_{\mathrm{QCD}} &= \overline{\Psi}\,(i\gamma^\mu D_\mu - m)\Psi \;+\; \mathcal{L}_G \\ &= \overline{\Psi}\,(i\gamma^\mu \partial_\mu - m)\Psi \;+\; g_s\,\overline{\Psi}\gamma^\mu \frac{\lambda_a}{2}\Psi\, G^a_\mu \;-\; \frac{1}{4}\, G^a_{\mu\nu} G^{a,\mu\nu} \,, \end{aligned} \tag{13}$$

where m is the quark mass originating from the electroweak sector. The quark mass is specific to each flavour and so the full QCD Lagrangian sums over the six flavours. It is also necessary to include additional gauge-fixing terms for each gluon field, which are chosen to give the same form for the gluon propagators as the photon propagators in QED. There is only one free parameter in the QCD Lagrangian, g_s.

The non-Abelian nature of $SU(3)$ results in the strong interaction exhibiting certain properties that make it very different to the other fundamental forces of nature. Quarks experience colour confinement due to the strong force coupling diverging at large distances, so hadrons can only exist in colour singlet states. When quarks are separated, the growing potential energy between them can become so large that it is energetically more favourable to create quark-antiquark pairs, that then combine with the original partons to form colour neutral hadrons. This process is the basis of hadronisation and jet formation for particles produced from high energy collisions. It is non-peturbative, and so jet formation cannot be calculated theoretically but must be modelled and tuned using experimental data. At small distances, or large energies, quarks experience asymptotic freedom, and inside hadrons quarks and gluons behave like free particles. At the high collision energies of modern particle accelerators the coupling is small enough for quarks and gluons to be treated as perturbative objects, and this allows the theoretical calculation of scattering probabilities and cross-sections.

2.2 Proton collisions

The nature of the strong interaction gives rise to an intricate hadronic structure. Experiments have determined parton distribution functions (PDFs) that describe the structure of the proton, and these are

essential to understand the scattering processes that occur in high energy proton-proton collisions. The running of the strong coupling constant with energy scale and the resulting asymptotic freedom and confinement embedded within the structure of the proton introduces a variety of effects in collisions, and in the formation of the final state hadrons that deposit energy in detectors.

The scattering processes that take place in proton collisions can be hard or soft, depending on the energy scale. Hard scatter processes occur when there is a high energy interaction with large momentum transfer between two partons, such is necessary for the production of a Z boson or high-p_T jets. Event properties and rates for hard scatter processes can be calculated accurately with perturbation theory. Soft processes involve low energy interactions and small momentum transfers between partons and are non-perturbative, so cannot be calculated directly. Predictions for these processes are made by fitting phenomenological models to experimental data. These models are typically long-distance functions, such as those describing the proton structure, and the "underlying event" specific to the initial state of the hard scatter that contains low energy interactions between the other partons from the colliding proton. It is also important to understand soft "pile-up" events resulting from low energy interactions of other protons in the colliding bunches, or from other bunches, that overlap with the main hard scatter process. For accurate theoretical predictions of production cross-sections from the interactions of colliding protons, these non-perturbative phenomena must be well understood.

2.2.1 Parton distribution functions

PDFs are determined with global fits to a variety of data, including deep inelastic scattering, Drell-Yan ($qq \rightarrow Z/\gamma* \rightarrow ll$), and jet production measurements from collider experiments. These fits describe the probability of finding a given parton that carries a fraction x of the four-momentum of the incoming proton at a given momentum scale Q^2 that characterises the scattering process. The dependence of the parton distributions on Q^2 is determined by extracting starting distributions from the global fits over a range of scales that are parametrised to construct perturbative solutions to the DGLAP equations [23]. At first order, partonic interactions are described by three branching processes: a quark radiating a gluon, quark pair production, and gluon splitting. The amplitude of these processes are given by the splitting functions $P_{ab}(r)$, which describe the probability of a parton of type b to decay into a parton of type a by radiating a gluon or quark:

$$
\begin{aligned}
P_{qq}(r) &= \frac{4}{3}\frac{1+r^2}{1-r} && \text{gluon radiation from quark} \\
P_{qg}(r) &= \frac{1}{2}[r^2 + (1-r)^2] && \text{quark pair production} \\
P_{gg}(r) &= 6\left[\frac{r}{1-r} + \frac{1-r}{r} + r(1-r)\right] && \text{gluon splitting}
\end{aligned} \tag{14}
$$

where r is the fraction of the longitudinal momentum of parton b carried by parton a. The evolution of the PDFs with Q^2 at leading order is described by these functions.

2.2.2 Cross-sections

Hadronic cross-sections are determined using factorisation theorems [22] that introduce a factorisation scale μ_F to separate the short-range perturbative calculation of the hard scatter from the long-range non-perturbative calculation that describes the proton structure with PDFs. The hard scatter process is calculated with matrix elements that describe the complex amplitude of the interaction. Large logarithmic corrections from gluons emitted collinear with the incoming quarks in the hard scatter are absorbed via the DGLAP equations into the renormalised PDFs. The hadronic cross-section for a process σ_{AB} is therefore calculated as the convolution of the partonic cross-section $\hat{\sigma}_{ab}$ of the hard scatter with the proton PDF $f_{a|A}(x_a, Q^2)$:

$$
\sigma_{AB} = \int dx_a dx_b \, f_{a/A}(x_a, \mu_F^2) \, f_{b/B}(x_b, \mu_F^2) \times [\, \hat{\sigma}_{LO} + \alpha_S(\mu_R^2)\, \hat{\sigma}_{NLO} + \ldots \,]_{ab\to X} \,, \tag{15}
$$

where μ_R is the renormalisation scale for the running coupling α_S, and the partonic cross-sections are shown at leading order (LO) and next-to-leading order (NLO). The momentum fractions $x_{a,b}$ of the colliding protons carried by the partons are related to the squares of the centre-of-mass energies of the partons, $\hat{s}$, and hadrons, s, by $\hat{s} = x_a x_b s$. The scales μ_R and μ_F are typically chosen to be the energy scales that characterise the hard scatter process, such as m_Z^2 or $\langle p_{T,jet}^2 \rangle$. The partonic cross-section at leading order is obtained by integrating the squared matrix element from the tree-level Feynmann diagrams over the relevant phase space. The result for Drell-Yan Z boson production, for example, is given by:

$$
\hat{\sigma}^{q\bar{q}\to Z} = \frac{\pi}{3}\sqrt{2} G_F M_Z^2 (v_q^2 + a_q^2)\delta(\hat{s} - M_Z^2), \tag{16}
$$

where G_F is the Fermi coupling constant, and v_q, a_q are the vector and axial coupling of the Z boson to quarks.

To obtain accurate differential predictions, and for more complicated processes such as Z + jet production, this integration must be done numerically and over a limited phase space to avoid divergences.

Large uncertainties arise in these calculations from the dependence on the unphysical factorisation and renormalisation scales, and higher order terms need to be calculated if precise comparisons of kinematic variables are to be made. These terms correspond to Feynman diagrams with extra vertices that introduce additional powers of g_s, and describe real and virtual processes such as initial and final state radiation and loop corrections. They can either be calculated explicitly from matrix elements (usually only at next-to-leading order due to computational complexity), or determined iteratively using PDFs and 'form factors' by parton shower algorithms. Matrix element calculations are performed by event generators that simulate hard multi-parton processes with a probability approximately proportional to the cross-section, and produce a list of final state particles and their momenta that is used as input to the parton shower algorithms. Often, a 'k' factor is applied to a leading order cross-section calculation to correct for higher order terms.

2.2.3 Parton shower

The hard scatter process involves large momentum transfers, with the partons in the initial and final state subject to extreme acceleration, resulting in the radiation of a succession of gluons and quarks that form the parton shower. Final state partons are highly virtual and must radiate energy through a cascade of emissions until the interaction scale is low enough, and the strong coupling large enough, to initiate the process of hadronisation, where the partons in the shower recombine to form colour-neutral mesons and baryons. The structure of a typical high energy proton-proton collision is shown in Figure 3.

Parton shower programs simulate the final state partons in full detail to pass to the hadronisation algorithms for the accurate prediction of stable particles that are measured in detectors. The algorithms generate $1 \rightarrow 2$ parton emissions from a large starting scale that is characteristic of the matrix element calculation, e.g. m_Z^2, down to a cut-off at the scale of hadronisation, typically around a few GeV, where non-peturbative effects take over. Emissions are calculated in segments ordered by an evolution variable, such as Q^2, relative p_T, or separation angle of the intial state partons. The amplitude of processes that generate additional partons are given by the splitting functions in Equation 14. These are used to construct the Sukadov form factors that give the probability of a parton to evolve from a hard scale t to a soft scale t_0, with momentum fraction z, without emitting a parton harder than a chosen resolution scale [25]. The form factor for initial state partons can be written as:

$$\Delta(t) \equiv \exp\left[-\int_{t_0}^{t} \frac{dt'}{t'} \int \frac{dz}{z} \frac{\alpha_S}{2\pi} P(z) \frac{f(x/z,t)}{f(x,t)}\right]. \tag{17}$$

Final state partons have similar form factors that are not weighted by PDFs. The parton decreases in

virtuality through emissions until its momentum fraction matches that in the PDFs, which determine the kinematics of the emitted partons.

2.2.4 Hadronisation

The parton shower results in a jet of partons moving roughly in the same direction as the final state parton from the hard scatter. Once all the partons in the shower have branched sufficiently and the strong coupling becomes large enough, the dynamics enter the non-peturbative phase and hadrons are formed. There are two main models for this process, built from ideological assumptions of general features in QCD, that are parametrised and tuned to experimental data.

The Lund string model [26] is based on lattice simulations and the observation that the potential energy between particles carrying colour charge increases linearly with separation. This is due to the self-interaction of the gluon fields, which causes the field lines to be compressed into 'strings'. For two quarks moving rapidly apart, this confinement potential grows until there is enough energy to produce a quark-antiquark pair, and the string is broken. The new antiquark is connected to the original quark and vice versa, forming two colour singlet states. These two shorter string segments then stretch and break, and this process repeats until sufficient energy has been converted into quark-antiquark pairs connected

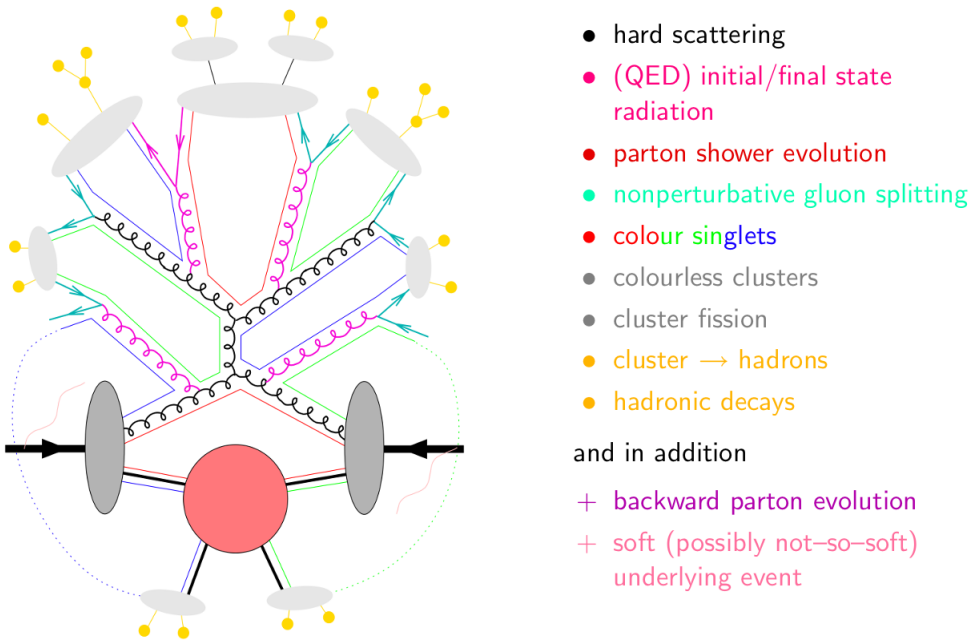

Figure 3: A proton-proton collision producing a top quark pair, illustrating various processes producing final state particles that deposit energy in the detector [24].

with short string segments that are bound into hadrons. Following the parton shower, there is a large number of partons at the hadronisation scale, and the evolution of the system depends on the colour structure. Each parton has a unique colour partner with a string connecting them, and any additional partons connected to this string will enhance hadron production in its direction of motion.

The cluster model [27] is based on 'pre-confinement' in QCD. This is where partons in the shower are clustered into colourless groups when the evolution scale is much less than that of the hard scatter. The invariant mass of these clusters only depends on the evolution scale and the QCD scale, Λ, and is independent of the hard scatter process. At the cut-off scale, all gluons from the shower are forced to split into quark-antiquark pairs, with clusters formed from the splitting of colour partners. The cluster mass is limited to a few GeV, and so there is a limit to the tranverse momentum generated through this process. For high mass clusters, a variation on the string model is used, with the difference that only two partons can be connected and any intermediate gluon breaks the string. The clusters are essentially proto-hadrons and decay into the observed hadronic states.

2.3 The Z + *b*-jets signal

The Z + b jet channel is a significant background to many physics processes at the LHC. It is one of the main backgrounds in searches for the supersymmetric partners of b quarks, and $Z + b\bar{b}$ is the largest background for Higgs boson searches in the $ZH \rightarrow Zb\bar{b}$ decay mode, shown in Figure 4. An accurate cross-section measurement for this process is therefore necessary for precision measurements in the Higgs sector and many searches for physics beyond the Standard Model. This process is also sensitive to the b quark density in the proton, and a precise knowledge of the b density is required to accurately predict processes that strongly depend on it, such as the production of supersymmetric Higgs bosons, or the electroweak production of single top quarks.

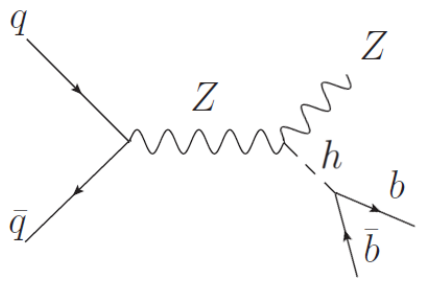

Figure 4: Feynman diagram for $ZH \rightarrow Zb\bar{b}$ production at the LHC.

The production of a Z boson in association with one or more b quark jets from proton-proton collisions provides an important test of peturbative QCD predictions in a multi-scale environment. Current theoretical predictions for this process vary significantly, and so a precision differential cross-section measurement is required to test these predictions. The dominant contribution to $Z + b$ jet production at the LHC at $\sqrt{s} = 7$ TeV comes from the interactions of splitting gluons, since the gluon density in the proton is significantly higher than that of the b quark. The leading order Feynman diagrams for the hard scatter processes that produce this final state are shown in Figure 5.

There are currently two methods of calculating such processes theoretically, the fixed-flavour (or four-flavour) scheme, which does not factor in the b quark density in the proton, and the variable-flavour (or five-flavour) scheme, which includes the b quark in the proton PDF. The differential measurement of the $Z + b$ jet cross-section can be used to test which of these schemes is more accurate. The top two diagrams in Figure 5 are the leading order subprocesses for $Z + b$ production and are only calculated in the variable flavour scheme. A massive b quark from the parton sea participates directly in the hard scatter. This is calculated by integrating the gluon splitting process into the b quark PDF, which is derived peturbatively from the gluon distributions using the DGLAP equations. Gluon splitting in the initial state produces a collinear $b\bar{b}$ pair, with one low-p_T b quark travelling along the beam pipe that is not detected, while the other b quark participates in the hard scatter process, emerging with high-p_T and producing a jet that deposits energy in the detector. Since this process is sensitive to the b quark density in the proton, precision measurements of the transverse momenta and rapidity of both the Z boson and b jet can be used to constrain the b quark PDF. An improved knowledge of the PDFs is essential, as almost all

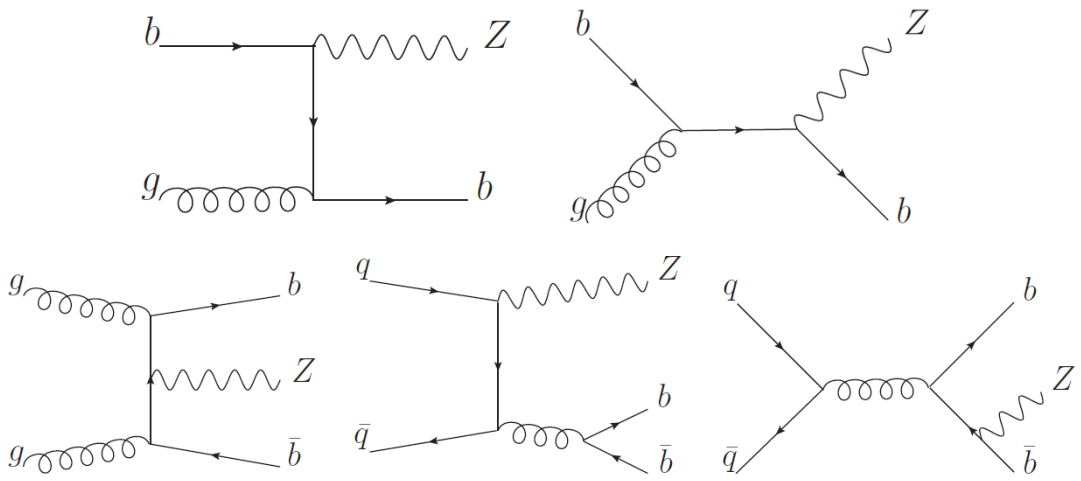

Figure 5: Main leading order diagrams for the associated production of a Z *boson and one or two* b *jets.*

measurements at the LHC are significantly affected by the PDF uncertainties.

The bottom three diagrams are the leading order subprocesses for $Z + b\bar{b}$ production, and are calculated by both schemes. The b quark density in the proton is not considered, and b quarks only arise through gluon splitting, which produces a $b\bar{b}$ pair in the final state. In the evaluation of the matrix elements, the b quarks are treated as massive. In the centre diagram, the $b\bar{b}$ pair can be produced very close to each other and thus may be reconstructed in the same jet. At any finite order in the pertubative expansion of the partonic cross-section calculated by integrating the matrix elements, the two schemes will produce different results, with additional large uncertainties arising from the PDFs. They can therefore be tested by comparing their predictions to precision differential cross-section measurements.

The current methods for calculating the next-to-leading order corrections for $gb \rightarrow Zb$ use the b quark density from the PDFs and treat the b quarks as massless. Including these corrections substantially increases the cross-section for this subprocess and decreases dependence on the renormalisation and factorisation scales. However, the cross-section calculation still varies significantly depending on the choice of these scales. By comparing the predicted and measured differential cross-sections the scale choice can be tested. This test was performed with the CDF experiment at Fermilab and is shown in Figure 6 [29], where both the renormalisation and factorisation scales are chosen to be either $Q^2 = m_Z^2 + p_{T,Z}^2$ or $Q^2 = \langle p_{T,jet}^2 \rangle$. The CDF results cannot distinguish very well between these scales, and so an LHC measurement is required to determine the correct scale choice.

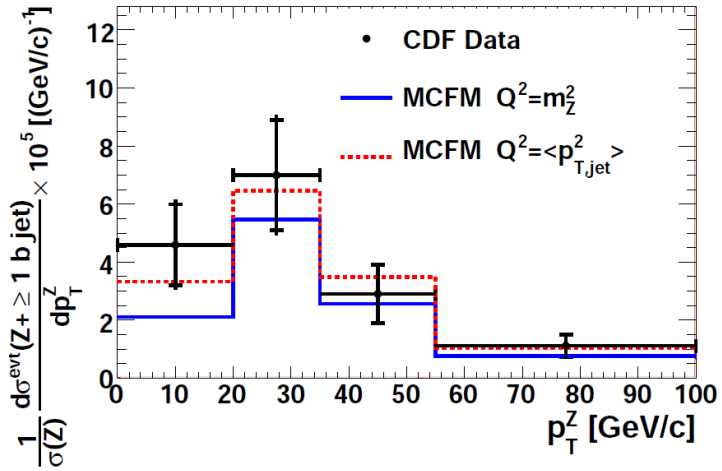

Figure 6: Ratio of the Z + b jet cross-section to the inclusive Z boson cross-section versus p_T^Z from the CDF experiment. Shown are the data compared to predictions from MFCM *calculated with the scales $Q^2 = m_Z^2 + p_{T,Z}^2$ (solid line) and with $Q^2 = \langle p_{T,jet}^2 \rangle$ (dotted line).*

Chapter 3

The ATLAS Experiment

3.1 The Large Hadron Collider

The Large Hadron Collider (LHC) [31] is a two-ring hadron accelerator, colliding two beams of protons up to a centre of mass energy of $\sqrt{s}$ = 14 TeV with an instantaneous luminosity of 10^{34} cm^{-2}s^{-1}. It is installed in the 26.7 km underground tunnel that was used for the Large Electron Positron collider in Geneva, Switzerland. It utilizes existing synchrotrons from previous CERN experiments to accelerate protons to 450 GeV for injection into the LHC ring, as shown in Figure 7.

The injected beam is captured, accelerated and stored by a 400 MHz superconducting radio frequency cavity system. Precise control of the field in each RF cavity is achieved by a complex feedback system, which is essential for the high intensity LHC proton beam. The LHC uses state-of-the-art NbTi superconducting dipole magnets operating at 8 T to bend the path of the proton beam. Superfluid helium is used to cool the magnets to below 2 K. A series of 858 quadrupole magnets throughout the beamline keep the proton beam focused to a width of around 0.2 mm. At the interaction points, inner triplet magnets focus the proton beams down to a width of around 12 μm for collision [32].

At nominal operation, each proton beam contains 2808 bunches of $\sim 10^{11}$ protons, with a bunch crossing frequency of up to 40 MHz, providing around 20 inelastic proton collisions per crossing and 600 million inelastic events per second. There are 3 main experiments that record these events for physics analysis: ATLAS [34], CMS [35] and LHCb [36]. Both ATLAS and CMS are general purpose detectors designed to search for new physics, such as Supersymmetry and the Higgs boson, whereas LHCb is built primarily to study CP violation in B-meson decay. A fourth experiment, ALICE [37], studies the collisions of lead nuclei to investigate the properties of quark-gluon plasma when the LHC is switched from accelerating protons to accelerating heavy ions.

3.2 The ATLAS experiment

The ATLAS Experiment consists of a general purpose detector situated 100 m underground at one of the four collision points of the LHC. The aim of the experiment, which is one of the largest scientific collaborations in history, is to search for a wide range of physics signatures within and beyond the

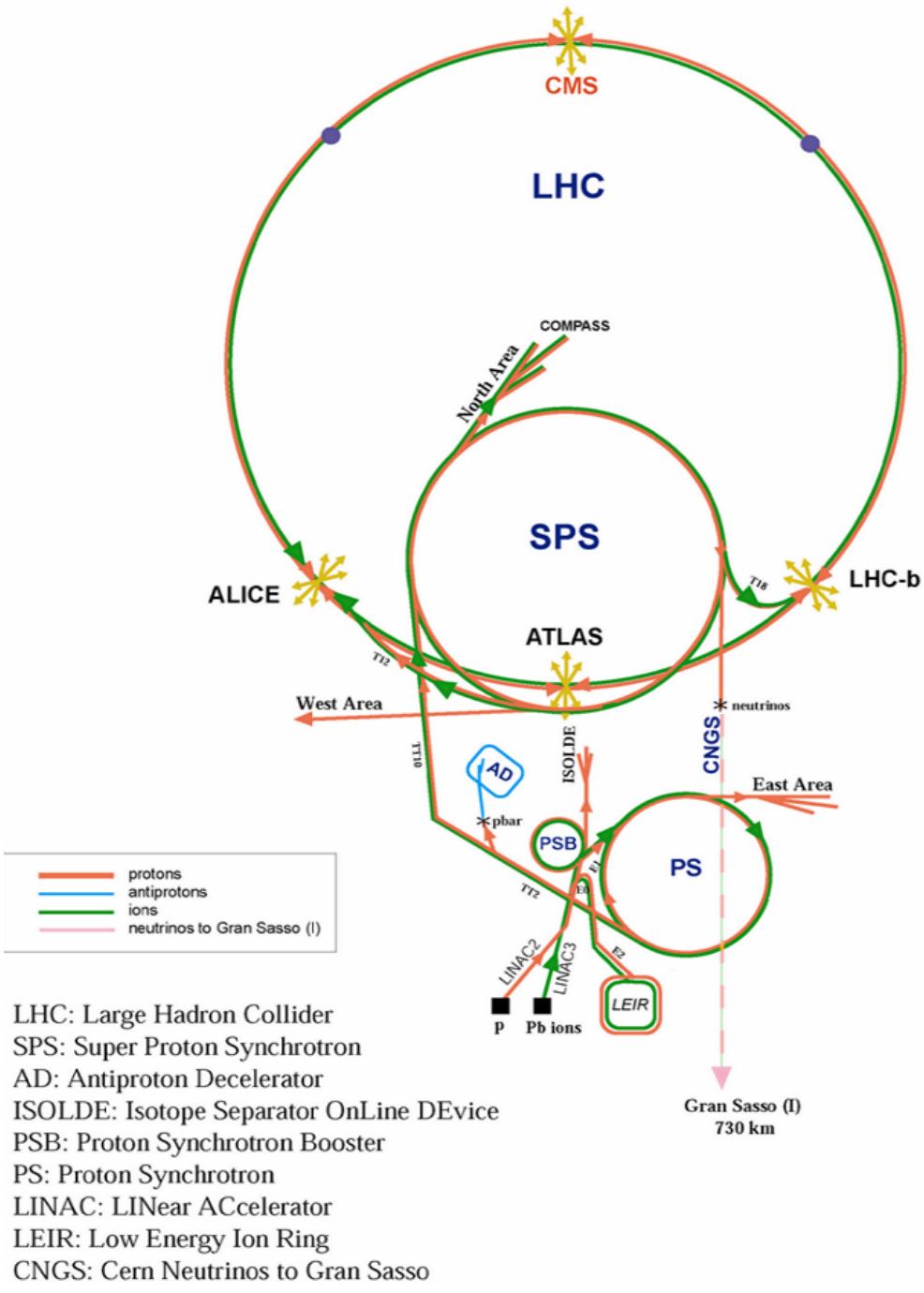

Figure 7: The Large Hadron Collider at CERN [33]

Standard Model (SM) of particle physics. One of these signatures is the long awaited Higgs boson, the last particle required to complete the SM. This was a primary goal for the ATLAS experiment: to discover the Higgs, or exclude it within a wide mass range, thus giving insight into the dynamics of electroweak symmetry breaking and the nature of mass. Now that the Higgs boson has been discovered,

the task begins to measure and understand this new particle with ATLAS data.

Another important part of the ATLAS physics programme is to search for new resonances that are predicted by Supersymmetry (SUSY). The unprecedented collision energies of the LHC may produce heavier 'superpartners' to the SM particles, which could be detected and measured by the ATLAS detector, thus verifying a deeper formulation of particle physics and solving theoretical problems that exist in the SM. Other areas of research beyond the SM include the search for new heavier gauge bosons, *W'* and *Z'*, and for evidence of additional space dimensions that could explain why the strength of gravity is so much weaker than the other three fundamental forces of nature. ATLAS will also make precision measurements of existing SM parameters, and test current QCD models and predictions.

3.3 The ATLAS detector

The ATLAS detector measures the flight paths, momenta and energies of particles using a series of high resolution trackers and calorimeters surrounding the interaction point with forward-backward symmetry and providing close to 4π solid angle coverage. The hermetic nature of the detector means that almost all particles from collisions pass through multiple detector subsystems, allowing full and accurate event reconstruction from the measured quantities. Toroid and solenoid magnet systems embedded within the detector bend the paths of charged particles to allow charge and momentum measurements. A cut-away view of the ATLAS detector is shown in Figure 8.

The high collision rate within ATLAS requires a complex online and offline triggering system to select only those events containing interesting particle interactions. Events passing the online triggers are recorded to disk and undergo further offline selection and quality checks before being signed off ready to be used in physics analysis.

The co-ordinate system used in ATLAS is right-handed, with the x-direction defined towards the centre of the LHC ring, the y-direction vertically upwards, and the z-direction pointing anticlockwise around the ring. Azimuthal and polar angles, ϕ and θ, are defined with respect to this coordinate system. More commonly used to define particle trajectory relative to the beampipe are the rapidity, defined in Equation 18 in terms of the particle energy, E, and the z-component of momentum, p_z, and pseudorapidity, defined in Equation 19 such that particle production is approximately constant with $|\eta|$.

$$y = \frac{1}{2} ln(\frac{E + p_z}{E - p_z}) \tag{18}$$

$$\eta = -ln(tan\frac{\theta}{2}) \tag{19}$$

3.4 Inner detector

The large track density and the need for high resolution momentum and vertex measurements in ATLAS requires a series of fine-granularity detectors as close to the collision point as possible. The silicon pixel and SemiConductor Tracker (SCT) detectors at the heart of ATLAS provide high precision measurements of the particle tracks from a radius of 4 cm from the beampipe, allowing identification of short-lived particles such as b quarks and τ leptons. There are 3 concentric barrels of high granularity pixel detectors with 4 endcap discs either side, followed by 4 layers of silicon microstrip detectors (SCT), with 9 endcaps each side, so that tracks within $|\eta| < 2.5$ are measured with 7 precision three-dimensional space points. This is surrounded by the Transition Radiation Tracker (TRT), a dense array of straw detectors providing a large number of tracking points to improve track reconstruction. An overview of the parameters of the inner detector sub-systems is given in Table 1 [38]. A schematic view of the inner detector is shown in Figure 9.

System	Position	Area (m^2)	Resolutions (μm)	Channels (10^6)	η coverage
Pixels	1 removable barrel layer	0.2	$r\phi$ = 12, z = 66	16	±2.5
	2 barrel layers	1.4	$r\phi$ = 12, z = 66	81	±1.7
	4 end-cap disks on each side	0.7	$r\phi$ = 12, r = 77	43	±1.7-2.5
Silicon strips	4 barrel layers	34.4	$r\phi$ = 16, z = 580	3.2	±1.4
	9 end-cap wheels on each side	26.7	$r\phi$ = 16, r = 580	3.0	±1.4-2.5
TRT	Axial barrel straws		170 (per straw)	0.1	±0.7
	Radial end-cap straws		170 (per straw)	0.32	±0.7-2.5
	36 straws per track				

Table 1: Parameters of the inner detector. The resolutions quoted are typical values (the actual resolution in each detector depends on $|\eta|$).

The entire inner detector is surrounded by a 2 T solenoid magnet system to bend the paths of charged particles, allowing particle momenta and charge to be determined. For tracks with p_T ~1 GeV, a momentum resolution of ~2 % is achieved, which increases to a resolution of ~10 % for tracks with $p_T > 100$

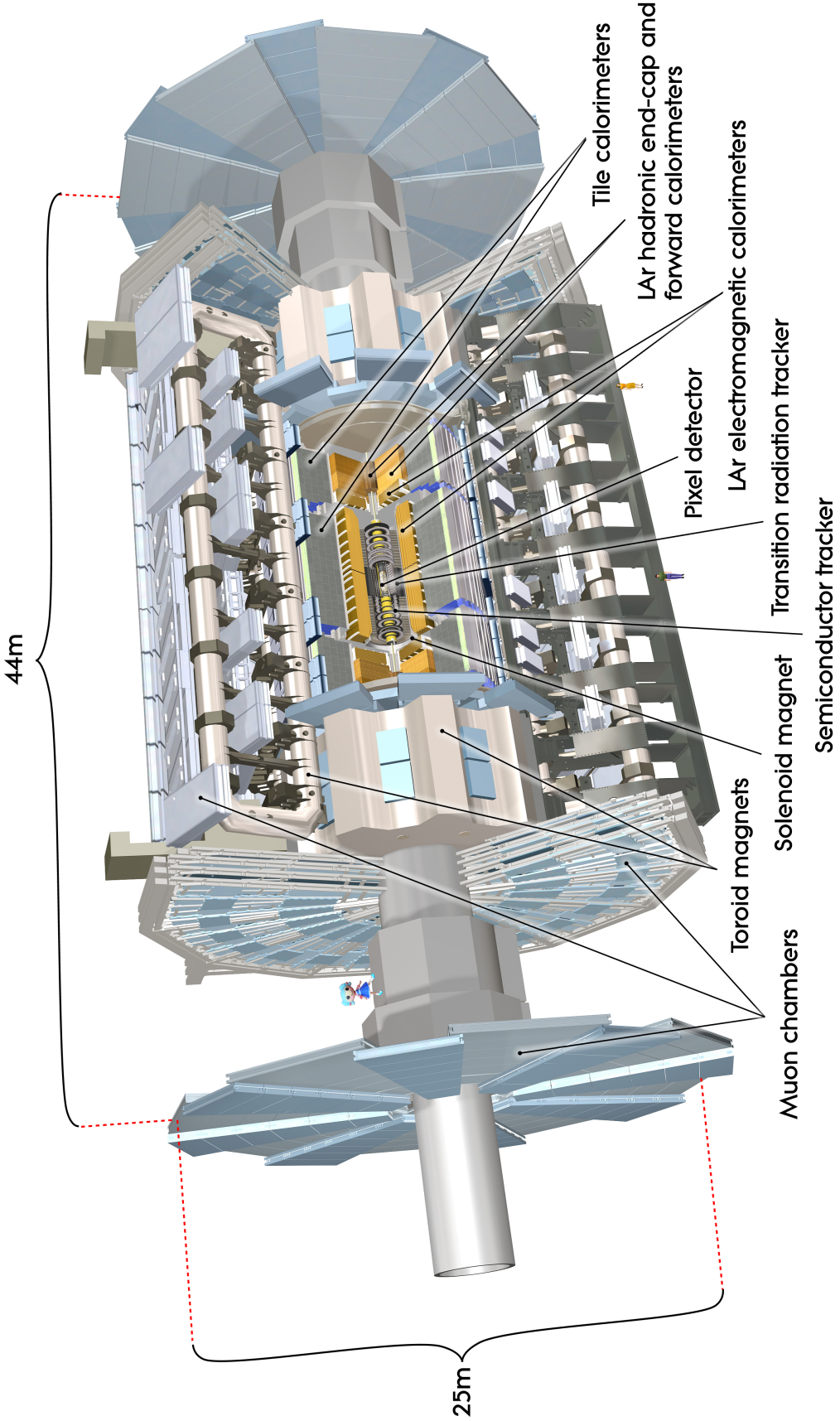

Figure 8: A schematic view of the ATLAS detector and its subsystems.

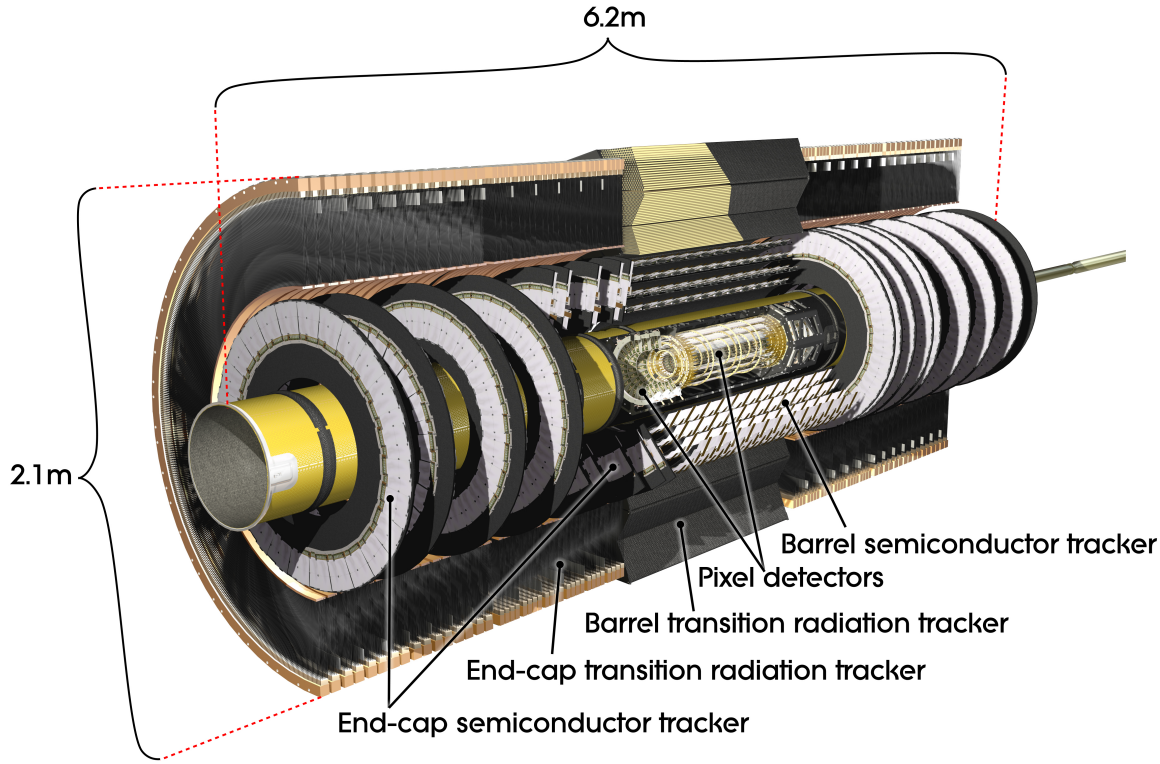

Figure 9: Schematic view of the ATLAS inner detector, showing the pixel, SCT, and TRT sub-systems.

GeV. Particle tracks reconstructed from the inner detector measurements are crucial in determining the primary and secondary vertices of an event.

The sensors and readout electronics of the inner detector are exposed to very high levels of radiation due to their proximity to the interaction point. The pixel and SCT systems have been built to tolerate up to 10 years 1 MeV neutron equivalent fluences squared of 8×10^{14} cm^2 and 2×10^{14} cm^2 respectively, with the exception of the innermost pixel barrel, the *b* layer, which is designed for replacement after 3 years of operating at nominal luminosity. All silicon sensors are operated at between -5 and -10 °C to prevent reverse annealing and the associated increase in required bias voltage [39]. The TRT is radiation hard and does not experience degradation in performance due to high radiation levels.

There are two important properties of the inner detector that significantly affect the accuracy of measurements. Materials used for the detector elements, support structures and services give rise to multiple scattering, bremsstrahlung, and photon conversion, which affect momentum resolution and track reconstruction, the extent of which is determined by the number of radiation lengths (or interaction lengths for hadronic interactions) traversed by a particle within the detector acceptance, displayed in

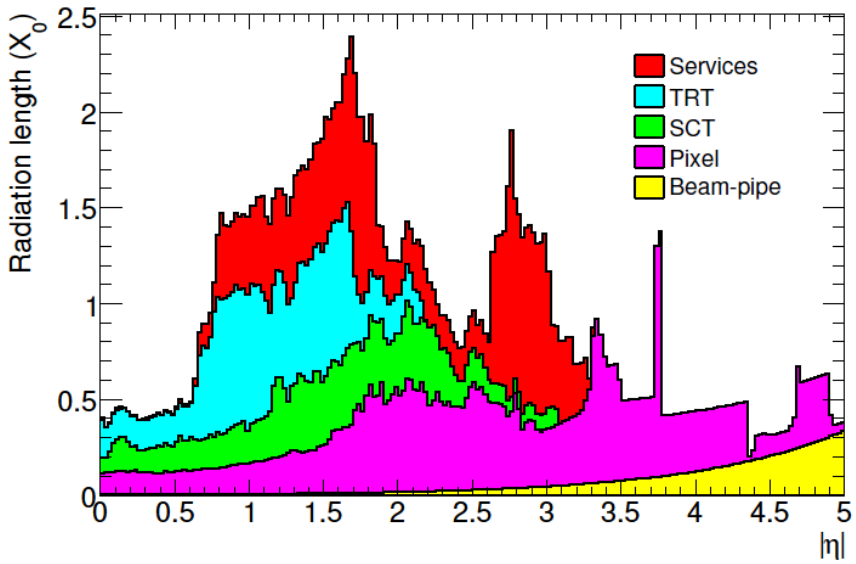

Figure 10: Radiation lengths traversed by an infinite momentum particle in the inner detector as a function of $|\eta|$, showing contributions from the different subsystems and services.

Figure 10. A large effort is made to ensure the material budget is described accurately in simulation. It is also essential to know precisely the positions of the silicon modules and their alignment. Track based alignment was initially performed with cosmic rays, and is monitored daily during collisions using a selection of ~1 million tracks. An interferometer system installed in the SCT also monitors the alignment of the detector modules. This ensures that the resolution of track parameters does not deteriorate by more than 20 % with respect to the intrinsic tracker resolution [40]. The effects of the material budget and misalignment in the commissioning of the inner detector with first collision data are discussed in detail in Chapter 5.

3.4.1 Pixel detector

The pixel detector is comprised of 3 pixel barrels at 4 cm, 11 cm and 14 cm from the beampipe, with 4 endcap discs that cover radii of 9-15 cm positioned at z from 50 to 65 cm, providing complete angular coverage up to $|\eta| < 2.5$. These are built from a total of 2586 pixel modules, each with 160×24 pixels read out by 16 chips. Each pixel has dimensions of 50 μm in the ϕ direction and 400 μm in z (barrel) or r (endcap). A pixel sensor consists of an array of n^+ diodes implanted on n bulk silicon on one side, with a layer of p^+ silicon implanted on the other side. A large reverse bias of a few hundred volts is applied to the sensor, creating a depletion region, so that ionising particles passing through this active volume

deposit energy and create charge carriers that are collected at the n^+ diodes. The front-end chip amplifies and digitizes the charge pulse, and sends the data to the module control chip, which serializes the data and stores it in a buffer to be read out if a trigger signal is received at the correct time.

The pixel detector has resolution of 12 μm in the r-ϕ direction, and 60 μm in the z-direction, or r-direction for the endcaps [41]. The high granularity of the pixel detector is crucial to achieve high impact parameter resolution and accurate vertex location, which allows the identification of secondary vertices from the decay of short-lived particles, such as b quarks, which are often a signature of interesting physics. The transverse impact parameter, d_0, is defined as the distance between the point of closest approach of a track to the primary vertex in the r-ϕ plane, and the longitudinal impact parameter, z_0, is the z-coordinate of this point. The sign of the impact parameters are defined as positive if the track intersects the jet direction in front of the primary vertex and negative if the track intersects the jet direction behind the primary vertex. The impact parameter resolution of the inner detector is discussed in Chapter 5.

3.4.2 Semiconductor tracker

The SCT consists of 4 barrel layers concentric with the beam axis at radii of 30, 37, 45 and 52 cm, and 9 endcap disks either side of the interaction point extending to $z = 2.8$ m from the centre of the detector [42]. There are 2112 barrel modules and 1976 endcap modules. Each module consists of two layers of 768 p^+ silicon strips implanted onto high resistivity n-bulk, glued back-to-back with a 40 mrad stereo angle. When an ionizing particle deposits energy in the active regions of the two layers, two crossed strips from either side will receive a charge pulse, which is amplified and digitized by one of 6 front end chips per side. Barrel modules have one set of strips aligned along z, whereas endcap modules with tapered strips have one set aligned along r. This provides a tracking point with spatial resolution of 16 μm in the r-ϕ direction, and 580 μm in the z-direction, or r-direction in the endcaps. The lower resolution in z or r is due to the pitch between the crossed p^+ strips. The SCT provides at least 4 position measurements in r-ϕ and z or r per track, contributing significantly to the momentum and impact parameter resolutions and vertex locating capabilities of the inner detector.

3.4.3 Transition radiation tracker

Surrounding the silicon based trackers is the TRT, composed of 351,000 proportional drift tubes, or straws, filled with a gas made up from 70 % xenon, 20 % tetrafluoromethane (CF4) and 10 % carbon

dioxide, each with a high voltage 30 μm diameter gold-plated tungsten wire anode running through the centre [43]. The straws measure 4mm in diameter, up to 144cm in length, and are arranged into three barrels and two endcap wheels. The TRT covers the slightly narrower range of $|\eta| < 2.0$, and each straw provides measurements with an intrinsic precision of 130 μm in r-ϕ. The straws are interleaved with polypropylene-polyethylene fibers in the barrel and polypropylene foils in the endcaps, such that when ultra-relativistic particles, mainly electrons, pass through the dielectric boundaries, x-ray transition radiation is produced, increasing the signal amplitude by adding to the ionization of the xenon gas from the original traversing particle. Since the amount of transition radiation produced is directly proportional to a particles relativistic γ factor, particle discrimination is made possible by operating at two thresholds, providing separation of electrons/positrons and pions. Particle tracks within the TRT acceptance typically cross 35-40 straws, thus providing detailed tracking at larger radii, which greatly improves pattern recognition and track reconstruction.

3.5 Electromagnetic calorimeter

The electromagnetic (EM) calorimeter in ATLAS is a lead-liquid-argon sampling calorimeter covering pseudorapidity range of $|\eta| < 3.2$, that triggers on and provides precision energy measurements of electrons, photons, the EM component of jets, and helps identify the missing E_T in an event. Liquid argon is used as the ionizing medium because of its radiation tolerance, stability of response throughout the volume and over time, and intrinsic linear behaviour as a function of deposited energy [45]. The layout of the EM calorimeter, shown in Figure 11, is divided into two identical half barrels with a gap of a few millimetres, and two concentric wheels for each endcap with the centre of these forming the forward calorimeter. Uniform coverage over ϕ is achieved using accordion-shaped lead absorbers, shown in Figure 12, segmented longitudinally to measure shower evolution as a function of depth, which is an essential tool for background rejection. Copper- polyimide multilayer readout boards are located between the absorbers, etched to define fully pointing readout cells in η, and four adjacent boards are grouped together to form cells in ϕ. Calibrations are performed using charge injections into the preamplifiers.

In the barrel, the innermost sampling is finely segmented into thin strip towers in η, providing precision position measurements, which help determine the flight path of photons and allow for π^0 rejection. The second and largest layer has coarser, square sampling towers, and is the main sampling for measuring the energy, as it absorbs most of the electromagnetic energy of a shower or jet. The third layer is coarser still and estimates the amount of energy from showers that escapes the EM calorimeter. To correct for

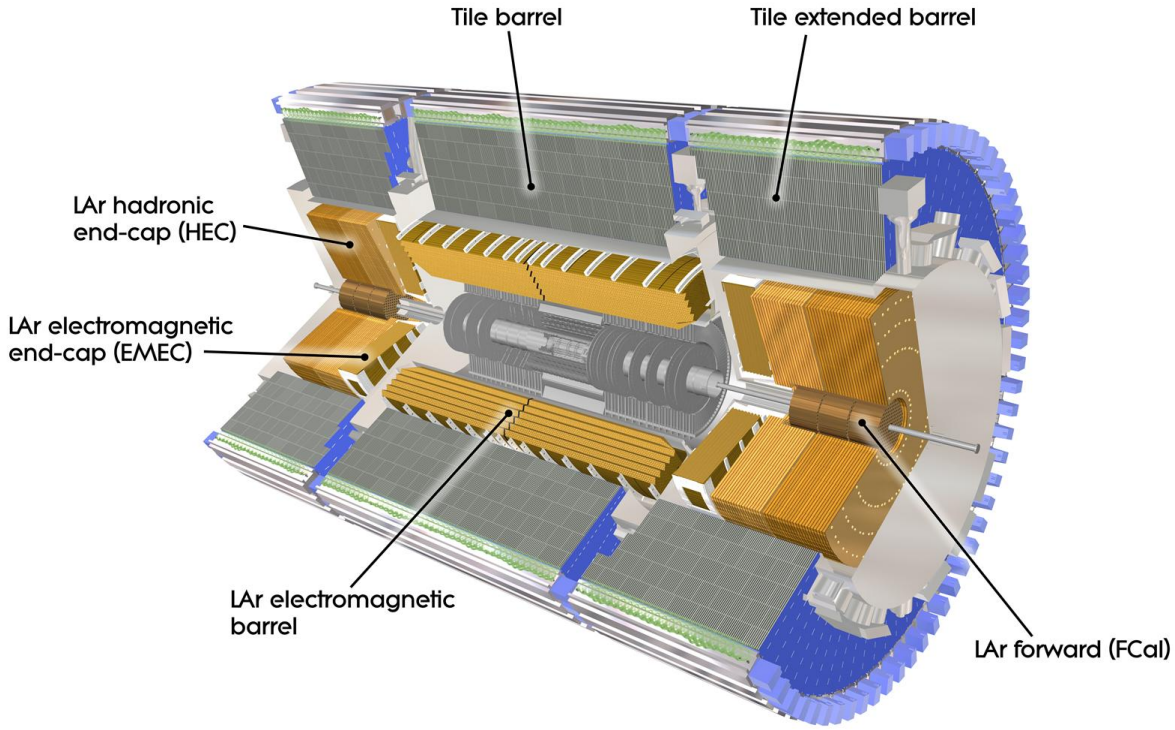

Figure 11: A schematic view of the ATLAS electromagnetic and hadronic calorimeters.

energy lost in the material before the calorimeter, a presampler is required, consisting of a liquid argon active layer with embedded electrodes. The endcaps have only two segmented layers and are of coarser granularity. To ensure that almost all the energy of high energy electrons and photons is absorbed, the total radiation lengths traversed in the EM calorimeter must be at least 24 X_0 in the barrel and 26 X_0 in the end-caps, however, fewer radiation lengths are desirable for higher resolution at medium energies. This is solved by varying the lead thickness with $|\eta|$.

There are around 170,000 channels in the electromagnetic calorimeter. Energy measurements range from ~10 MeV to ~3 TeV, with resolution of approximately 10 $\%/\sqrt{E} \oplus C$, where E is measured in GeV and the convolution constant is derived from properties of the detector material. The front-end electronics amplify and digitize the signal, and perform analog sums of energy deposits in the trigger towers, providing trigger signals within the required latency. In the central region, 60 cells are summed to form the trigger signal, with trigger towers covering 0.1×0.1 in η and ϕ, decreasing to 8 cells for $|\eta| > 2.5$, with towers covering 0.2×0.2.

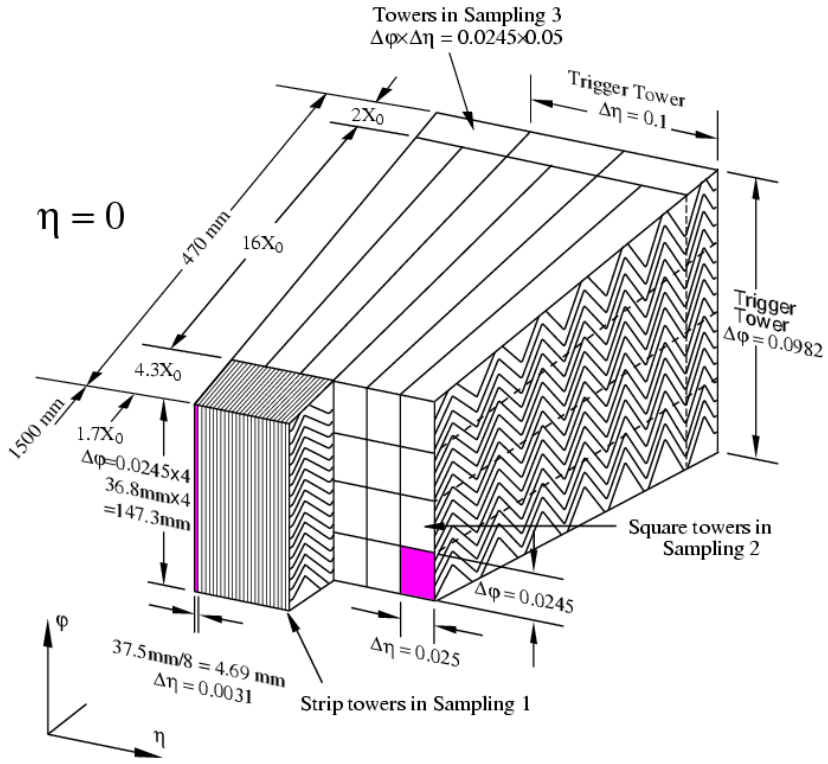

Figure 12: A section of the EM calorimeter barrel, showing the accordion structure, trigger tower and granularity of the different layers.

3.6 Hadronic calorimeters

Strongly interacting particles produced from collisions are fully absorbed in the hadronic calorimeters, which provide measurements for the efficient reconstruction of jets. Accurate jet identification is a key component of many physics analyses, and is particularly important for rejecting unwanted background QCD processes, which form the main background in many searches for new physics. Calorimeter performance is optimized for shower profile measurement whilst maintaining high resistance to radiation damage by having three separate systems with different measurement techniques as a function of $|\eta|$. These are the tile calorimeter, hadronic endcap calorimeter and forward calorimeter.

The tile calorimeter consists of a large central barrel and two smaller lateral extended barrels of steel absorbers interleaved with plastic scintillator tiles, covering $|\eta| < 1.7$. Each barrel has 64 module wedges, measuring $\delta\phi = 0.1$ rad, with wavelength shifting fibres coupled to each edge that convert ultraviolet light produced in the scintillator to visible light [46]. The fibres are grouped together to form pseudo-projective readout cells in slices of η, projected towards the nominal interaction point, with three radial sampling

depths. Fibres are read out at the outer edge of each module by two different photomultipliers (PMTs), providing redundancy and allowing signals produced from particles entering the scintillator at different positions to be partially equalized. The PMTs are housed in metal cylinders to shield them from the magnetic field produced by the solenoid and toroid. The signals produced from the photomultipliers are shaped, amplified and digitized by the front-end electronics, which perform analogue sums of subsets of channels to provide trigger towers for the Level-1 (L1) trigger [47]. System calibration is achieved using three control signals. Charge injection at the input of each electronic channel is used to monitor linearity and stability of electronics, a laser signal is used to monitor the readout chain, and a caesium-137 source on a hydraulic system can illuminate each tile, allowing the response of each cell to be equalized by adjusting PMT voltages.

The Hadronic Endcap (HEC) and Forward Calorimeters (FCAL), covering $1.5 < |\eta| < 3.2$ and $3.1 < |\eta| < 4.9$ respectively, use liquid argon technology due to the more intense radiation environment. Each hadronic endcap consists of two longitudinal sections containing 32 wedge shaped modules with copper absorber plates. The modules are biased at 1800 V with a typical electron drift time of ~400 ns. An important property of the HEC is its ability to measure the radiative energy loss of muons. The HEC and FCAL have similar readout electronics to the EM calorimeter modules, and share the same cryostat as the EM endcap calorimeter. The FCAL is composed of three longitudinally separated high density modules, the first with copper absorbers for EM measurements and the last two with tungsten absorbers for hadronic measurements. Very small liquid argon gaps are used to avoid ion build-up problems due to high particle fluxes and provide a faster signal than the EM calorimeter. Calibration is achieved using charge injection into the preamplifiers, and the FCAL system can be independently tested by injecting pulses at the front end crates.

3.7 Muon spectrometer

The outermost component of the ATLAS detector is a series of chambers for the detection and tracking of muons, shown in Figure 13. Typically muons are the only particles detectable within ATLAS that pass completely through the calorimeters, since they are minimum ionising particles and bremsstrahlung is suppressed due to their mass. The precision measurement of muons is important for ATLAS physics as they provide a clean signal for many processes. The muon spectrometer covers $|\eta| < 2.7$ and consists of tracking chambers with excellent momentum resolution, three large superconducting air-core toroids that bend the muon paths in the η direction, and a fast-response trigger chamber system. Chambers are

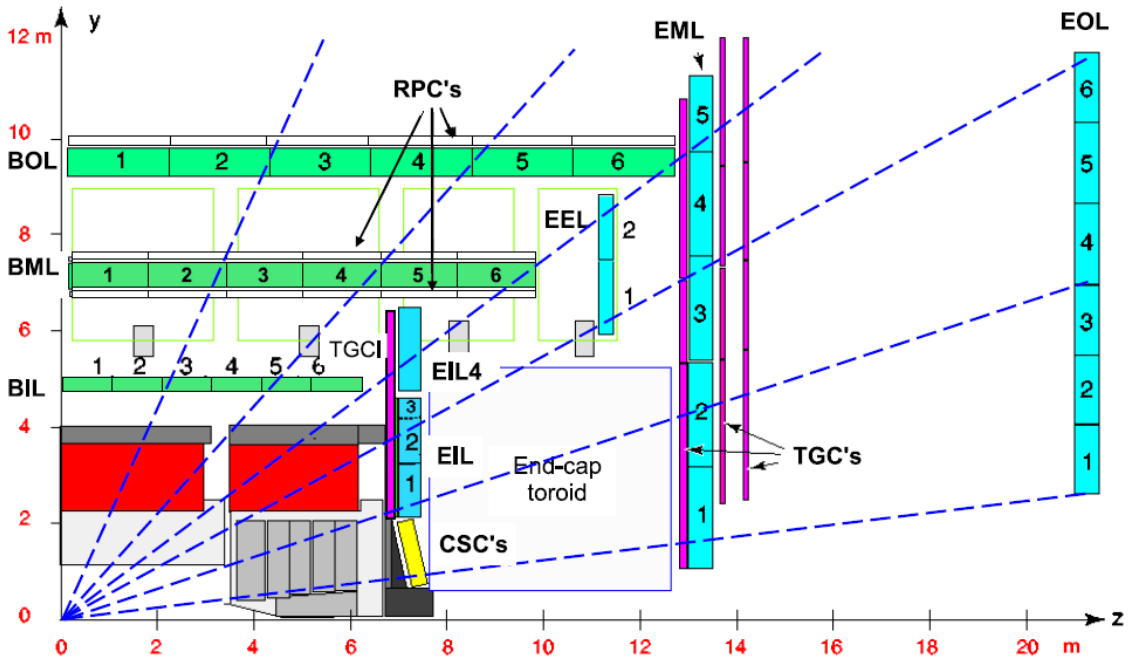

Figure 13: A section through the muon spectrometer systems in ATLAS, with MDTs highlighted in green and blue.

arranged in 'stations' of three concentric barrel layers with three wheels in each endcap, segmented in r-ϕ, forming eight small and eight large sectors projecting back to the interaction point.

Most of the precision space-point measurements in the spectrometer are performed by Monitored Drift Tube (MDT) chambers, formed from aluminium tubes 3 cm in diameter and between 0.9 and 6.2 m in length, and filled with 93 % argon and 7 % carbon dioxide. Each chamber has two multi-layers with 3 or 4 layers of tubes. A charged particle track typically has 20 drift tube measurements, identifying the track position in z r with a resolution of ~80 μm per tube, and ~35 μm per chamber. The MDTs are equipped with straightness monitors, temperature monitors, and magnetic field sensors to predict the effect of $E \times B$ on the drift time [48]. In the forward region, $2.0 < |\eta| < 2.7$, where there is a higher particle flux, precision measurements are made with faster, higher granularity Cathode Strip Chambers (CSC), consisting of multiwire proportional chambers with two cathode planes perpendicular to one another. Each chamber has four planes of anode wires extending out radially from the beam axis, surrounded by planes of cathode strips, and provide resolutions of 40 μm in r and 5 mm in ϕ. There are 32 CSCs with a total of 30,700 readout channels, which provide four position measurements in r-ϕ for a muon track passing through one of the CSC discs.

The trigger chambers reconstruct tracks originating approximately from the interaction point to iden-

tify muons with large transverse momentum, p_T, and provide a fast signal for the trigger decision. They also measure the ϕ coordinate of the muons and provide bunch crossing identification information. Two thresholds are used, a low-p_T threshold at 6 GeV, requiring coincidences between two trigger layers, and a high p_T threshold at 20 GeV that requires coincidence in all three layers. The resolutions for the low-p_T and high-p_T triggers are around 20 % and 30 % respectively, limited by energy fluctuation in the calorimeter, multiple scattering, and the length of the interaction region. The barrel trigger system uses Resistive Plate Chambers (RPCs) operated in avalanche mode, each unit composed of two gas volumes with independent parallel electrode plate detectors measuring the z and ϕ coordinates with space and time resolutions of 1 cm and 1 ns respectively, providing a total of 6 space-point measurements over the three layers. There are 606 RPCs in the spectrometer with a total of 373,000 readout channels. The end-cap uses Thin Gap Chambers (TGC) to provide the trigger signal, which consist of multi-wire chambers operated in saturated mode. Anode wires provide r measurements with space and time resolutions of 23 mm and 4 ns, and ϕ measurements are made using external pick up strips orthogonal to the anode with space and time resolutions of 37 mm and 4 ns. The TGC gas is 55 % carbon dioxide and 45 % n-pentane. There are 3588 TGCs with a total of 318,000 channels, providing 9 measurements for tracks passing through all four endcap wheels.

An essential part of the performance of the muon spectrometer is the alignment, which must be known precisely to achieve the design p_T resolution of 10 % for 1 TeV muons, corresponding to a track precision of < 50 μm. An optical alignment system and straightness monitors provide alignment in the barrel. This is not possible in the endcaps due to the presence of the cryostat and toroid magnet, and so alignment bars are used. These use a system of precision charge coupled devices and light emitting diodes to monitor alignment and transverse shape, and temperature sensors that control longitudinal thermal expansion. Track-based alignment procedures are performed and significantly improve knowledge of the muon spectrometer alignment. It is also necessary to know precisely the toroidal magnetic field for the momentum measurement, and this is monitored using 1800 Hall sensors mounted onto the MDTs and endcap cryostats.

3.8 The ATLAS trigger

Proton-proton collisions occur within ATLAS at a rate of up to 40 MHz, and with most of these collisions only producing soft QCD interactions, only a small fraction contain interesting physics events produced by a hard scatter process that need to be recorded and reconstructed for physics analysis. The ATLAS

trigger is a three-level hardware and software processing system that contructs a trigger decision based on geometrical Regions Of Interest (ROIs), reducing the incoming rate from 40 MHz to less than 1 kHZ for storage on disk. A flow diagram of the ATLAS trigger and DAQ is shown in Figure 14.

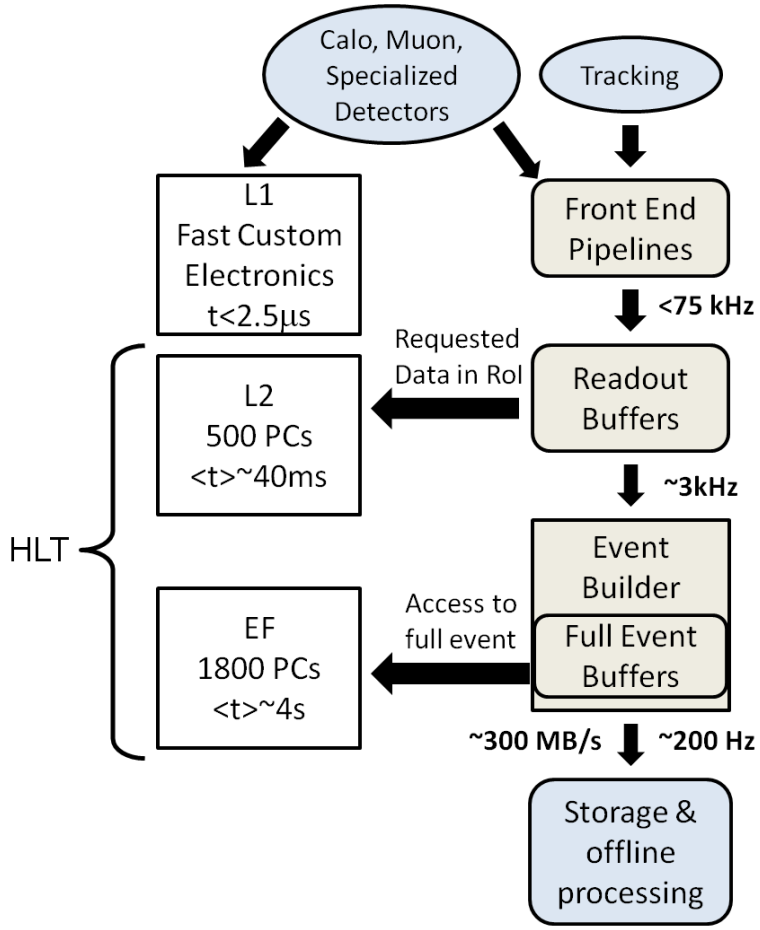

Figure 14: Flow diagram of the ATLAS trigger and data acquisition software architecture, with latencies and event rates at the three trigger levels [49].

3.8.1 Level-1 trigger

The Level-1 trigger is implemented in custom built electronics hardware and provides a decision to record an event or discard it within 2.5 μs, corresponding to the on-detector buffer sizes, and reduces the event rate from 40 MHz to around 75 kHz. The trigger decision is based on reduced granularity data received from the calorimeters and muon spectrometer. Energy deposits summed in trigger towers from the calorimeter readout are scanned to determine if they are characteristic of jets, electrons, photons, or hadronic decays of τ leptons, and also for global signatures such as missing transverse energy and total

transverse energy. Muon multiplicities are estimated from track information in the RPC and TGC, and programmable hit coincidence logic identifies high-p_T muon candidates. The central trigger processor forms logical combinations of the results from the L1Calo and L1Muon, passing events that satisfy conditions set in the trigger menu, and can apply a prescale to reduce the rates of trigger menu items that are using up excessive amounts of the available bandwidth. The prescale, p, is chosen so that $1/p$ events are recorded. If an event passes the trigger an L1 accept signal is sent to the readout drivers on the detector-specific front-end electronics and the event is passed to the High Level Trigger (HLT), along with the ROI information containing coordinates and the threshold or isolation conditions that satisfied the criteria of the trigger menu item that the event passed.

3.8.2 High level trigger

The HLT is composed of the Level-2 (L2) trigger and the Event Filter (EF) software algorithms running on dedicated processor farms. The L2 trigger uses the full detector granularity output in energy and position for the ROIs passed down from L1, allowing higher p_T thresholds, and reduces the event rate from 75 kHz to ~2 kHz with a latency of 40 ms. The information processed at L2 amounts to about 1-2 % of a total event, and includes track information from the inner detector, allowing improved particle identification such as the separation of electrons and photons. The trigger selection is implemented in selection sequences, using feature extraction algorithms to reconstruct a physics candidate that is validated by a hypothesis algorithm, producing a trigger element. For an event to be accepted, a list of trigger elements must be satisfied leading to the complete execution of a trigger chain, validating a trigger signature. If an event passes the L2 trigger, all detector information is sent to the event builder, where the event is fully assembled and sent to the EF. The EF reduces the final event rate to 200 Hz and the mass storage rate to 320 MB/s, and has a much larger decision time of ~4 s. The event selection process has the same structure as L2, except that the EF reconstruction algorithms are the same as those used for full offline event reconstruction in the ATLAS analysis environment ATHENA, and all available event data is now utilized. Events passing the EF are categorized into inclusive streams, such as Egamma, JetTauEtmiss, or Muons, corresponding to the physics candidate that validated the trigger signature, and are then permanently recorded to disk.

Chapter 4

Reconstruction

The digitised signals from the various detector sub-systems from events that pass the ATLAS trigger are recorded as raw data object information, consisting of hits in the inner detector and muon chambers, and digitised energy signatures from the calorimeters. The recorded event data is passed through the ATLAS offline reconstruction framework ATHENA [50], which is built from a series of software algorithms that convert the raw data into physics objects such as tracks, vertices, electrons, muons, and jets, and produce the kinematic and object quality data that is required for physics analysis. Simulated Monte Carlo events are first passed through a full simulation of the ATLAS detector [51] in the GEANT4 software [52] before being reconstructed in ATHENA by the same algorithms used for data.

4.1 Tracks

Charged particle tracks are reconstructed by algorithms that use space points derived from hits in the pixel and SCT detectors. These algorithms perform two main processes: pattern finding, consisting of both a global pattern search and local pattern recognition, and track fitting. Track reconstruction in ATHENA is performed with pattern recognition algorithms that use a global-χ^2 method. These perform the main inside-out track reconstruction, which extends seeds from the silicon detectors out to the TRT and reconstructs primary tracks, followed by the outside-in reconstruction, which starts with TRT-based seeds and extends inwards, reconstructing secondary tracks from conversions, material interactions and long-lived particle decays.

Inside-out reconstruction starts by creating three-dimensional space points from the silicon detector measurements. This is simple for hits in the pixels, since they provide a two-dimensional local measurement, but more complicated for the SCT measurements, since obtaining a single space point requires the readout of two different module streams. The space point collections are processed and used to seed the track candidate search within the inner detector. The global part of the pattern recognition, the seed search, can be constrained by the z vertex, where z vertices are built from pairs of space points in the pixel detector, or can remain unconstrained, which leads to a significantly higher number of initial track seeds [53]. The space point seeds provide directional information that guides the search for associated hits for the track candidate, initiating the local part of the pattern recognition. The track fitting is then

performed using the global χ^2 method to follow the trajectory and include successive hits in the track candidate fit. Outliers with large χ^2 are rejected.

The seed track finding produces a large number of track candidates, many of which are incomplete, have shared hits or are fake tracks, where the majority of hits do not originate from a single particle. The effect of such phenomena on the identification of heavy flavour jets is discussed in Section 6.4. To remedy this, the tracks are ranked in their likelihood to have been produced by real particles based on a 'track scoring' strategy, and tracks that do not score high enough are ignored [54]. An example of the track scoring criteria is given in Figure 15. The tracks that pass this selection are associated to hits in the TRT, and act to extend the inner detector tracks.

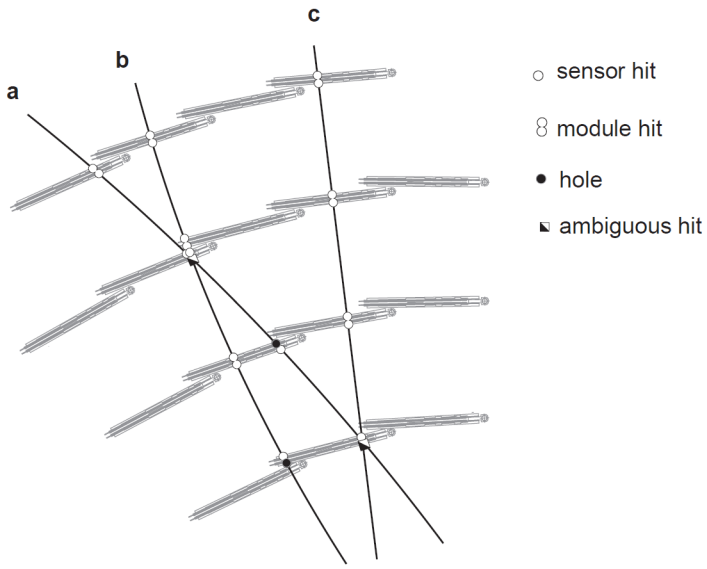

Figure 15: Example illustration of how ambiguous tracks can be formed in the SCT. A hit on both sides of a module is scored higher than two single hits without a hit on a backside module. Hits in an overlap region (track b) are high scored. Holes in a track, where a hit is expected, but not found, get a penalty in the track score.

The outside-in reconstruction is necessary to correct for a number of effects. Some of the inital track seeds might not be found by the inside-out method, or may be discarded due to shadowing from ambiguous hits. Also, tracks from secondary vertices produced by the decay of long-lived particles, such as K_s, or photon conversions, may not have sufficient hits in the silicon detectors to be reconstructed by the inside-out algorithm. The outside-in method first performs a global pattern search in the TRT, using projective planes since there is no information of the coordinate along the straw direction. This is followed by local pattern recognition that builds track segments using the global χ^2 method, also utilising

the drift-time information. These track segments are then backtracked into the silicon detector to form track candidates.

4.2 Vertices

Primary vertex reconstruction consists of two main processes: primary vertex finding, where charged particle tracks are associated to a vertex candidate, and vertex fitting, where the vertex position is reconstructed and the corresponding covariance matrix is determined. Reconstruction begins with a selection of tracks that are likely to originate from the interaction region that pass the selection criteria shown in Table 2. A vertex seed is then found from the global maximum of the distribution of the z coordinates of the tracks with respect to the beam spot centre. The vertex is then fitted by a χ^2 based fitting algorithm that takes as input the vertex position and the nearby tracks, with outlier tracks with large χ^2 weighted down. Any tracks incompatible with the vertex by more than $\sim 7\sigma$ are considered outliers and removed from the vertex fit and used to construct a new seed vertex. This process is then repeated to produce multiple seed vertices that compete to gain tracks until there are no unassociated tracks left or no additional vertex can be constructed.

Since there is generally more than one proton-proton interaction in the colliding bunches, known as pileup, there can be more than one reconstructed collision vertex. By default, the primary vertex with the highest Σp_T^2 of tracks associated to it is identified as the hard scatter process that fired the trigger [56].

Parameter		Cut Value
p_T	>	150 MeV/c
$\lvert d_0 \rvert$	<	4 mm
$\sigma(d_0)$	<	5 mm
$\sigma(z_0)$	<	10 mm
Silicon hits	>	5
SCT hits	>	3

Table 2: Track selection criteria for vertex reconstruction [55].

4.3 Electrons

The standard algorithm for reconstructing electrons in ATHENA starts from reconstructed clusters in the cells of the electromagnetic calorimeter and builds identification variables based on information from both the calorimeter and the inner detector. Electromagnetic clusters are reconstructed using a 'sliding window' algorithm that maps the calorimeter cells onto a grid of towers with $\Delta\eta = 0.025$ and moves a window of 5×5 towers over this grid [57]. A cluster is identified as an electron seed if the transverse energy in the window is greater than 3 GeV. Corrections must be applied to the cluster position and energy to take account of the varying particle impact position and energy containment, and to correct for the transition region between the calorimeter barrel and endcap. These corrections are discussed in detail for the $Z + b$ jet cross-section measurement in Section 7.5.3). There is also a calibration between the different calorimeter layers that accounts for the energy scale, the loss of energy upstream and from dead material, and longitudinal leakage. Electron seeds are matched to charged particle tracks reconstructed in the inner detector, provided the track does not originate from photon conversion. This is done by extrapolating the inner detector track to the calorimeter and matching it to the cluster within a broad window of $\Delta\eta \times \Delta\phi = 0.05 \times 0.10$. When more than one track can be associated to a cluster, the track is chosen with the ratio of the cluster energy to the track momentum, E_{clus}/p_{trk}, closest to 1.

In hadron-hadron collisions, QCD processes dominate, and the jets produced from these processes can often fake electrons since they produce charged particle tracks in the inner detector and deposit energy in the EM calorimeter. To separate true electrons from fakes, a range of electron identification requirements are imposed on the electron candidates. These are based on the different behaviour of electrons and jets and the response of the sub-detector, for example, jets are broader and have more leakage in the hadronic calorimeter than electrons, and the TRT has the capability to separate electrons and pions. Identification cuts are therefore performed on variables reflecting the shower shape in the calorimeter and information from the TRT. Further background reduction can be achieved from cuts on the track quality, such as a minimum number of hits in the pixel and SCT detectors, and constraints on track-cluster matching. There are three main sets of cuts that are defined in ATHENA: *loose*, *medium*, and *tight*. These allow the electron identification to be tailored to the analysis, depending on whether efficiency or rejection is favoured. The loose, medium and tight identification cuts are summarised in Table 3, where $\Delta R = \sqrt{(\Delta\eta)^2 + (\Delta\phi)^2}$.

Type	Description	Variable Name
Loose Cuts		
Detector acceptance	$\|\eta\| < 2.47$	
Hadronic leakage	Ratio of E_T in the first sampling of the	
	hadronic calorimeter to E_T of the EM cluster	
Second layer	Ratio in η of cell energies in 3×7 versus 7×7 cells	R_η
of EM calorimeter	Ratio in ϕ of cell energies in 3×3 versus 3×7 cells	R_ϕ
	Lateral width of the shower	
Medium cuts (includes loose cuts)		
First layer of EM	Difference between energy associated with	ΔE_s
calorimeter	the second largest energy deposit	
	and energy associated with the minimal value	
	between the first and second maxima	
	Second largest energy deposit normalised	R_{max2}
	to the cluster energy	
	Total shower width	w_{stot}
	Shower width for three strips around maximum strip	w_{s3}
	Fraction of energy outside core of three central strips	F_{side}
	but within seven strips	
Track quality	Number of hits in the pixel detector (> 0)	
	Number of hits in the pixels and SCT (> 8)	
	Transverse impact parameter (d_0 < 1 mm)	
Tight (isol) (includes medium cuts)		
Isolation	Ratio of transverse energy in a cone $\Delta R < 0.2$	
	to the total cluster transverse energy	
Vertexing-layer	Number of hits in the vertexing-layer (> 0)	
Track matching	$\Delta\eta$ between the cluster and the track (< 0.005)	
	$\Delta\phi$ between the cluster and the track (< 0.02)	
	Ratio of the cluster energy to	E/p
	the track momentum	
TRT	Total number of hits in the TRT	
	Ratio of the number of high-threshold	
	hits to the total number of hits in the TRT	
Tight (TRT) (includes tight (isol) except for isolation)		
TRT	Same as TRT cuts above, but with	
	tighter values corresponding to about 90 %	
	efficiency for isolated electrons	

Table 3: Definition of variables used for loose, medium and tight electron identification cuts [58]. The cut values are given explicitly only when they are independent of η and p_T.

The electron reconstruction efficiency in 2011 and 2012 data and in simulation is shown in Figure 16. The reconstruction efficiency of electrons is defined with respect to electromagnetic clusters built using a sliding window algorithm, and is measured in $Z \rightarrow e^+e^-$ events using the 'tag and probe' method [60], with no identification requirements applied. The cluster building efficiency for electrons in these events is close to 1.

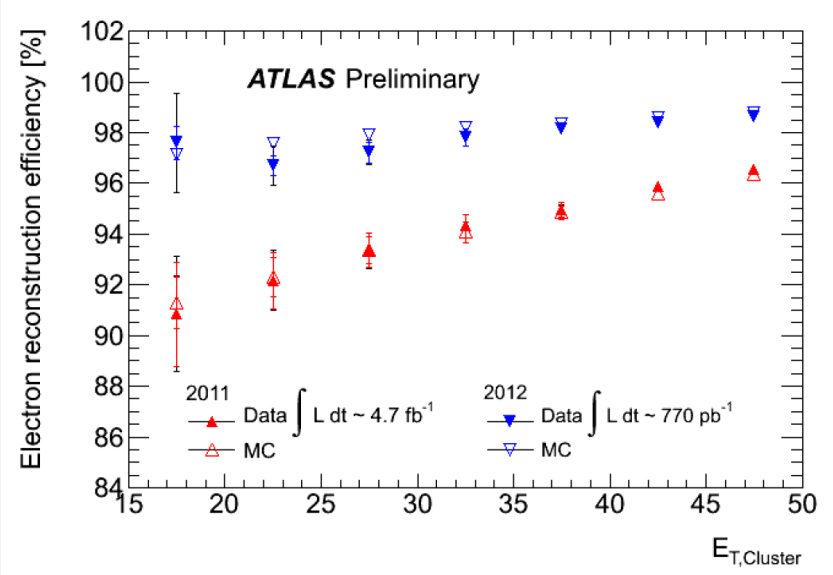

Figure 16: The reconstruction efficiency (including the requirements on the track quality) as a function of the electron transverse energy, for data (filled markers) and MC (open markers) from 2011 (red up triangles) and 2012 (blue down triangles). The total (statistical and systematic) uncertainty is displayed. Electrons reconstructed in the calorimeter transition region $1.37 < |\eta| < 1.52$ *are not taken into account [59].*

4.4 Muons

The reconstruction of muons within the muon system involves four main steps: the identification of regions of activity (ROA) defined by hits in the muon trigger chambers, the reconstruction of local straight track segments in each of the muon stations that measure the ROA with pattern recognition algorithms, the construction of segment tagged muon track candidates from the combination of track segments from different muon stations by the Muonboy algorithm [61], and finally the global track fit of the muon track candidates throughout the muon system. The reconstruction process must also back-track from the muon system through the calorimeters and inner detector to the beam region to account for energy losses and and multiple scattering. This requires accurate knowledge of the material traversed

to correct the muon momentum, which is done using an energy loss parametrisation.

Once a muon track candidate is found in the muon system, it is extrapolated back to the vertex, and matched to a track reconstructed independently in the inner detector to form a combined muon. The combination of muon measurements from the muon system and the inner detector improves the momentum resolution and allows the rejection of muons from secondary interactions as well as those from in-flight decays of pions and kaons. The matching and combination of the tracks is performed by the STACO program [62]. To match the segment tagged muon track with an inner detector track, the match χ^2 is calculated, defined as the difference between the two track vectors weighted by their combined covariance matrix, and if this value is less than a chosen threshold the tracks are considered matched. Once a match is found, the muon spectrometer track is removed from the search so that the track collection does not contain any combined muon tracks constructed from the same extrapolated muon spectrometer track. The STACO program then performs a statistical combination of the track vectors and covariance matrices from segment tagged muon tracks and inner detector tracks to obtain the full track parameters.

For $p_T > 6$ GeV the average muon reconstruction efficiency is above 98% [63]. The efficiency for combined muons and combined + segment tagged muons as a function of p_T for $0.1 < \eta < 1.1$ in 2010 data and simulation, determined with the tag-and-probe method using muons from decays of J/Ψ mesons, is shown in Figure 17. The muon reconstruction efficiency decreases quickly with decreasing p_T because the inhomogeneous magnetic field in ATLAS makes accurate tracking of low p_T muons difficult. Also, the energy lost by low p_T muons inside the calorimeters is comparable to their energy, particularly in the barrel region, meaning they may not deposit energy in the muon system. The efficiency is also reduced in certain regions due to the limited geometrical acceptance of the muon spectrometer.

4.5 Jets

Jets are reconstructed from calorimeter signal towers and topological cell clusters by jet-finding algorithms that recombine the full four-momentum of hadronic particles in jets. There are three main types of algorithms: fixed-size cone algorithms, sequential recombination algorithms, and algorithms based on event shape analysis. The type of algorithm chosen depends on the topology of the hadronic final state that is being measured. In ATHENA, the same jet-finding code can be run on objects such as calorimeter signal towers, topological cell clusters in the calorimeters, reconstructed tracks, and generated particles and partons in the simulation.

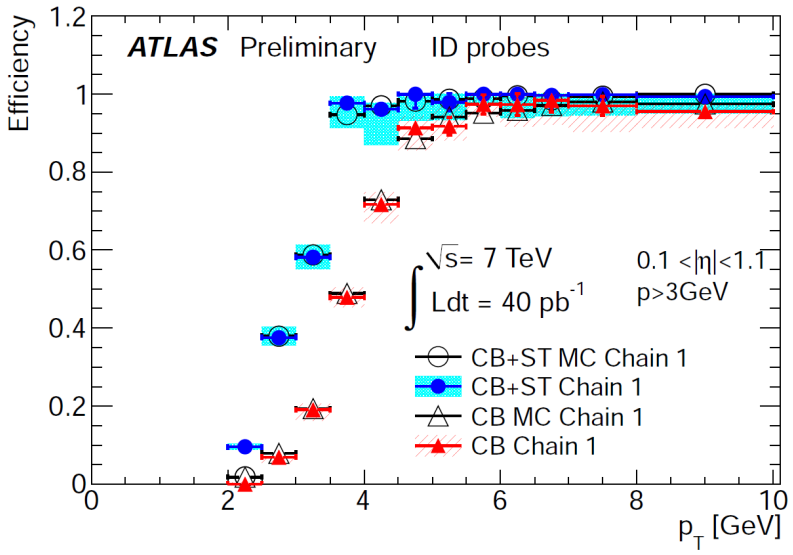

Figure 17: Efficiency for combined muons (CB) and combined + segment tagged (ST) muons with respect to calorimeter-tagged muons as a function of p_T for $0.1 < \eta < 1.1$ in data and simulation. The error bars represent the statistical uncertainties while the band around the data points represents the statistical and systematic uncertainties added in quadrature [63].

Any jet-finding algorithm must satisfy a set of theoretical and experimental requirements. Theoretically, the jet reconstruction must be infrared safe, collinear safe, and order independent. Infrared safety requires that the presence of additional soft particles between two hard particles in the same jet should not affect the recombination of these two particles into a jet, and conversely the absence of any additional soft particles should not affect reconstruction. Generally, any soft particles not from the fragmentation of the hard scattered parton should not change the number of reconstructed jets. Collinear safety requires the jet reconstruction not be affected by the fact that a certain amount of the jet transverse momentum is carried by one particle in the jet. For the jet reconstruction to be order independent, the same hard scattering process should be reconstructed at parton, particle, and detector level.

Jet reconstruction should also take into account features of the detector and be independent of the detector technology, i.e. the jet and its kinematic variables should not depend on the signal source, or be affected by the finite detector resolution, and all detector signals must be stable. The jet reconstruction should be minimally affected by any additional activity in the event, such as changes in the underlying event and varying instantaneous luminosity, which affect the number of multiple interactions. In general, all physically interesting jets from energetic partons must be identified with high efficiency.

The jet reconstruction algorithm used for the analysis in this thesis, and in many other ATLAS physics measurements, is the anti-k_t jet clustering algorithm [64]. This is a sequential recombination algorithm based on the characteristic behaviour that soft particles usually cluster with hard particles before clustering with other soft particles. The algorithm operates by first constructing a list of entities, containing particles and pseudojets, and defines the distances between pairs of these entities, d_{ij}, and the distance between each entity and the beam, d_{iB}:

$$\begin{aligned} d_{ij} &= \min(k_{ti}^{2p}, k_{tj}^{2p}) \frac{\Delta_{ij}^2}{R^2}, \\ d_{iB} &= k_{ti}^{2p}, \end{aligned} \tag{20}$$

where $\Delta_{ij}^2 = (y_i - y_j)^2 + (\phi_i - \phi_j)^2$ and k_{ti}, y_i and ϕ_i are respectively the transverse momentum, rapidity and azimuth of particle i. In addition to the usual radius parameter R, there is a parameter p to govern the relative power of the energy versus geometrical Δ_{ij} scales [64].

The clustering proceeds by identifying the smallest of these distances. If $d_{ij} < d_{iB}$, the entities i and j are combined, whereas if $d_{iB} < d_{ij}$, i is labelled a jet and removed from the list. Distances are then recalculated and this process is repeated until there are no entities left. An important feature of this algorithm is that soft emissions do not change the jet shape, whereas hard emissions do, therefore the jet boundary is resilient with respect to soft radiation, but flexible with respect to hard radiation and the sub-structure of the jet. If a hard particle has no hard neighbours within twice the configurable radius parameter R, it will accumulate all the soft particles within that radius, resulting in a perfectly conical jet. If another hard particle is present such that $R < d_{ij} < 2R$, there will be two hard jets, and the shape of the jets will depend on their relative transverse momenta: the jet with the larger momentum will be more conical. However, if the two hard particles lie within $d_{ij} < R$, they will be reconstructed in the same jet, with the jet direction dependent on their relative transverse momenta.

A unique property of the anti-k_t algorithm is that the 'area' of a jet, a measure of its susceptability to radiation, is not affected by the jet p_T. The impact of the underlying event and pileup on the momentum resolution for jets is related to both the typical value of the area, and to the extent of the fluctuations of the area. These fluctuations are close to zero for the anti-k_t algorithm, making it one of the more stable reconstruction algorithms with good jet resolution. Other jet reconstruction algorithms used in ATLAS are discussed in [65].

4.6 Missing transverse energy

The Missing Transverse Energy (MET) resulting from particles that do not deposit any energy in the detector is calculated using reconstructed energy deposits from the calorimeter and muons reconstructed in the muon spectrometer. Low energy particles may not deposit enough energy in the calorimeter, and some muons may not be fully reconstructed due to the muon spectrometer acceptance. To recover such particles, tracks from the inner detector may be used. Calorimeter clusters must be associated to physics objects in the correct order for the calibrations to be applied correctly. Electrons are associated first, followed by photons, hadronically decaying taus, jets and muons. There are various approaches and calibrations when reconstructing the MET. For the analyses in this thesis, the calibration used is 'METRefFinal', which is discussed in detail in [67]. Once the calibrations are applied, the energy cells associated to each object are combined to construct a negative vectorial sum. The vectorial sums from each object, i, are then combined to calculate the x and y missing transverse energy components using:

$$E_{x(y)}^{miss} = \sum_{i=0}^{N} E_{x(y)}^{miss\ i} \tag{21}$$

where N is the total number of objects. The total MET and its direction are then given by:

$$\begin{aligned} E_T^{miss} &= \sqrt{(E_x^{miss})^2 + (E_y^{miss})^2} \\ \phi^{miss} &= \tan^{-1}(E_y^{miss}/E_x^{miss}) \end{aligned} \tag{22}$$

The MET is generally reconstructed within the detector acceptance $\eta < 4.9$, except for the muon terms, since muon tracks are reconstructed within $\eta >= 2.7$.

4.7 *b* quark jets

Many physics analyses in ATLAS require the identification of jets originating from the decay of bottom quarks, which are often a sign of interesting physics. This is performed using various b tagging algorithms, which identify or "tag" jets as originating from a b decay, thus suppressing background processes that contain predominantly light-flavour jets that often arise from QCD interactions. This background suppression is essential for precision measurements in the top quark sector and in the search for the Higgs boson, and may also be critical to achieve an understanding of the flavour structure of any new physics revealed at the LHC.

There are two main types of b tagging algorithm that exploit the fact that b hadrons have a relatively long lifetime of ~1.5 ps, and therefore have a measureable flight path in the detector of typically around

a few millimetres. Vertex-based algorithms explicitly reconstruct the secondary vertex from the b decay by selecting and fitting tracks from the jet. Impact-parameter based algorithms select b jets based on the large non-zero impact parameters of charged particle tracks in jets produced by the decay of a b hadron.

There are three quantities that must be determined in order to utilise b tagging: the b tagging efficiency , the c tagging efficiency, and the mistag efficiency. The b tagging efficiency, ϵ_b, is defined as the fraction of true b jets produced by collisions that are selected by the b tagging algorithm. The c tagging and mistag efficiencies are defined as the probability of mistakenly tagging a jet originating from a c quark or a light-flavour parton ($u-, d-$, s-quark or gluon). The true number of *b, c or l* jets in data is generally unknown, and so the efficiencies and mistag rate are usually determined from Monte Carlo simulation. The b tagging algorithms must therefore be calibrated for use in physics analyses to correct for differences between data and simulation. This is discussed in detail in Chapter 6.

The first stage of most b tagging algorithms is to reconstruct the decay of neutral strange particles (V^0 decays), such as K_s^0 or Λ^0, and to remove tracks from such decays since they can mimic the tracks produced by b hadron decays. This is done in the preselection, which cuts on the track transverse and longitudinal impact parameters, d_0 and z_0 respectively, to reject most tracks from other long-lived particle decays and secondary interactions.

4.7.1 The SV0 *b* tagging algorithm

The SV0 b tagging algorithm is a vertex-based algorithm that selects jets originating from b quarks by explicitly reconstructing displaced (secondary) vertices from the tracks of decay products of b hadrons. The SV0 algorithm takes as input a list of tracks that are associated to a jet in the calorimeter that are unlikely to be associated to the primary vertex and attempts to reconstruct an inclusive secondary vertex. The tracks used as input for SV0 must pass the track selection cuts shown in Table 4. Tracks with large χ^2 with respect to this reconstructed secondary vertex are iteratively removed until the vertex fulfils a set of quality criteria. Two-track vertices are removed if they are consistent with the masses of the K_s^0 or λ^0, or if they are located at one of the pixel barrel layers and are therefore likely to have originated from material interactions. The signed decay length significance, $L/\sigma(L)$, where L is the signed decay length and $\sigma(L)$ is its uncertainty, illustrated in Figure 18, of the reconstructed vertex with respect to the primary vertex is calculated, and if this is above a certain value, the jet is tagged as a b jet. The sign of $L/\sigma(L)$ is given by the projection of the decay length vector onto the jet axis. The sign is positive for true b jets and can be negative due to reconstruction and resolution effects. More details on the SV0 b tagging

algorithm can be found in [84].

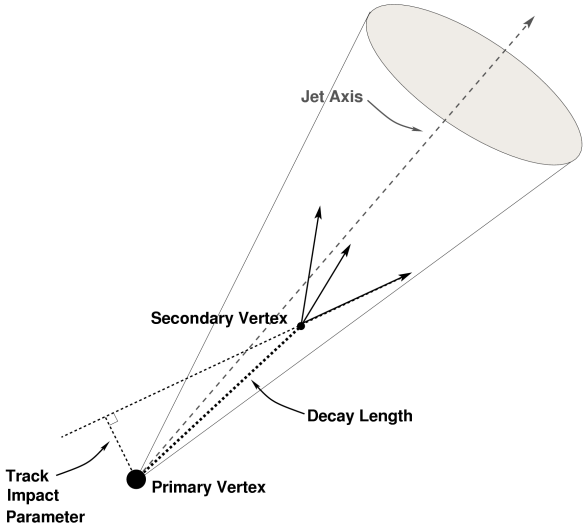

Figure 18: Illustration of primary and secondary vertices [68]. A secondary vertex with a large decay length indicates the jet was produced by the decay of a long-lived particle. The secondary vertex is reconstructed from charged particle tracks in the jet, which have a large impact parameter significance with respect to the primary vertex.

Track Selection		
p_T	>	0.5 GeV
d_0^{PV}	<	2 mm
$z_0^{PV}\sin\theta$	<	2 mm
$\sigma(d_0^{PV})$	<	1 mm
$\sigma(z_0^{PV})$	<	5 mm
χ^2/ndof	<	3
Pixel hits	>	1
SCT hits	>	3
Pixel + SCT hits	>	6

Table 4: SV0 track selection, where PV is the primary vertex.

The cut value on the signed decay length significance for tagging b jets with SV0 is chosen to produce a specific b tagging efficiency in simulated $t\bar{t}$ events. Figure 19 shows an example of the $L/\sigma(L)$ distribu-

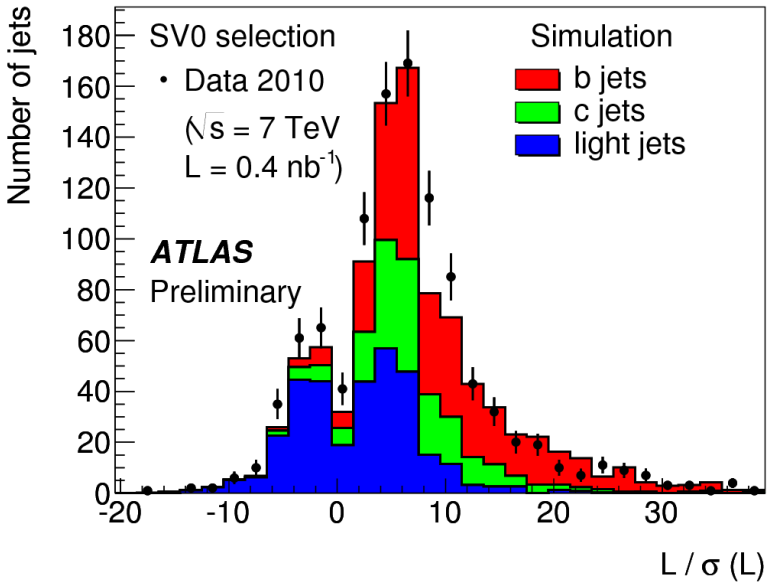

Figure 19: The three-dimensional decay length significance, signed with respect to the calorimeter jet axis, for secondary vertices reconstructed in 2010 data events (black dots). Also shown is the expectation from simulated events (filled histograms for the various flavors), in non-diffractive minimum bias events, normalized to the number of jets in the data [68].

tion for 2010 data and simulation, separated into components from bottom, charm, and light-flavour jets. The flavour of the jet in simulation is determined by matching a reconstructed hadron within a cone of specified radius in η and ϕ to a hadron generated by the particle event generator.

An advanced secondary vertex tagger, SV1, reconstructs the secondary vertex and takes the likelihood ratio of various properties of the vertex and the jet to produce a jet weight. The SV1 weight is used as an input parameter for some of the neural network b tagging algorithms, such as JetFitterCombNN and MV1.

4.7.2 The Jet Fitter *b* tagging algorithm

The JetFitter algorithm [69] uses a special secondary vertex reconstruction algorithm that exploits the topological structure of b and c hadron decays inside jets to seperately reconstruct the b and c decay vertices, based on the hypothesis that the b quark decays to a c quark and that the vertices and the primary event vertex lie on the same line, which represents the b hadron flight path. The JetFitter algorithm takes as input a set of preseleceted tracks in the form of helix track parameters and covariance matrices. The track parameters are defined at the point of closest approach in the transverse plane with respect to a

chosen reference point (the 'perigee' distance). The track measurements are used to iteratively update the vertex fit, which is performed by a 'Kalman filter'-based algorithm, with one update step for every track. The Kalman filter algorithm must be provided with a 'measurement equation', describing the relation between the track parameters to the vertex position and the track momentum at the vertex. The JetFitter algorithm then updates a set of parameters that describe directly the primary vertex and the b-to-c decay cascade to determine the b hadron flight axis.

Once the primary vertex and the flight axis have been defined, an initial χ^2 fit is performed based on the assumption that each track represents a single vertex along the flight axis. Clustering is then performed for all combinations of two vertices that lie on the flight axis, plus the primary vertex, to fill a table that represents the probabilities for any pair of vertices to form a single vertex, and for this vertex to be compatible with the rest of the decay chain. The vertices with the highest probability are merged and this process is iterated until there are no vertices left with a probability above a certain threshold. This procedure produces a decay topology with well defined vertices along the b hadron flight axis. The b tagging algorithm separates b jets from c and l jets by defining a likelihood function using a set of discrete variables that describe the decay topology and the vertex information, combined using a trained artificial neural network. A cut is then applied to the neural net ouput value to select a sample of b jets with a given tagging efficiency and light jet rejection. The JetFitter algorithm is combined with the impact-parameter based IP3D algorithm, which uses the tranverse and longitudinal impact parameter significances with a log-likelihood probability function, to produce the JetFitterCombNN neural network response. The JetFitter and IP3D variables and the JetFitterCombNN responses are shown in Table 5. Figure 20 shows the distribution of the JetFitterCombNN neural network output in 2011 data and in simulated data generated by the PYTHIA Monte Carlo program.

4.7.3 The MV1 neural network *b* tagging algorithm

The MV1 b-tagging algorithm is based on a multivariate neural network response using the output weights of the JetFitter+IP3D, IP3D and SV1 algorithms as input. This is the preferred b tagging algorithm for use with 2011 ATLAS data since it gives the best light jet rejection for the highest b tagging efficiency out of all the available tagging algorithms with the same level of agreement between data and simulation.

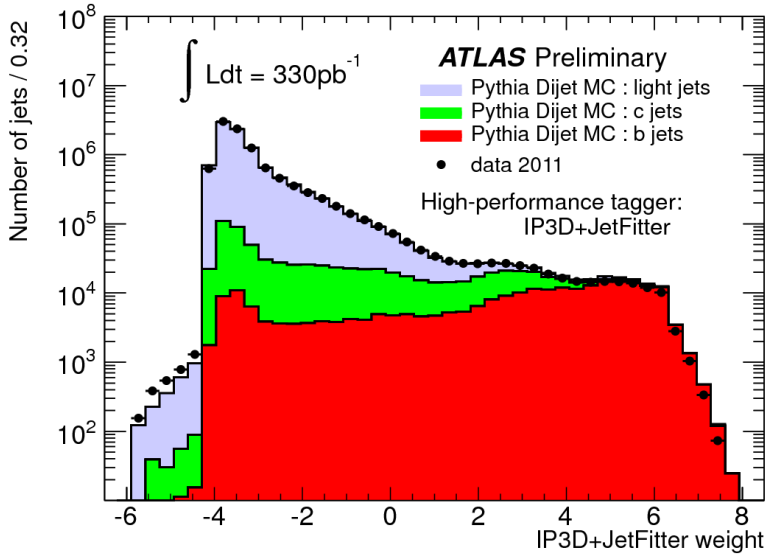

Figure 20: Distribution of the output of the IP3D+JetFitter tagging algorithm in 2011 data (black dots) and for simulated data (filled histograms for the various flavors) [70].

4.7.4 Estimating the *b* tagging efficiency in data

The *b* tagging efficiency is defined as the fraction of jets originating from the decay of a *b* quark that are tagged by the tagging algorithm. To calculate the efficiency, one must know the true number of *b* quarks that were originally in the sample. This value is known for Monte Carlo simulation, and there are ways to estimate it in real data.

Often *b* jets contain soft muons resulting from the semileptonic decay of the *b* quark, and the *b* tagging efficiency in data can be calculated for the subset of all *b* jets that contain a muon. This is performed by taking the muon transverse momentum relative to the combined muon-plus-jet axis, p_T^{rel}. The p_T^{rel} spectrum for *b* jets is harder than that for *c* and light flavour jets, since semileptonic *b* quark decays will generally produce muons with larger p_T. Templates of p_T^{rel} are constructed from simulated data for each of the *b*, *c* and light components, and fitted to the p_T^{rel} spectrum in data to estimate the proportion of each jet flavour in the data sample. This method is used to estimate the fraction of *b* jets before and after *b* tagging.

The performance of any *b* tagging algorithm is dependant on p_T and η, thus the p_T^{rel} templates are fitted to data according to these quantities. The p_T bins used are $\{20, 30, 60, 90, 140\}$ GeV. The η bins are $\{0.0, 1.2, 2.5\}$.

This method is limited to p_T <140 GeV for 2011 data, since for jets with large transverse momentum

Algorithm	Name	Nature	Description
JetFitter	Mass	Continuous	Invariant mass of secondary vertex fitted tracks.
JetFitter	eFrac	Continuous	Fraction of energy of fitted tracks realtive to all tracks in jet.
JetFitter	3D d_0 sig.	Continuous	3D impact parameter significance of secondary vertex.
JetFitter	nVtx	Discrete	Number of fitted vertices with two or more tracks.
JetFitter	n1TrkVtx	Discrete	Number of vertices where single track crosses fitted b hadron line of flight.
JetFitter	nTrkAtVtx	Discrete	Total number of tracks in the secondary vertex.
IP3D	IP3D Weight	Partially Continuous	Output of the IP3D tagging algorithm.
JetFitterCombNN	p_b	0.0-1.0	Neural net probability for b jet
JetFitterCombNN	p_c	0.0-1.0	Neural net probability for c jet
JetFitterCombNN	p_u	0.0-1.0	Neural net probability for light jet
JetFitterCombNN	$ln(p_b/p_u)$	–	Discriminates b jets from light jets
JetFitterCombNN	$ln(p_b/p_c)$	–	Discriminates b jets from c jets

Table 5: Definitions for JetFitter and IP3D inputs and subsequent response variables of the JetFitterCombNN algorithm.

the muon trajectory is very close to the jet axis and the b fraction cannot be determined because the flavour template shapes are too similar. For many new physics searches, as well as Standard Model measurements, the b tagging efficiency for jets with high p_T must be well understood. For these analyses the b tagging efficiency can be estimated from Monte Carlo simulation, and a set of systematics that take into account all the effects which could result in the efficiency in data being significantly different to that in Monte Carlo simulation can be used in the calibration of a given tagging algorithm. This is discussed in Chapter 6.

More details on the p_T^{rel} method can be found in [71]. Other methods for estimating the b tagging efficiency in data are described in [72], [73] and [74].

Chapter 5

Detector Commissioning: Resolution Studies

5.1 Introduction

The accurate tracking of charged particles through the inner detector is an essential ingredient in all physics analyses in ATLAS. Reconstructing the paths of charged particles as they propagate from the primary vertex allows precise measurement of particle properties such as charge and momentum.

The resolution of a particle track not only depends on the intrinsic detector resolution of the silicon modules but also on their alignment. If the assumed position of a module in the detector is significantly different from its actual position, the track resolution is downgraded, as shown in Figure 21. Thus an important part of detector commissioning is module alignment. The amount of material in the inner detector also affects track resolution. Particles interact with detector material and service structures resulting in multiple scattering. The material budget must therefore be well modelled in simulation to fully quantify the track resolution.

5.2 Impact parameters and resolutions

The transverse and longitudinal impact parameters, d_0 and z_0, are used extensively in b tagging algorithms to identify jets containing b hadrons (see Section 4.7). The impact parameter resolution is thus critical to analyses requiring the identification of b jets, such as the $Z + b$ jets cross-section measurement presented in Chapter 7.

The resolution of the impact parameter of a track, $\sigma(d_0^{\text{track}})$, can be divided into two independent terms, one accounting for the intrinsic detector resolution and misalignment, $\sigma_{\text{intrinsic}}$, and one describing the multiple scattering of particles in detector material, σ_{MS}:

$$\sigma(d_0^{\text{track}}) = \sigma_{\text{intrinsic}} \oplus \sigma_{\text{MS}} \tag{23}$$

The multiple scattering term itself is dependent on two properties of the particle track: its momentum, p, and angle in the yz-plane, θ [77, 78]. A particle with low momentum is more likely to interact with matter and multiple scatter. Particles with lower values of θ, that are closer to the beampipe, will pass through more detector material. The impact parameter uncertainty due to multiple scattering is therefore

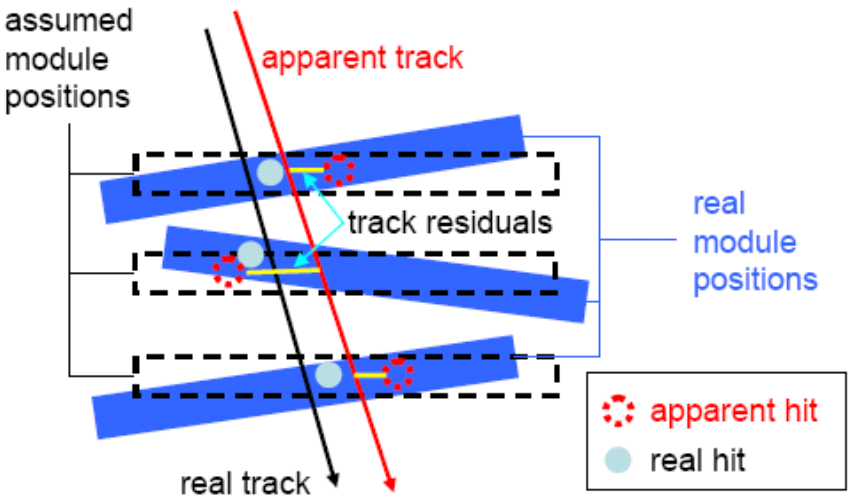

Figure 21: Result of module misalignment [75].

inversely proportional to transverse momentum p_T and $\sin\theta$. Assuming cylindrical geometry for the inner detector barrel:

$$\sigma_{\mathrm{MS}} = \frac{b}{\sqrt{p^2 \sin^3\theta}} = \frac{b}{\sqrt{p_{\mathrm{T}}^2 \sin\theta}}, \tag{24}$$

where b is a constant describing the material budget. The impact parameter resolution derived from the track properties is then given by:

$$\sigma^2(d_0^{\mathrm{track}}) = \sigma^2_{\mathrm{intrinsic}} + \frac{b^2}{p_{\mathrm{T}}^2 \sin\theta}\,. \tag{25}$$

The total error in the impact parameter will also depend on the resolution of the primary vertex, σ_{PV}:

$$\sigma(d_0) = \sigma(d_0^{\mathrm{track}}) \oplus \sigma_{\mathrm{PV}} \tag{26}$$

The width of a Gaussian fit to the impact parameter distribution represents $\sigma(d_0)$. Plotting $\sigma^2(d_0)$ in bins of $1/p^2 \sin^3\theta$ and fitting the data with a straight line will produce a y-intercept that corresponds to the alignment, described by $\sigma_{intrinsic}$, and a gradient that describes the amount of multiple scattering from the detector material. This was performed with data from proton collisions at $\sqrt{s}$ = 900 GeV and 7 TeV.

5.3 Data from p-p collisions at $\sqrt{s} = 900$ GeV

5.3.1 Selection

To study the aligment and material budget of the inner detector for the commisioning of ATLAS, distributions of the impact parameter resolution were produced using data from proton-proton collisions at $\sqrt{s} =$ 900 GeV. Data is recorded from the minimum bias trigger stream, providing around 450,000 events, with an event selection applied to eliminate data recorded from runs or luminosity blocks when the detector was not fully configured or when subdetectors were not functioning. A modified version of the baseline track selection for b tagging was used [76]. This selection is designed to provide well defined tracks whilst rejecting tracks from particles with a long lifetime, fake tracks, and tracks deflected by material interactions. It is required that there is a minimum of seven hits in the silicon detectors, with at least two hits in the pixel layer, one of which must be in the b layer. The transverse momentum cut was relaxed from 1 to 0.5 GeV to increase the sample size for a more accurate determination of the alignment. The impact parameter cuts, $|d_0| < 1$ mm and $|z_0 \sin\theta| < 1.5$ mm, were not applied as the full range of values for the impact parameter distributions are required so that Gaussian functions can be fitted to data. Also, the eta cut, $|\eta| < 1.2$, was relaxed to $|\eta| < 2.5$ to study a larger detector acceptance. Table 6 summarizes the selection cuts.

Cut Parameter	Cut Value
p_T	> 0.5 GeV/c
$\|\eta\|$	< 2.5
Silicon hits	> 6
Pixel hits	> 1
b layer hits	> 0
Tracks in PV	> 3

Table 6: Track selection criteria for producing impact parameter distrubutions.

A cut on the minimum number of tracks used in reconstructing the primary vertex ensures that it is high quality. This reduces the error in the primary vertex position, which has a notable effect on impact parameter resolution. The track under consideration is removed from the primary vertex reconstruction

when calculating its impact parameter so that it is unbiased. Including the track in the fit would pull the primary vertex towards it, producing a smaller impact parameter and a narrower, biased impact parameter distribution, so for each track the primary vertex is recalculated with the track of interest removed.

5.3.2 Impact parameter resolution

The distribution of the transverse impact parameter for all tracks passing the selection cuts from collisions at $\sqrt{s}$ = 900 GeV are shown in Figure 22. The simulation shows excellent agreement with data, and the shape of the central region of the data distribution can be accurately fitted with a Gaussian function, as can be seen in Figure 23.

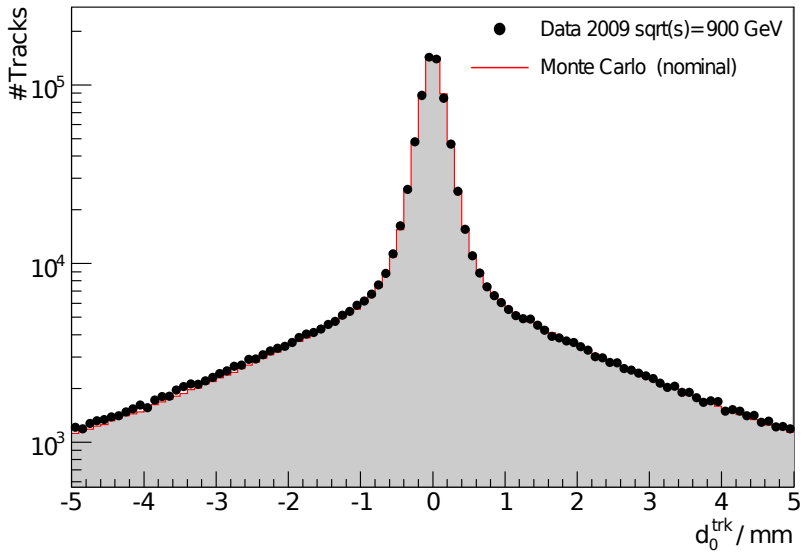

Figure 22: Distribution of the transverse impact parameter d_0, for all tracks passing the selection cuts described above, produced from collisions at $\sqrt{s}$ = 900 GeV.

To study the effect of module alignment and material description on the overall resolution of tracks in the inner detector, d_0 distributions are analysed in bins of $1/p^2 \sin^3\theta$. The quantity $\sigma^2_{d_0}$ for each bin is determined by fitting a Gaussian function to the d_0 distribution in that bin. This quantity contains the primary vertex resolution convoluted with the track impact parameter resolution. The Gaussian is fitted iteratively over a range of $\pm 2\,\sigma^2_{d_0}$, centered on the histogram mean. This prevents the non-Gaussian tails of the distribution significantly affecting the fit, which are mainly a result of material interactions and misalignment. Figure 23 shows an example d_0 distribution for $0.2500 < 1/p^2 \sin^3\theta < 0.3025$ GeV^{-2}

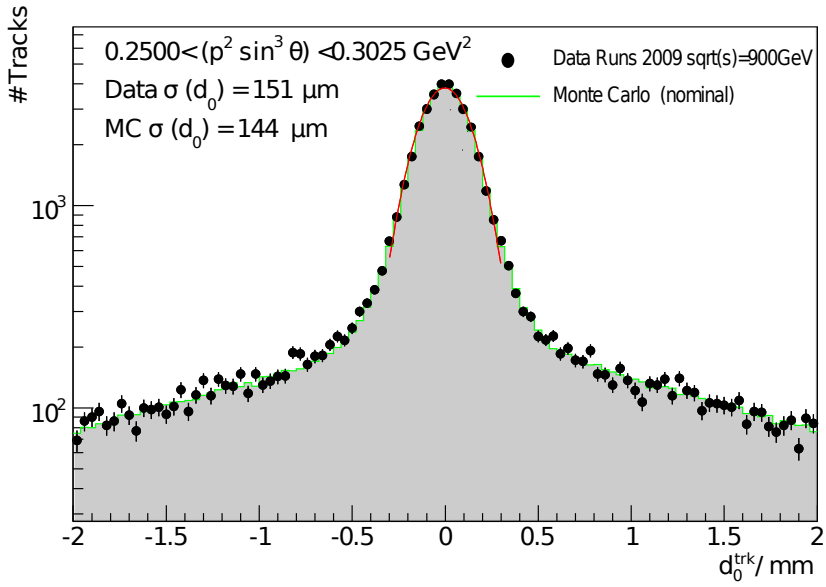

Figure 23: Distribution of the transverse impact parameter, d_0, for tracks with $0.25 < 1/p^2 \sin^3\theta < 0.3025$ GeV^{-2}, fitted with a Gaussian.

fitted with a Gaussian. The Monte Carlo simulation agrees fairly well with the data, however, the impact parameter distribution in Monte Carlo is narrower than that in data. This is discussed in Section 6.4.1.

Figure 24 shows the extracted impact parameter resolution determined from the Gaussian fits as a function of $1/p^2 \sin^3\theta$ for data, nominal Monte Carlo, and two other Monte Carlo simulations that are modelled with the amount of material in the inner detector increased by +10 % and +20 %. For this comparison the η range is restricted to the barrel region with $|\eta| < 1.2$ where there is cylindrical symmetry. The gradient of the straight-line fit for these additional simulations is significantly greater than that in data, and the nominal simulation agrees best with experimental data confirming that the material budget is well described by the default simulation.

Figure 25 shows the data and nominal Monte Carlo, and also simulated data generated with 'day 1' alignment, which represents an initial estimate of the module positions. Improving the accuracy of module position and alignment results in higher impact parameter resolution. This reduces the gradient of the straight line fit to the d_0 variance. This can be seen in Figure 25, which shows that the initial alignment of the detector is better than the day 1 estimate, and first data measurements agree quite well with improved alignment in the nominal Monte Carlo simulation.

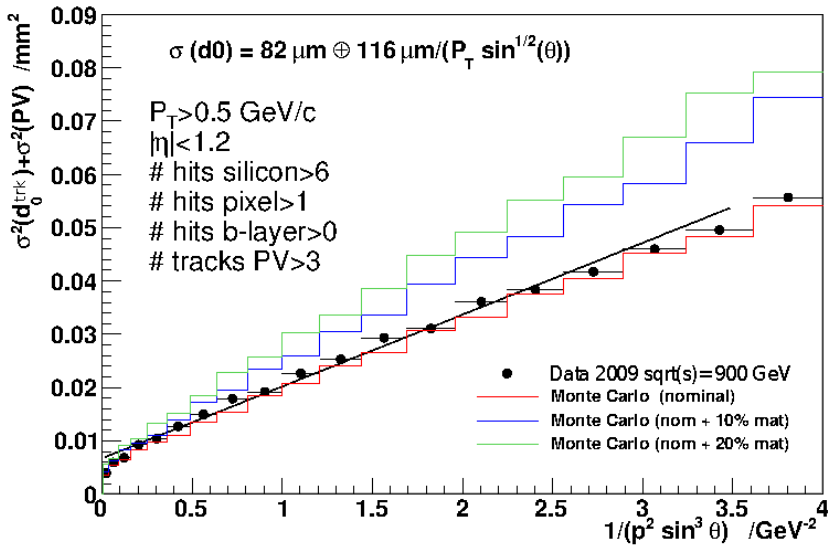

Figure 24: Distribution of d_0 variance as a function of $1/p^2 \sin^3\theta$ for tracks with $|\eta| < 1.2$ produced from collisions at $\sqrt{s}$ = 900 GeV. Nominal Monte Carlo is displayed along with two other MC simulations show the effect of increased material budget in the inner detector.

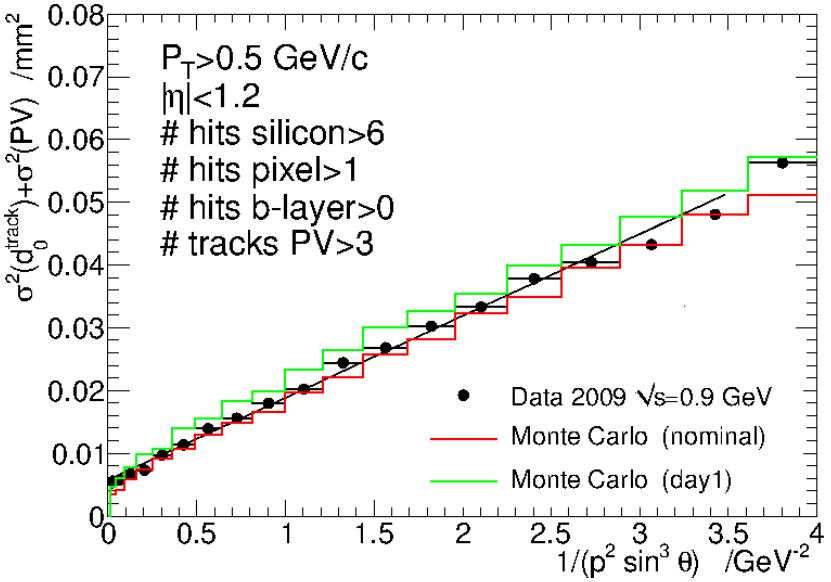

Figure 25: Distribution of d_0 variance as a function of $1/p^2 \sin^3\theta$ of tracks produced from collisions at $\sqrt{s}$ = 900 GeV. Nominal Monte Carlo is displayed along with another MC simulation corresponding to estimated 'day 1' alignment of the inner detector.

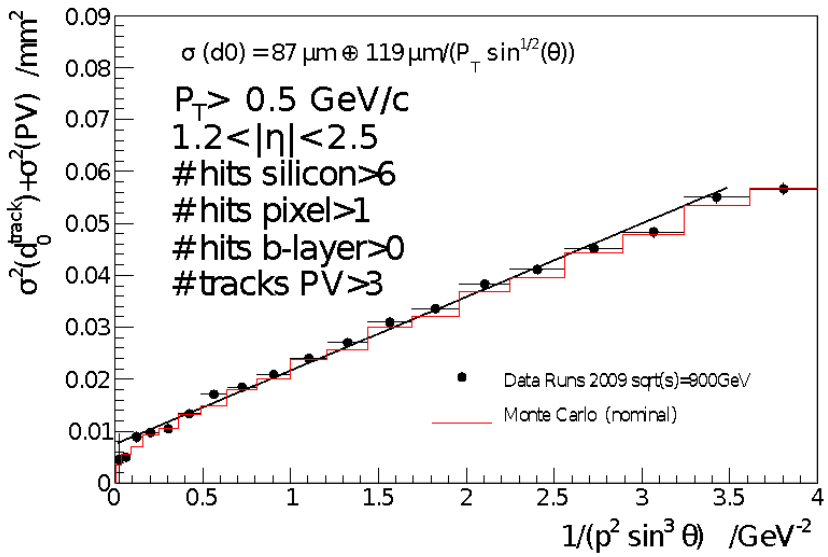

Figure 26: Distribution of d_0 variance as a function of $1/p^2 \sin^3\theta$ of tracks produced from collisions at $\sqrt{s}$ = 900 GeV, for the forward region of the inner detector, $1.2 < |\eta| < 2.5$, for data and nominal Monte Carlo. The resolution is slightly worse than in the central region, as expected.

Separate histograms were produced for the central region, $|\eta| < 1.2$, and the forward region, corresponding to the endcaps, with $1.2 < |\eta| < 2.5$. The parametrization of the impact parameter resolution, defined in Equation 25, assumes that the detector material is cylindrically symmetric. This is only true for the central region, and is not technically valid for the endcaps. However, the resolution histogram for the forward region in Figure 26 shows that this model seems to work well for the endcaps. The gradient and intercept of the straight-line fits to these distributions in nominal Monte Carlo simulation agree well with those in data. These parameters describe the material budget and the alignment and intrinsic resolution respectively. This confirms that the description of the inner detector material, impact parameter resolution, and alignment is well modelled in simulation at a collision energy of 900 GeV.

5.4 Data from p-p collisions at $\sqrt{s}$ = 7 TeV

5.4.1 Selection

A similar event selection was used on 15 nb^{-1} of data from collisions at $\sqrt{s}$ = 7 TeV. At higher energies, a tighter track selection needs to be performed to reduce combinatorial tracks resulting from higher track multiplicities. The minimum number of tracks in the primary vertex reconstruction was increased to

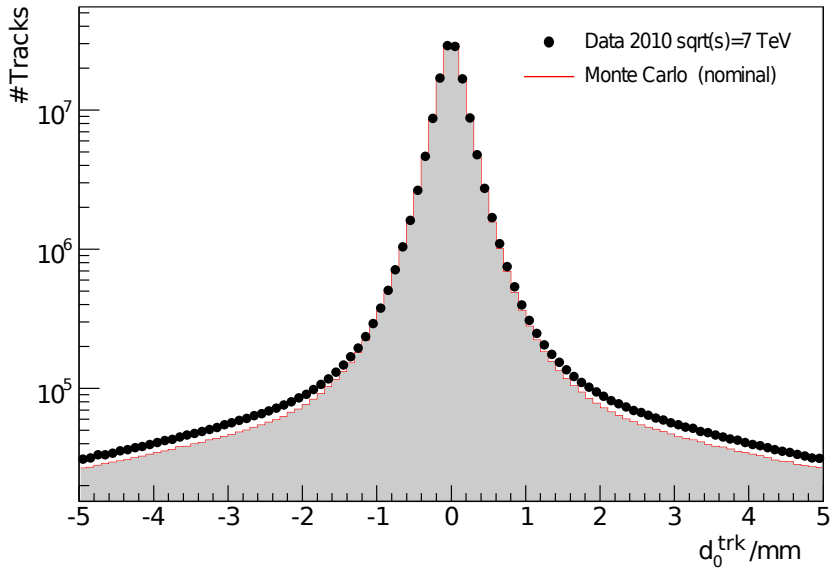

Figure 27: Distribution of the transverse impact parameter d_0*, for tracks passing the selection cuts, produced from collisions at* $\sqrt{s}$ *= 7 TeV.*

10. This improves the resolution of the primary vertex and hence improves the overall impact parameter resolution. The number of vertices in the event was also restricted to 1. This cut is performed to eliminate events with pile-up vertices produced from QCD interations that are not part of the hard scatter process, as these interactions were not well understood in first data. The overall track resolution is improved by the increased statistics.

5.4.2 Impact parameter resolution

Figure 27 shows the transverse impact parameter distribution for tracks passing the selection cuts at $\sqrt{s}$ = 7 TeV. The simulated data describes the transverse impact parameter very well in the central region, where the Gaussian fit is performed to measure the resolution. However, the tails of the distribution are narrower in Monte Carlo than in data. This needs to be corrected for, and the effect of this on the identification of heavy-flavour jets is discussed in Chapter 6.

To study the resolution of the inner detector for tracks produced from collisions at $\sqrt{s}$ = 7 TeV, d_0 variance distributions were produced for the new data and updated Monte Carlo simulation with the same method used for data at 900 GeV in Section 5.3. With a much larger number of tracks in the selected data sample, the number of bins of $1/p^2 \sin^3\theta$ can be increased. At $\sqrt{s}$ = 7 TeV, there is better agreement

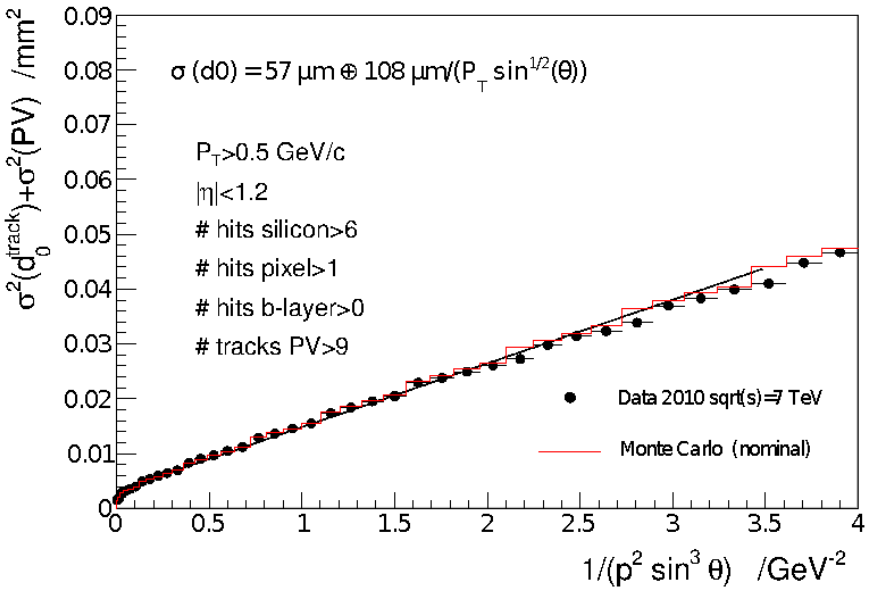

Figure 28: Distribution of d_0 variance as a function of $1/p^2 \sin^3\theta$ for tracks produced from collisions at $\sqrt{s}$ = 7 TeV for data and nominal Monte Carlo.

between data and simulation in the resolution histograms. The overall impact parameter resolution is greatly improved, as can be seen by comparing Figures 24 and 28, where it has been reduced from 82 μm to 57 μm. The d_0 resolution in the forward region, shown in Figure 29, also has good agreement between data and simulation.

Distributions of d_0 were also produced in bins of η to investigate how the impact parameter resolution and material budget vary over the detector acceptance. This allows a direct comparison of the intercept value, p_0, corresponding to $\sigma^2_{\text{intrinsic}}$, and gradient, p_1, represented by b^2 in Equation 25, of the linear fit in data and simulation to see how well the simulation agrees for different regions of the inner detector. The histograms of p_0 and p_1 are shown in Figure 30. As expected, as $|\eta|$ increases, the impact parameter resolution gets worse, due to the increased material traversed by the particle. Overall, there is a good agreement between data and simulation, except for one discrepancy in p_0, for the bin corresponding to -2.2 < η < -2.5, where the data has worse resolution than simulation. This is attributed to a misalignment in the endcap, as there was a known problem with one of the endcaps in this dataset.

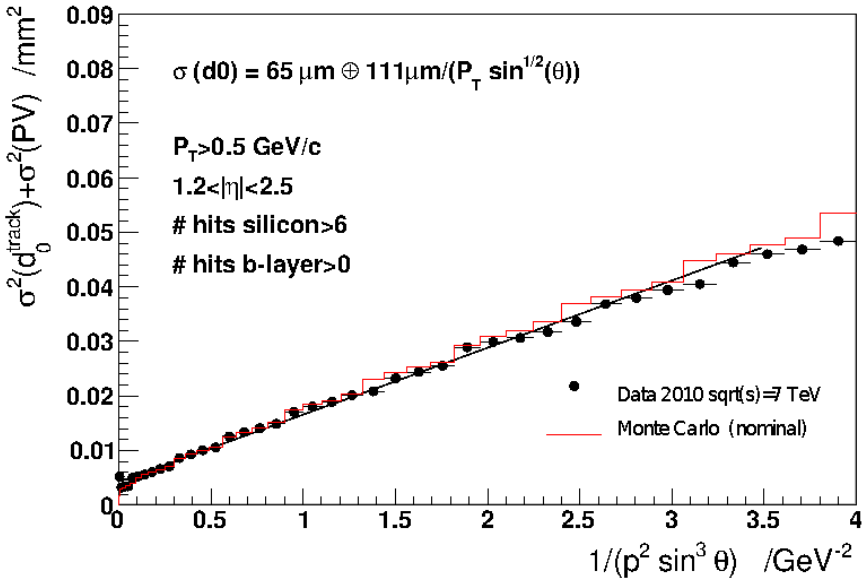

Figure 29: Distribution of d_0 variance as a function of $1/p^2 \sin^3\theta$ for tracks produced from collisions at $\sqrt{s} = 7$ TeV, for data and nominal Monte Carlo, in the forward region of the inner detector $1.2 < |\eta| < 2.5$.

5.5 Summary

Early data recorded by the ATLAS detector of proton collisions at energies of $\sqrt{s} = 900$ GeV and $\sqrt{s} = 7$ TeV was used to study the distributions of the transverse impact parameter. These distributions were used to investigate the resolution and material budget of the inner detector. This study has shown that in the early stages of data taking, the modelling of the ATLAS inner detector in simulation is very good. Tracks in the inner detector and their resolution are well measured and described by Monte Carlo simulation, and this allows the *b* tagging analysis to proceed by measuring and calibrating the behaviour of heavy flavour jets within ATLAS at $\sqrt{s} = 7$ TeV. This involves studying jet properties such as momentum, multiplicity, track multiplicity, energy scales, and jet spatial distributions in ATLAS. The analysis of the output distributions of the various tagging algorithms and neural network outputs, and their tagging efficiencies and systematics, is essential for physics analyses involving heavy flavour jets.

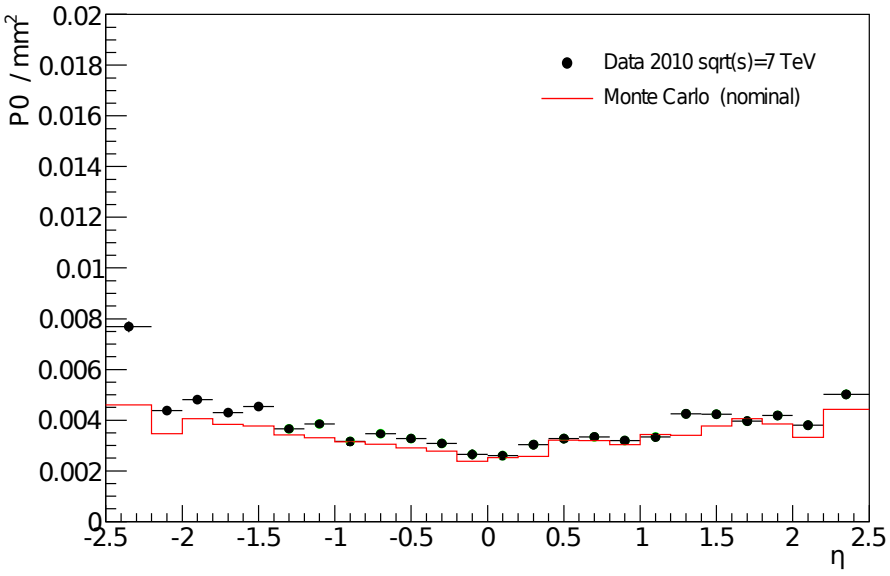

(a)

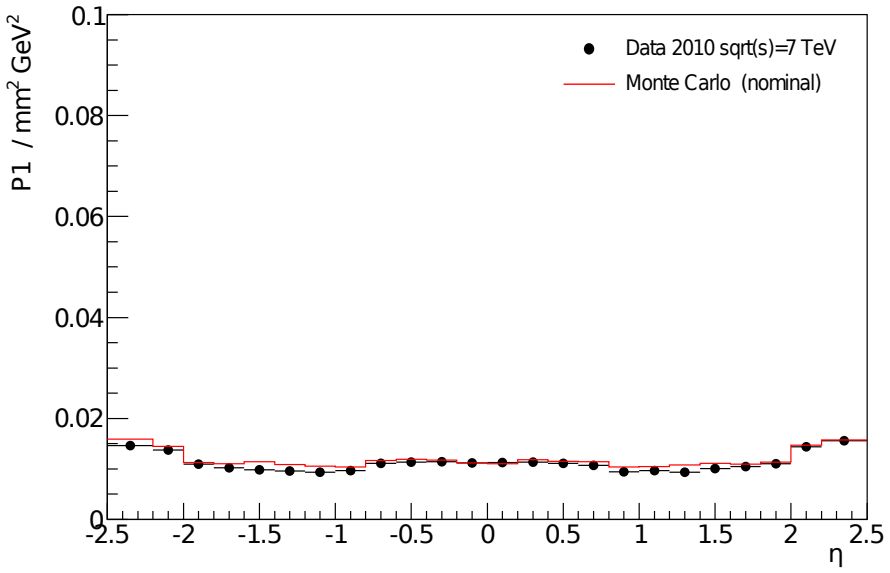

(b)

Figure 30: (a) Intrinsic resolution and misalignment factor p_0 *as a function of η, corresponding to* $\sigma^2_{\text{intrinsic}}$ *in Equation 25. The discrepancy for -2.2 < η < -2.5 may be due to a misaligned endcap. (b) The amount of material traversed by a particle track is quantified by the factor* p_1*, proportional to the factor* b^2 *in Equation 25, shown here as a function of η.*

Chapter 6

Identifying Heavy Flavour Jets: *b* tagging Calibration

6.1 Introduction

To estimate the number of jets originating from the decay of bottom quarks in collision events, the efficiency of the *b* tagging algorithms (defined in Section 4.7) used to identify *b* jets must be determined. In most analyses, the efficiency is derived from Monte Carlo simulation using the parton truth information from the event generator, however, the efficiencies in data and simulation will generally be different for a number of reasons, such as detector and reconstruction effects. The *b* tagging algorithms must therefore be calibrated for use in physics analyses to correct for differences between data and simulation, so that the true number of *b* jets in data can be estimated using the efficiencies from Monte Carlo. This is usually done by applying a jet p_T dependent efficiency scale factor to Monte Carlo efficiencies that correct the *b* tagging performance in simulation to that observed in data.

Methods for estimating the *b* tagging efficiency from data to calibrate the *b* tagging algorithms are generally limited and do not provide calibration for high-p_T jets. At the time of this study, data-driven methods were limited to jet $p_T < 140$ GeV [71]. For jets with $p_T > 140$ GeV, the scale factor from the highest jet p_T bin is applied, with the systematic uncertainty doubled. This approach is not technically correct since the efficiency in data for this p_T range is not measured. In this chapter, an alternative to this method is described, where the *b* tagging efficiency in data for each jet-p_T bin is taken to be the same as that in simulation (giving a data/MC scale factor of unity), and the error on the efficiency is defined with a set of jet-p_T dependent systematic uncertainties that take into account effects where there are significant discrepancies between data and simulation that affect the *b* tagging efficiency. This method can be applied to any given *b* tagging algorithm and is valid over the full jet p_T range. This study measures efficiencies and systematic effects for the SV0 *b* tagging algorithm, described in Section 4.7.1.

It is also important to know the probability of tagging jets originating from the decay of a charm quark or a light flavour quark (u, d, s quark or gluon) as coming from a *b* decay, referred to as the *c* tagging and mistag efficiency respectively, as these values significantly affect the estimation of the number of *b* jets in data. Data/MC scale factors are also provided for these efficiencies in the calibration

of the b tagging algorithms. In the same way, these efficiencies can also be calibrated by providing a set of jet p_T dependent systematics . At the time of this study, there was no explicit measurement of the c tagging efficiency, and the data/MC scale factors for the c tag efficiency were assumed to be the same as those for the b tag efficiency. This was verified by studying the same set of systematic effects on the c tagging efficiency.

6.2 Samples and event selection

6.2.1 Data and Monte Carlo samples

The sample used in this study consists of data periods B2 to F (runs 178044 to 182519) recorded by the ATLAS detector in 2011 from proton-proton collisions at $\sqrt{s} = 7$ TeV delivered by the LHC. The data quality selection established by the top working group is applied to the sample, ensuring only data collected during stable beam periods and when all detector sub-systems were fully operational is used. The total integrated luminosity for this data sample is 330 pb^{-1}, corresponding to around 93 million events. Throughout this period, the LHC beam parameters were stable. In particular, the luminosity-weighted average of the Poisson distribution on the number of interactions per beam-crossing, μ, which represents the amount of pileup, was consistently around six.

The simulated data used in this analysis comprises of QCD dijet Monte Carlo samples generated with the PYTHIA 6.4.21 [80] program using the MRST leading order parton distribution functions (for details, see [81, 82]). These consist of around 40 million events, which are simulated in 8 samples (J0-J7) based on the transverse momentum of the hard scatter process. These events are then passed through the GEANT4 simulation of the ATLAS detector and reconstructed with the same release of the ATLAS software as data. The eight MC samples were combined taking into account their production cross section as shown in Table 7.

The beamspot position in these samples has been simulated to reproduce period D of the 2010 data. Most disabled pixel modules and faulty readout chips are masked in simulation as they are in data. There may be small run-to-run variations of the number of disabled channels in data that are not corrected for in the simulation, but this is a small effect. The detector simulation is perfectly aligned, leading to discrepancies between data and simulation, as seen in Section 5.3.2.

Sample	p_T range (GeV)	Cross-section (pb)	Simulated events
J0	8-17	9860800	16.4M
J1	17-35	678180	7.4M
J2	35-70	40982	2.8M
J3	70-140	2196.9	2.8M
J4	140-280	87.701	2.8M
J5	280-560	2.3501	2.8M
J6	560-1120	0.033614	2.1M
J7	1120-2240	0.00013744	1.4M

Table 7: Monte Carlo samples used in this study, showing p_T range, cross section and number of events.

6.3 Trigger, selections, and corrections

6.3.1 Trigger

The data events used for this study contain a jet that fired one of the L1 jet triggers and were recorded by the JetTauEtmiss stream. Events are required to pass one of a variety of EF triggers with increasing thresholds, requiring $p_T > \{10, 15, 20, 30, 40, 55, 75, 100, 135, 180, 240\}$ GeV. The low p_T triggers are prescaled by up to five orders of magnitude. This is not modelled in simulation, so the jet transverse momentum spectra from Monte Carlo must be reweighted to that in data. This reweighting is described in Section 6.3.3.

6.3.2 Selection

Events are required to have at least 10 tracks associated to the primary vertex, and must contain no other vertex with more than 4 tracks. This serves to reject events with pileup vertices. The track and jet selection is outlined in Table 8. Jets measured in problematic calorimeter regions, or likely caused by detector effects such as energy spikes in the calorimeter, and those arising from beam background are removed by applying various 'jet cleaning' cuts. These cut on jet properties such as the timing of energy deposits and the fraction of jet energy measured in the hadronic and EM calorimeters. Jet cleaning is described further in [83].

Track Cuts	Jet Cuts
$p_T > 0.5$ GeV/c	$p_T > 25$ GeV/c
$\|\eta\| < 2.5$	$\|\eta\| < 2.5$
Silicon hits > 6	Electron overlap $\Delta R > 0.4$
Pixel hits > 1	Number of jets > 1
b layer hits > 0	
Tracks in PV > 9	

Table 8: Track and jet selection cuts

6.3.3 Corrections

The simulation is produced without knowledge of certain features in data, such as the proton beam parameters, which can affect the modelling. This requires that a number of corrections be applied to simulation, performed by reweighting certain distributions in simulation to match those in data. Collisions from protons in neighbouring bunches give rise to out-of-time pileup. To correct for this, the simulated events are reweighted to reproduce the μ distributions in data. The distribution of the number of vertices is shown in Figure 31. The number of vertices is still underestimated by simulation, and this discrepancy shall be addressed in future versions of the reconstruction software and Monte Carlo simulation.

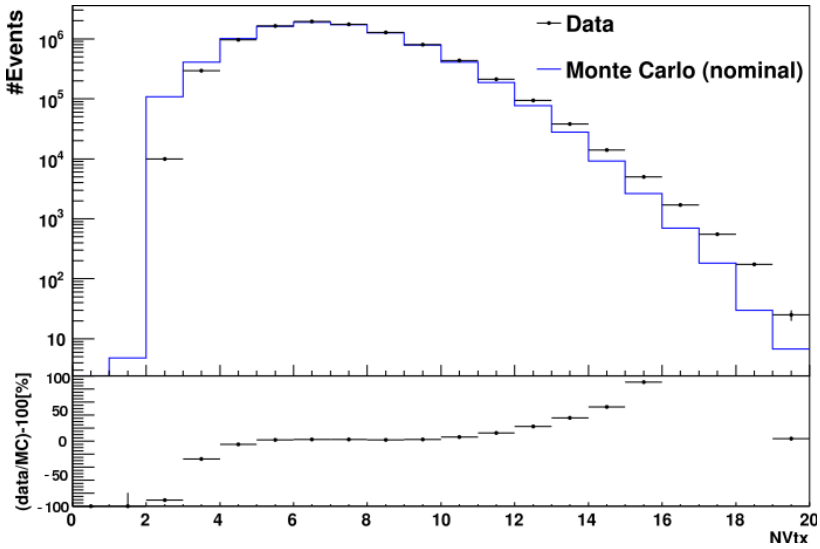

Figure 31: Distribution of the number of vertices in the event for data and default Monte Carlo (no systematic effect applied) with data/MC ratio.

The combination of jet triggers used for this study are prescaled, leading to significant differences between data and simulation. In particular, the p_T and η distributions for jets do not agree. It is therefore neccessary to perform a two-dimensional reweighting in jet p_T and η. Since the most energetic jet is most likely to have fired the trigger, a two-dimensional reweighting map of the leading jet p_T and η is created and used to correct the simulation to match the data. The reweighted jet p_T and η distributions are shown in Figure 32, where the reweighted simulation describes the data well. The features in the jet p_T spectrum are caused by trigger efficiency turn-on curves resulting from the trigger prescaling.

6.4 Calibrating efficiencies using Monte Carlo

In order to use tagging efficiencies that are calculated from Monte Carlo simulation, as described in Section 4.7.4, for analyses on real data, a range of effects need to be measured. These are mainly effects that cause significant discrepancies between data and simulation, together with detector effects and uncertainties on important quantities in the event. In this section, the effects studied are described, and the percentage by which the b tagging efficiency, ϵ_b, varies is given.

6.4.1 Impact parameter resolution

An important quantity when selecting b jets from a sample is the distance of closest approach of the trajectory of a track to the primary vertex. For tracks produced from the decay of short lived particles such as the electroweak W and Z bosons, the impact parameter will be very close to zero. However, for tracks produced from the decay of long lived particles such as b hadrons, K^0_s, and Λ^0, the impact parameter will be significantly different from zero. This property of tracks is used directly in impact parameter based taggers. Distributions of the transverse and longitudinal impact parameters d_0 and z_0 in data and simulation are shown in Figure 33. There is an asymmetry between the shape of the distribution for positive and negative values of the impact parameter. There are more tracks with a positive impact parameter, since the impact parameter is signed with respect to the jet axis, as described in Section 4.7.1. The impact parameter sign is given by the projection of the track vector onto the jet axis. The asymmetry is mainly due to heavy flavour contributions, with smaller contributions from K^0s and Λ^0 decays and photon conversions. Tracks produced from such phenomena will generally have a positive impact parameter, although the impact parameter sign can sometimes be negative due to reconstruction and resolution effects.

In Monte Carlo simulation the detector is modelled with perfect alignment. This results in the impact

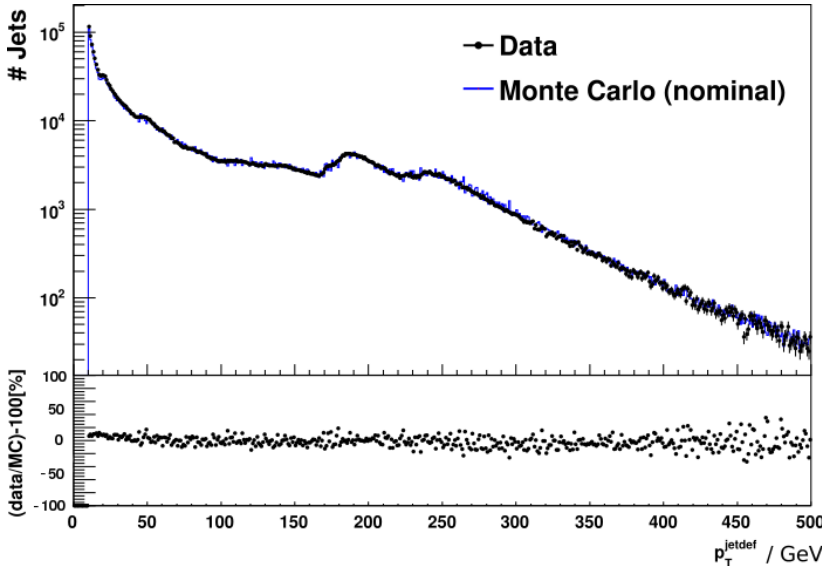

(a)

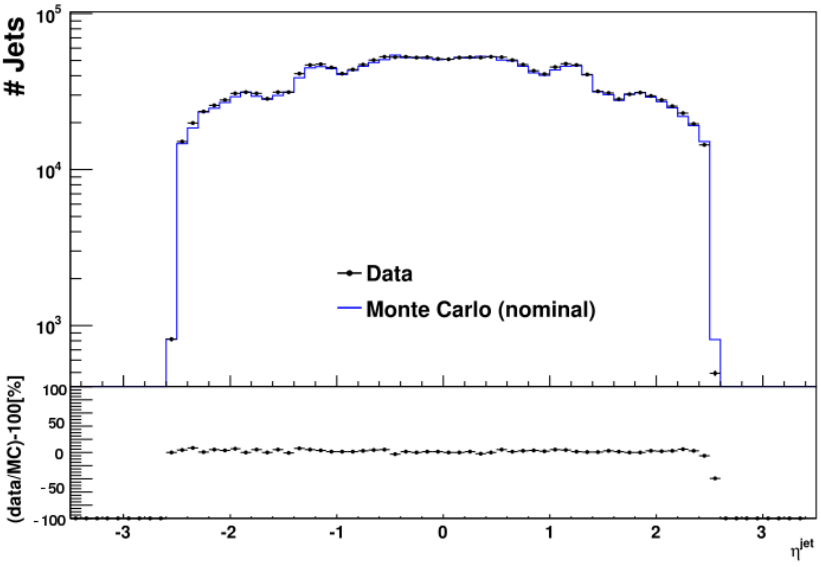

(b)

Figure 32: (a) Jet p_T and (b) η distributions for all jets passing cuts after reweighting in data and default Monte Carlo, with the data/MC ratio distribution shown underneath.

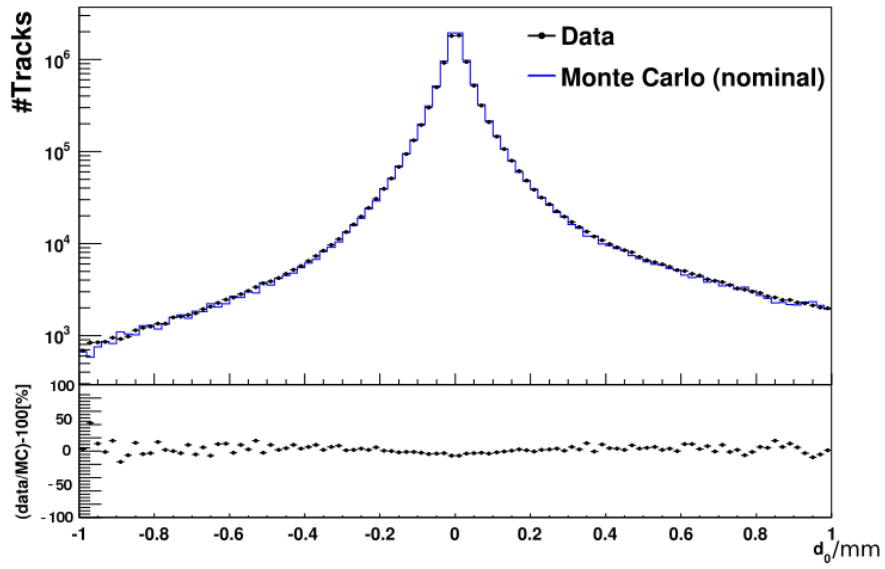

(a)

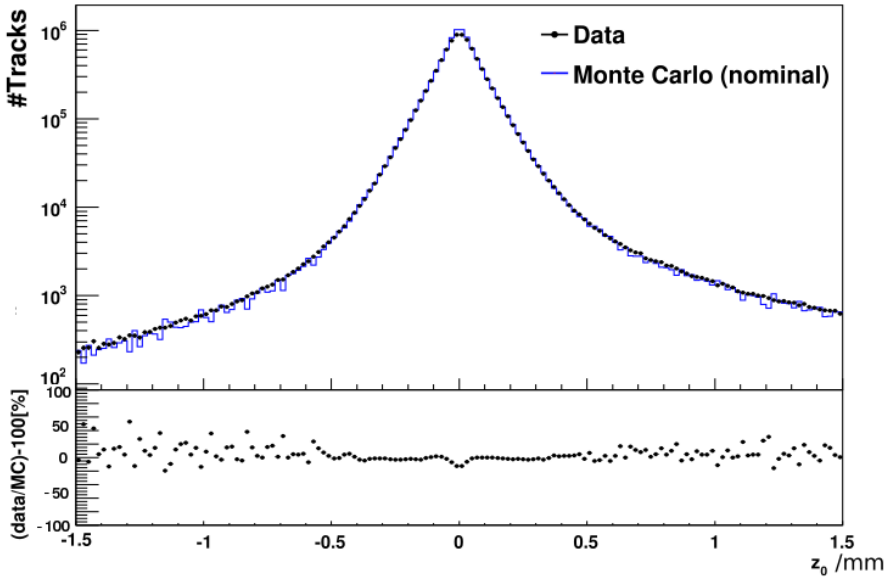

(b)

Figure 33: Distribution of (a) d_0 and (b) z_0 in data (circles) and simulation (histogram). The impact parameter resolution is narrower in Monte Carlo than in data. The asymmetry induced by heavy flavour contributions (and also, to a smaller extent, K^0s, Λ^0s, photon conversions, etc.) is clearly visible on both distributions.

parameter distributions in simulation being narrower than those in data, since the position of detector modules can only be known to finite accuracy. This uncertainty must be taken into account when using efficiencies derived from Monte Carlo in analyses on real data. This is performed by smearing the Monte Carlo impact parameter distributions, and propagating this effect through the analysis chain by re-running the b tagging algorithm, and measuring how much this smearing changes the tagging efficiencies. A systematic contribution is then calculated by taking the difference between the default Monte Carlo and smeared Monte Carlo efficiencies.

The smearing is applied by convolving the transverse IP distribution with a Gaussian of 10 μm width for the central region, $|\eta| < 1.2$, and 25 μm width in the forward region, $1.2 < |\eta| < 2.5$. These numbers were obtained from studies of tracks specifically for b tagging algorithms in 7 TeV data [85]. Since discrepancies between data and simulation are also seen in the tails of the IP distribution, a wider Gaussian of width 100 μm is added to 8 % of tracks. These values for long-range smearing were chosen as they produced a reasonable agreement in the tails, as can be seen in Figure 33. For the longitudinal impact parameter, z_0, a similar procedure is used, adding just one Gaussian of width 15 μm. The tranverse and longitudinal impact parameter distributions for data and smeared Monte Carlo are shown in Figure 34. The simulation is oversmeared to produce a wider impact parameter distribution than in data, to make a conservative estimate of this systematic uncertainty on the b tagging efficiency, hence the worse agreement between data and simulation compared to Figure 33. The anomalous spikes in two bins in the tails of Figure 34(a) are artefacts from the smearing procedure. Smearing d_0 and z_0 shifts the b tagging efficiency relative to the default efficiency by -0.9 % and +1.6 % respectively over the full p_T range.

6.4.2 Tracking efficiency

Some tracks will not be reconstructed in the detector for a number of reasons. An example is when a charged particle does not deposit enough energy in a silicon sensor to generate a signal above threshold and a hit is not registered. This means that occasionally a particle may not be reconstructed in the event. This effect is not modelled accurately in simulation, and so must be considered when using tagging efficiencies from Monte Carlo. To estimate the size of this effect, a percentage of tracks, selected at random, are removed from simulated events. This is performed in bins of η, since different regions of the inner detector have different tracking efficiencies. The tracking inefficiencies were obtained from mesurements of low energy minimum bias events [87]. The jet track multiplicites for data, default simulation, and modified simulation are shown in Figure 35. There is a small reduction in the jet track

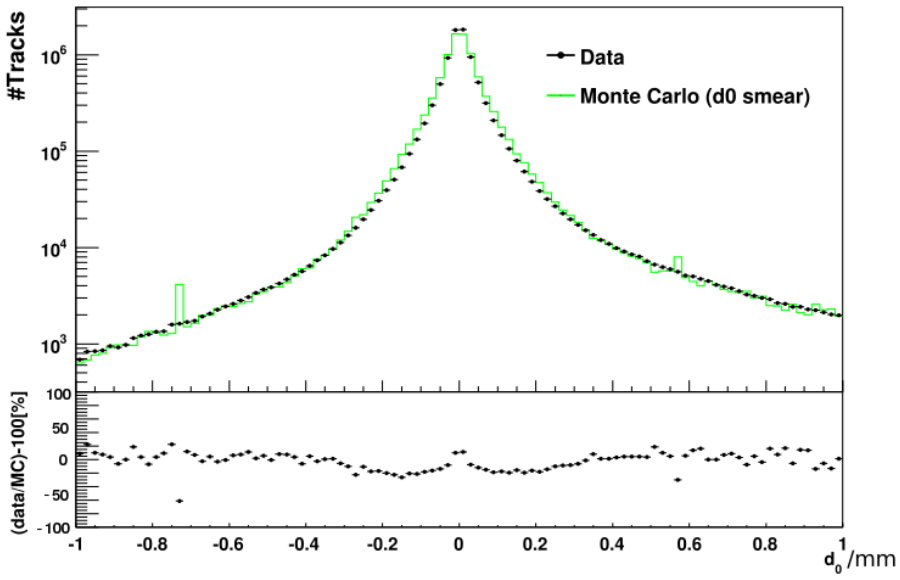

(a)

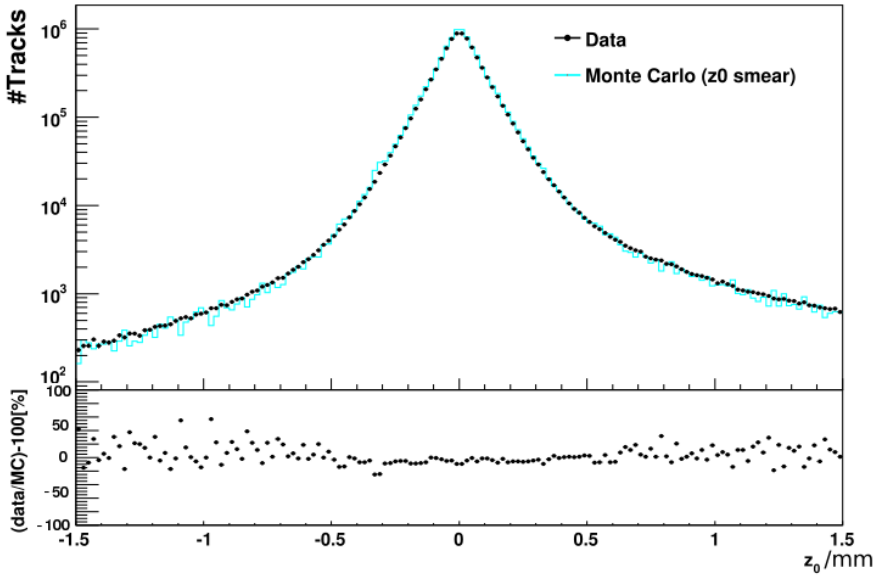

(b)

Figure 34: Distribution of (a) transverse impact parameter d_0 and (b) longitudinal impact parameter z_0 in data (circles) and simulation (histogram) after applying the smearing procedure. The asymmetry induced by heavy flavour contributions (and also, to a smaller extent, K^0s, Λ^0s, photon conversions, etc.) is clearly visible on both distributions.

multiplicity, and the modified simulation better describes the data. The b tagging efficiency over the full p_T range was reduced by 0.9 % relative to the default efficiency when applying this effect.

6.4.3 Tracks with shared hits

The energies at which protons are collided at the LHC produce very high track multiplicities and track densities in the ATLAS detector. Occasionally, more than one charged particle will deposit energy in a single detector channel. This results in some tracks having shared hits with other tracks. The ATLAS b tagging group defines a track with shared hits as having at least one shared hit in the pixel detector or at least two shared hits in the SCT detector. Shared hits are more common in the silicon strip detectors than the pixel detectors, since they only provide precision measurement in R-ϕ, and only loosely constrain the direction orthogonol to R-ϕ. However, shared hits in the pixel detectors are more critical for b tagging since the pixel hits, particularly in the b layer, significantly constrain the track impact parameter. Although only a small fraction of tracks have shared hits, these tracks induce large tails in the transverse impact parameter distribution, as seen in Figure 36, and this significantly degrades the b tagging performance. To study the extent of this effect, 50 % of tracks with shared hits, selected at random, are removed from each event. The b tagging is then re-run and efficiencies calculated. Applying this effect shifted the b tagging efficiency by -2.9 % over the full p_T range. This is a large effect, however, it should be noted that throwing away 50 % of tracks is conservative.

6.4.4 Fake tracks

With large track multiplicities and a high density of hits in the silicon detectors, it is not uncommon for fake tracks to be reconstructed in the inner detector. This happens when silicon hits from a number of real particles are reconstruced as a single fake track. The main cause of this effect is simply the combinatorics of large hit densities in the inner detector. However, there are other effects that can contribute to this, such as material interactions and dead sensors that produce incomplete track information. The number of fake tracks is uncertain and will affect the b tagging. The size of this effect is estimated by throwing away 50 % of fake tracks in simulation, selected at random, and re-running the b tagging. This produced a shift in the b tagging efficiency of +0.9 % over the full p_T range.

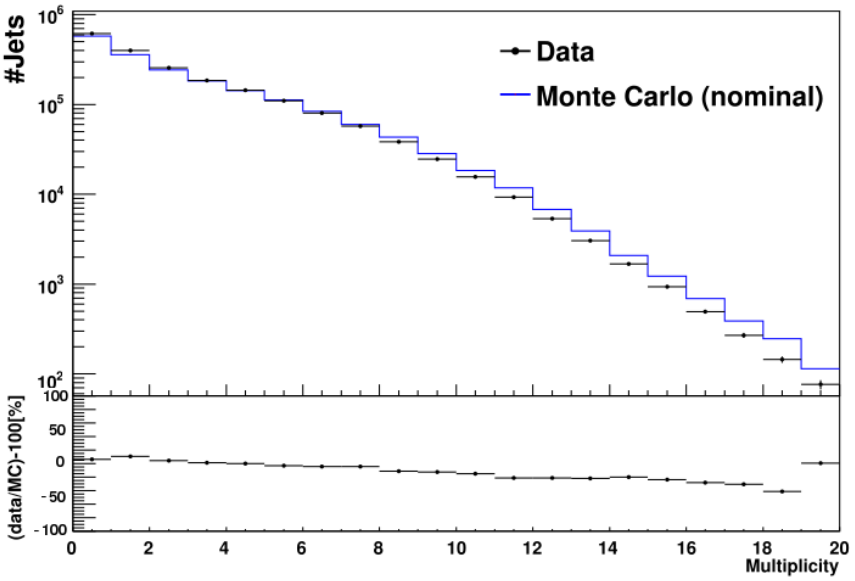

(a)

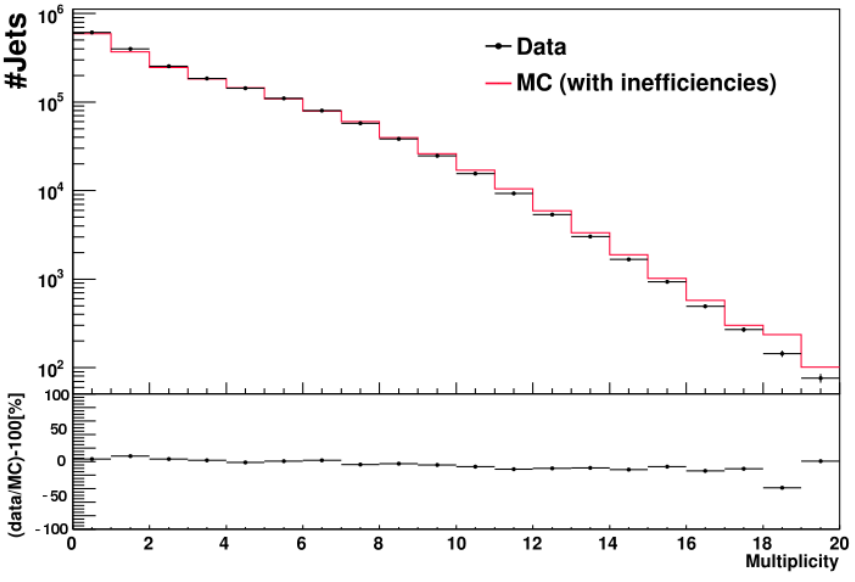

(b)

Figure 35: The jet track multiplicities for (a) default Monte Carlo and (b) with the tracking inefficiencies applied.

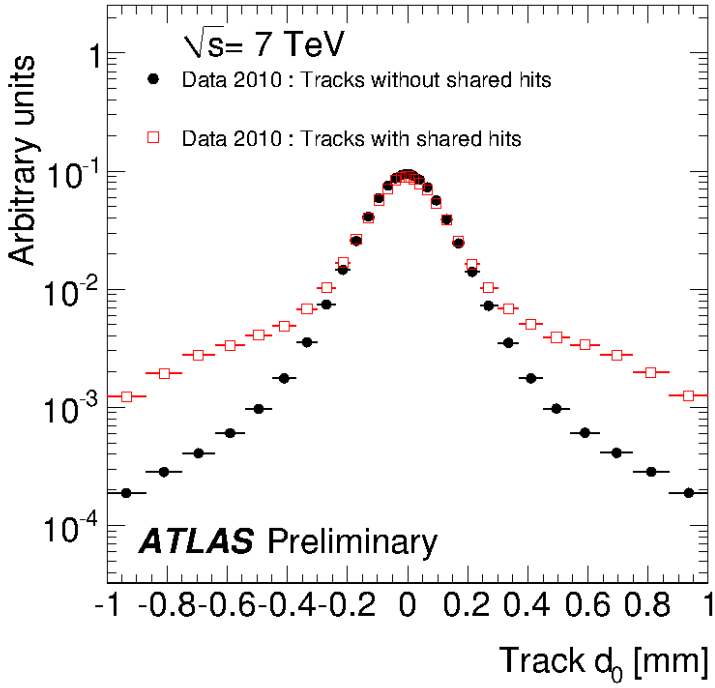

Figure 36: Distribution of the transverse impact parameter d_0 in experimental data for tracks without shared hits (black circles) and for tracks with shared hits (red squares) [85]. The distribution for tracks with shared hits has been normalised to the same area of the distribution for tracks without shared hits.

6.4.5 Jet axis resolution

When a *b* hadron decays, usually ~5mm from the primary vertex, it produces a secondary vertex within a jet of particles that leave tracks in the inner detector and deposit energy in the calorimeter. The jet axis is normally defined by the energy measurements in the calorimeter. The jet direction can also be constructed by vectorially adding the momenta of all tracks in the jet. Due to the nature of the measurements, these two definitions can be noticeably different. The jet direction resolution is better in Monte Carlo simulation than in data, and this can lead to different *b* tagging efficiencies. For instance, the lifetime sign of a track in a jet, as discussed in Section 4.7.1, will be affected by the jet direction resolution. To take this into account, the η and ϕ co-ordinates of the jet axis are smeared with a Gaussian centred on zero with a width of 0.015. This value was obtained by taking the average difference between the axis defined in the calorimeter and the axis built from the tracks in the inner detector. Studies show that after smearing the simulation and data have good agreement for ΔR(calo,track) [79]. Applying the jet-axis smearing caused a change in *b* tagging efficiency of +0.8 % over the full p_T range.

6.4.6 Jet energy scale uncertainty

The jet energy scale used in this analysis has an average uncertainty of 4 % [86]. If the jet energy scale is different to that in data, the p_T spectrum will be biased, which will result in a change in b tagging efficiency in particular regions of p_T due to migration across the jet p_T bin boundaries. To measure this effect, the jet energy scale is shifted up and down by 4 %, which produced shifted the b tagging efficiency by +0.2 % and +1.2 % respectively over the full p_T range. Shifting the jet energy scale down produces a larger effect as some tracks in jets are lost as their energy is shifted below the track selection threshold.

6.5 *b* tagging efficiency

The b tagging efficiency in bins of jet p_T calculated from Monte Carlo is shown in Figure 37. The systematic error on the b tagging efficiency from each of the effects studied in this analysis is calculated by taking the difference between the default efficiency and the efficiency after applying the effect. These are summed in quadrature to give the total systematic error. The b tagging efficiency scale factors used to calibrate the SV0 tagging algorithm, derived using the ${p_T}^{rel}$ method are shown in Figure 38. For comparison, the total systematic error derived from the effects studied in this analysis is shown, with a scale factor of unity, and is compatible with the ${p_T}^{rel}$ scale factors, within uncertainties.

6.6 *c* tagging efficiency

At the time of this study, there was no explicit measurement of the c tag efficiency in ATLAS data, and the scale factor was taken to be the same as for the b tagging efficiency. This is based on the fact that both b tag and c tag efficiencies are dominated by decays of long-lived hadrons and therefore should show similar behaviour. The systematic uncertainty provided in the calibration for the c-tagging efficiency scale factor is 20 %, corresponding to the current 10 % uncertainty on the b tagging efficiency scale factor inflated by a factor of 2. To validate this assumption, which is made for the calibration of the SV0 tagger, a cross check was performed. The c-tag efficiency, shown in Figure 39, and the ratio of the b and c tag efficiencies, shown in Figure 40, were calculated in bins of jet p_T for the set of systematic effects. A table displaying this ratio for each systematic contribution is shown in Appendix A. The ratio of the b and c tagging efficiencies does not vary by more than 10 % for each systematic effect in any given p_T bin, and both the b and c efficiencies show similar variations for each effect. This supports the decision to take the scale factor for the c efficiency to be the same as that for the b efficiency with the inflated systematic error of 20 % in the calibration of the basic b tagging algorithms. See [79] for more details

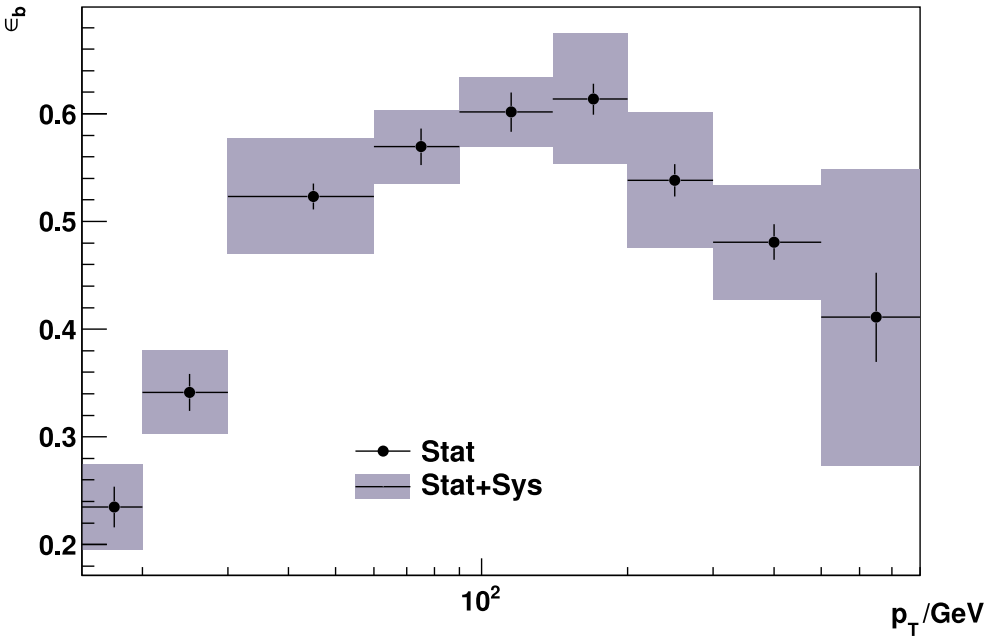

Figure 37: The b tag efficiency in bins of jet p_T.

on the SV0 calibration.

6.7 Summary

In this study, a range of systematic effects have been measured that cause significant differences between important quantities in data and Monte Carlo, that can lead to different values for the *b* tagging efficiency of a given *b* tagging algorithm in data and simulation. These effects have been propagated through the analysis chain by re-running the *b* tagging algorithm to produce a variation in the *b* tagging efficiency resulting from each individual effect.

This method can be used to provide calibration for any *b* tagging algorithm in the form of a set of jet-p_T-dependent systematics, which take into account the differences between efficiencies in data and simulation. This method has the flexibility in that it is not limited to jets with $p_T < 140$ GeV, and can provide calibration for analyses requiring high p_T *b* jets. This method has been applied to the SV0 tagging algorithm and results are seen to be consistent with the current recommended calibrations, and offer the possibility to extend these calibrations.

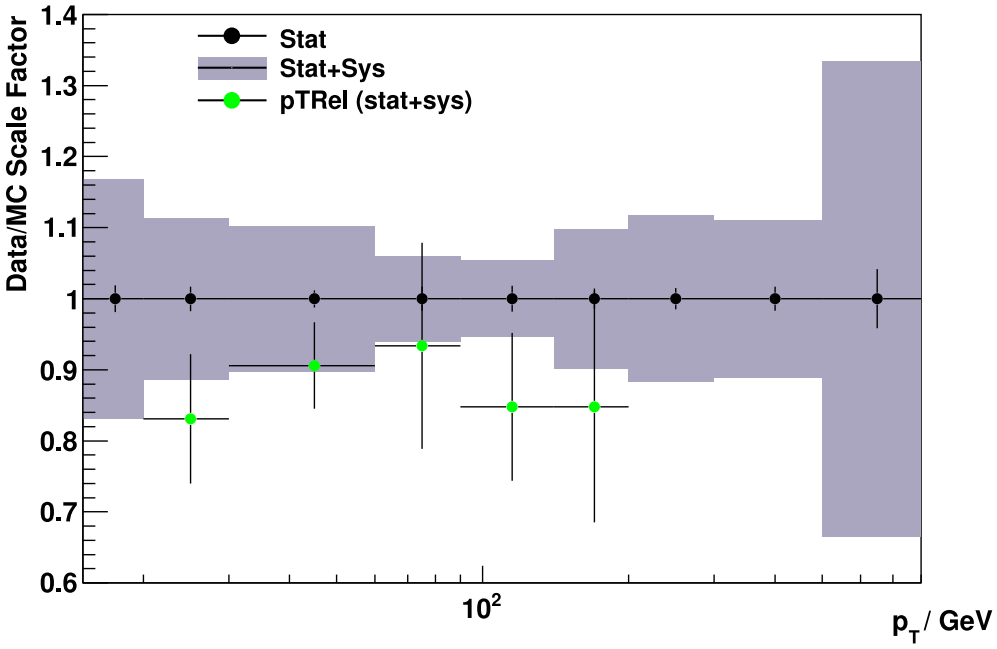

Figure 38: Data to MC scale factors for the b tag efficiency. The green points are the data/MC scale factors derived using the p_T^{rel} method. The grey bands centred on unity show the combination of the systematic effects studied in this analysis.

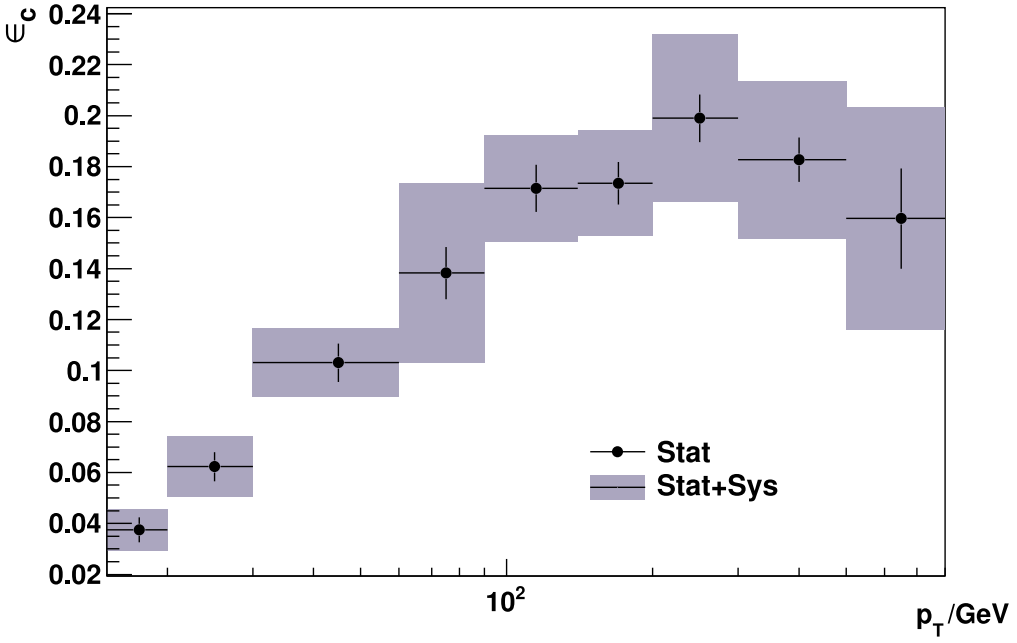

Figure 39: The charm tagging efficiency in bins of jet p_T for jets passing the selection cuts.

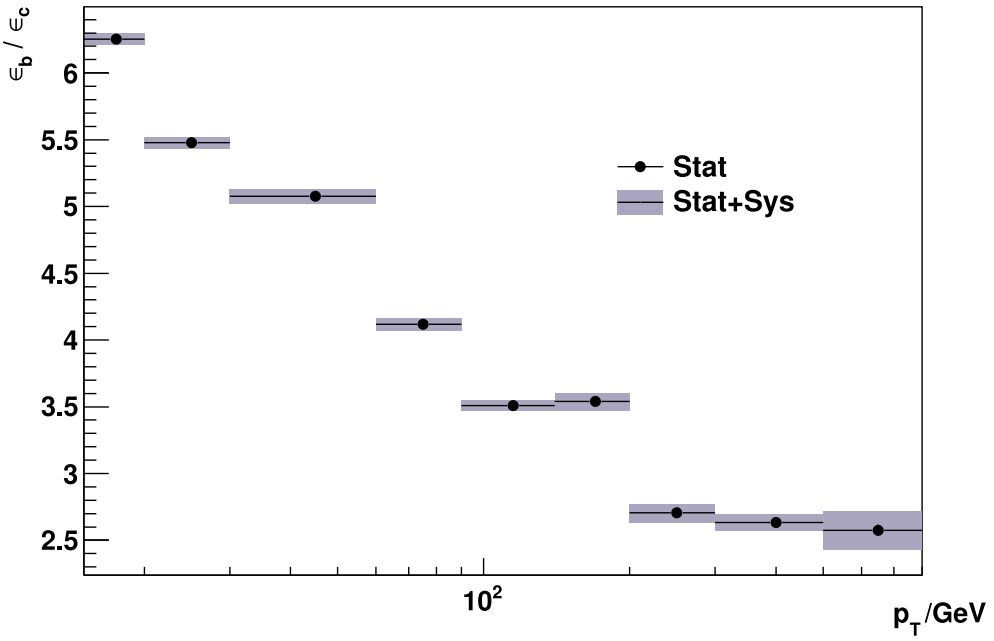

Figure 40: b tag efficiency divided by the c tag efficiency in bins of jet p_T showing the total systematic from the effects studied in this analysis.

Chapter 7

Measurement of the Z + b jet cross section

7.1 Introduction

A differential measurement of the cross-section for the associated production of Z bosons with b jets is useful for a number of reasons. The $Z+b$ jets signal provides a clean signature with low background that can be used to test the current theoretical models and event generators that are used to produce Monte Carlo simulation. The modelling of heavy flavour jet production in current models and generators are susceptible to fairly large uncertainties from the PDFs and scale choices. The fixed and variable flavour schemes provide two methods of calculating matrix elements for final states involving b jets, and the $Z + b$ measurement can compare these models to data and see which is more accurate. In addition to testing theoretical predictions and event modelling, an improved measurement of this cross-section will allow measurements of the Higgs boson to be refined.

In this chapter, the integrated and differential cross-sections for the production of a Z boson in association with one or more b jets is measured in 2011 ATLAS data, and the results are compared with leading order Monte Carlo data simulated using the ALPGEN event generator, and with next-to-leading-order parton level peturbative QCD predictions calculated by the MCFM program.

7.2 Data and Monte Carlo Samples

The data used in this analysis was recorded between 13th March and 30th October 2011, with an integrated luminosity of 4.7 fb^{-1}. The data quality selection established by the top working group, is applied to the sample, ensuring only data collected during stable beam periods and when all detector sub-systems were fully operational is used. The data periods, shown with the integrated luminosity after applying this selection, and the triggers that were used for each period, are shown in Table 9. The event filter triggers that are used in this analysis are named according to the p_T threshold they must pass and the object quality definition that is used, for example, EF_2E12TVH_MEDIUM denotes an event filter trigger that requires two electrons with $p_T > 12$ GeV that pass the medium electron identification criteria as defined in Section 4.3, with the 'vhT' denoting a variable cut on the hadronic leakage. The 'MG' in the muon triggers denotes the use of the 'muon girl' algorithm described

The instantaneous luminosity of the proton-proton collisions delivered by the LHC increased almost exponentially over the course of the year, and so the trigger used is specific to the data period, which reflects the changes that were made to the trigger menu to manage the increased trigger rates. Further information on the trigger menu for 2011 can be found in [88]. The unprescaled triggers recommended by the W/Z group for 2011 analyses are used, with di-lepton triggers for the electron channel and single lepton triggers for the muon channel. The leptons selected in the offline analysis are required to match the trigger fired in the event, with one lepton match required for the single lepton trigger and two for the dilepton trigger. This matching is implemented at the Z mass window stage of the selection.

Monte Carlo simulation is used in this analysis to derive the shape of flavour templates, which use a variable that gives the best possible discrimination between the distributions for b, c, and light flavour jets. The shapes of these templates are corrected by reweighting the charged particle multiplicity to that in data, as described in Section 7.5.6. The templates are fitted to data using an extended likelihood fit to obtain the b jet yield in data.

Z decay channel	data periods	trigger	integrated luminosity [fb^{-1}]
$Z \to ee$	D-J	EF_2e12_MEDIUM	1.7
$Z \to ee$	K	EF_2e12T_MEDIUM	0.6
$Z \to ee$	L-M	EF_2e12TVH_MEDIUM	2.3
$Z \to ee$	D-M		4.7
$Z \to \mu\mu$	D-I	EF_mu18_MG	1.4
$Z \to \mu\mu$	J-M	EF_mu18_MG_MEDIUM	3.2
$Z \to \mu\mu$	D-M		4.7

Table 9: Triggers used and integrated luminosities collected during 2011 data taking periods.

The Monte Carlo samples involve a final state with two leptons and one or more b jets and are generated using the ALPGEN matrix element event generator [89], with the showering of the partons modelled by the HERWIG parton shower program [90]. The signal samples listed in Table 10 consist of two types of processes generated by calculating exact matrix-elements. The $Zb\bar{b}$ samples involve a Z boson and a pair of bottom quarks, produced from gluon splitting in the initial state, with the bottom quark mass taken into account. Often, the $\bar{b}$ quark remains close to the parent proton and is undetected. Additional samples of this process are generated with 0-3 extra light partons. The $Z + jets$ samples involve a Z boson produced

with 0-4 light partons, where b quarks are produced from gluon splitting, and may be reconstructed in the same jet. In the signal samples, the Z boson, b quarks, and additional light partons are produced directly from the hard scatter process or from gluon splitting in the initial or final state. The background samples, listed in Table 11, consist of $t\bar{t}$ production, single top, diboson, and W+jets final states. The background samples are generated using the ALPGEN, JIMMY [91], and MC NLO [92] event generators. $t\bar{t}$, single top, and WW production can mimic the $Z + b$ jet signature if the leptons produced from the W decays are falsely reconstructed as a Z. WZ and ZZ production may also produce b jets and dilepton final states. W + *jets* production can mimic the $Z + b$ final state if the jets are falsely reconstructed as leptons.

7.2.1 Removing heavy flavour event overlap in simulated data

There is a double-counting of events when combining the ALPGEN Monte Carlo samples, which is removed using the Heavy Flavour Overlap Removal procedure (HFOR) [93]. The overlap occurs for events containing a lepton pair and a pair of bottom quarks, which can appear in both the ALPGEN $Z + b\bar{b}$ signal and Z+light parton background samples. Leading order diagrams for this process are shown in Figure 5 by the bottom three diagrams. In the signal MC, a lepton pair with a pair of bottom quarks are produced directly from the matrix element calculations in ALPGEN, which uses massive b quarks and can produce additional light partons. The Z+light parton background MC contains this signal from the ALPGEN calculation of a lepton pair plus gluon final state when the gluon splits into a $b\bar{b}$ pair in the parton shower, as shown by the bottom middle diagram in Figure 5.

The HFOR procedure removes this duplication by separating these events based on the angular separation ΔR of the $b\bar{b}$ pair. It is assumed that the parton shower better describes the kinematics and yield for small-angle gluon splitting, while the exact matrix-element calculation is more accurate for large-angle splitting [93]. The b quarks in the event are classified based on how they were produced. b quarks can originate from the ALPGEN matrix element calculation, gluon splitting in the parton shower, from multi-parton interactions in the underlying event, or from the b quark content of the colliding protons.

There are also b quarks produced by the parton shower to conserve flavour from the PDF b quarks involved in the hard scatter. These only appear from the multi-parton interactions, and since ALPGEN does not use the b PDF they need not be considered in the overlap removal. Events are then removed using the classification of the final state b quarks. In the Z+ light parton samples, events with a $b\bar{b}$ pair from the parton shower are only kept if the separation between them satisfies $\Delta R < 0.4$. In the $Z + b\bar{b}$ samples, events with a $b\bar{b}$ pair from the matrix element calculation are only kept if $\Delta R > 0.4$.

ID	description	MC generator(s)	$\epsilon_F \cdot \sigma$ [pb]	k-factor	N_{evts}
109300	$Zb\bar{b}$+0 part., $Z \to ee$	Alpgen+Jimmy	6.57	1.25	409999
109301	$Zb\bar{b}$+1 part., $Z \to ee$	Alpgen+Jimmy	2.48	1.25	160000
109302	$Zb\bar{b}$+2 part., $Z \to ee$	Alpgen+Jimmy	0.89	1.25	60000
109303	$Zb\bar{b}$+3 part., $Z \to ee$	Alpgen+Jimmy	0.39	1.25	30000
107650	Z+0 part., $Z \to ee$	Alpgen+Jimmy	668.32	1.25	6618284
107651	Z+1 part., $Z \to ee$	Alpgen+Jimmy	134.36	1.25	1334897
107652	Z+2 part., $Z \to ee$	Alpgen+Jimmy	40.54	1.25	2004195
107653	Z+3 part., $Z \to ee$	Alpgen+Jimmy	11.16	1.25	549949
107654	Z+4 part., $Z \to ee$	Alpgen+Jimmy	2.88	1.25	149948
107655	Z+5 part., $Z \to ee$	Alpgen+Jimmy	0.83	1.25	50000
109305	$Zb\bar{b}$+0 part., $Z \to \mu\mu$	Alpgen+Jimmy	6.56	1.25	409949
109306	$Zb\bar{b}$+1 part., $Z \to \mu\mu$	Alpgen+Jimmy	2.47	1.25	160000
109307	$Zb\bar{b}$+2 part., $Z \to \mu\mu$	Alpgen+Jimmy	0.89	1.25	60000
109308	$Zb\bar{b}$+3 part., $Z \to \mu\mu$	Alpgen+Jimmy	0.39	1.25	29999
107660	Z+0 part., $Z \to \mu\mu$	Alpgen+Jimmy	668.68	1.25	6615230
107661	Z+1 part., $Z \to \mu\mu$	Alpgen+Jimmy	134.14	1.25	1334296
107662	Z+2 part., $Z \to \mu\mu$	Alpgen+Jimmy	40.3	1.25	1999941
107663	Z+3 part., $Z \to \mu\mu$	Alpgen+Jimmy	11.19	1.25	309899
107664	Z+4 part., $Z \to \mu\mu$	Alpgen+Jimmy	2.75	1.25	35000
107665	Z+5 part., $Z \to \mu\mu$	Alpgen+Jimmy	0.77	1.25	50000

Table 10: Signal MC samples, filter efficiency times cross section, k-factor (correcting for NLO terms) and number of events.

7.3 Selection

The $Z + b$ jet selection is similar to the baseline recommendations from the ATLAS WZ group, with various modifications to improve background rejection and signal efficiency.

The event vertex is chosen to be that with the largest sum of $(p_T^{trk})^2$, and must have three or more tracks assigned to it otherwise the event is rejected.

ID	description	MC generator(s)	$\epsilon_F \cdot \sigma$ [pb]	k-factor	N_{evts}
105200	$t\bar{t}$	MC NLO+Jimmy	79.01	1.146	14983835
108346	Wt inclusive	MC NLO+Jimmy	14.59	1.079	899694
108344	t s-channel	MC NLO+Jimmy	0.47	1.064	299998
108341	t t-channel	MC NLO+Jimmy	7.12	0.979	299999
105930	ZZ, $\ell\ell qq$	MC NLO+Jimmy	0.559	-	25000
105942	W^+Z, $qq\ell\ell$	MC NLO+Jimmy	0.5415	-	24950
105972	W^-Z, $qq\ell\ell$	MC NLO+Jimmy	0.2944	-	100000
107680	W+0 part., $W \to e\nu$	Alpgen+Jimmy	6930.50	1.196	10495000
107681	W+1 part., $W \to e\nu$	Alpgen+Jimmy	1305.30	1.196	7570000
107682	W+2 part., $W \to e\nu$	Alpgen+Jimmy	378.13	1.196	3770000
107683	W+3 part., $W \to e\nu$	Alpgen+Jimmy	101.86	1.196	1010000
107684	W+4 part., $W \to e\nu$	Alpgen+Jimmy	25.68	1.196	1075000
107685	W+5 part., $W \to e\nu$	Alpgen+Jimmy	6.99	1.196	1000000
107690	W+0 part., $W \to \mu\nu$	Alpgen+Jimmy	6932.40	1.195	10495000
107691	W+1 part., $W \to \mu\nu$	Alpgen+Jimmy	1305.90	1.195	7500000
107692	W+2 part., $W \to \mu\nu$	Alpgen+Jimmy	378.07	1.195	3770000
107693	W+3 part., $W \to \mu\nu$	Alpgen+Jimmy	101.85	1.195	1010000
107694	W+4 part., $W \to \mu\nu$	Alpgen+Jimmy	25.72	1.195	1000000
107695	W+5 part., $W \to \mu\nu$	Alpgen+Jimmy	7.00	1.195	1000000
107280	$Wb\bar{b}$+0 part., $W \to \ell\nu$	Alpgen+Jimmy	47.35	1.2	1000000
107281	$Wb\bar{b}$+1 part., $W \to \ell\nu$	Alpgen+Jimmy	35.76	1.2	1240000
107282	$Wb\bar{b}$+2 part., $W \to \ell\nu$	Alpgen+Jimmy	17.33	1.2	175000
107283	$Wb\bar{b}$+3 part., $W \to \ell\nu$	Alpgen+Jimmy	7.61	1.2	700000

Table 11: Background MC samples, filter efficiency times cross section, k-factor, and number of events. ll denotes ee or μμ.

Selected electrons must have $p_T > 20$ GeV, and must pass the medium electron identification criteria outlined in Section 4.3. Electrons must be contained well within the inner detector acceptance, with $|\eta| < 2.47$, and must not be reconstructed in the calorimeter crack region, $1.37 < |\eta_e| < 1.52$. To ensure that the electron tracks are well-defined, the inner detector tracks must have a longitudinal impact parameter less than 1mm and a transverse impact parameter significance less than 10. Initially the η measurement from the calorimeter clusters is used to remove electrons reconstructed in the calorimeter crack region, and for the η kinematic cut for the detector acceptance. For the remainder of the electron selection, the η value calculated from the track information is used.

Muons selected for analysis must be STACO combined muons, with $p_T > 20$ GeV and $\eta < 2.4$. Muon isolation is defined using $\Sigma p_T^{ID}(dR = 0.2)$, which defines the transverse momentum sum of the inner detector tracks within a cone of radius $R \leqslant 0.2$ around the muon. The cuts on the muon longitudinal impact parameter, z_0^{PV}, and transverse impact parameter significance, $|d_0^{PV}/\sigma(d_0^{PV})|$, where both impact parameters are extrapolated to the primary vertex, are tighter than in the baseline selection. The Z selection requires oppositely charged leptons with an invariant mass between 76 and 106 GeV, also tighter than the baseline to improve rejection of top background. The $Z \rightarrow ee$ selection requires there are no further electrons or muons reconstructed in the event. The $Z \rightarrow \mu\mu$ selection requires there are not selected electrons that overlap with a selected muon within a cone of $R = 0.1$.

The jet selection uses anti-k_T jets built from topoclusters with $R = 0.4$, with $p_T > 20$ GeV and $y < 2.4$. Jets are corrected to the EM+JES scale with offset and beam-spot corrections. Overlap removal is performed to remove jets that overlap with a signal lepton within a cone of radius $R < 0.5$, where R is calculated at the EM scale, as this prevents including duplicate reconstructions of the same object. Applying the E_T^{miss} cut requires that the event is checked for badly reconstructed jets that affect the E_T^{miss} measurement. Jets may be reconstructed from fake energy deposits in the calorimeter due to noisy calorimeter cells or hardware problems that can cause energy spikes. An event is rejected if any jets pass a set of criteria based on the calorimeter information or if the jet overlaps with a signal lepton within a cone of $R < 0.3$. The jet vertex fraction, which measures the probability that a jet originated from a particular vertex, must be greater than 0.75, which helps to reject jets from pileup interactions.

A cut is performed on the maximum missing transverse energy to improve rejection of top background, and a narrower dilepton mass window is applied to further reject the top background and background from multijet production, as both have an approximately flat dilepton invariant mass distribution. To utilise the full range of the b tagging calibration provided by the ATLAS heavy flavour tagging group,

the jet rapidity, y, is used rather than pseudorapidity, since this is how it is defined in the calibration.

The b jet selection tags b jets using the MV1 b tagging algorithm (see Section 4.7.3), with a weight cut applied that yields a b tagging efficiency of 75 % in selected $t\bar{t}$ events.

7.4 Particle level selection

To extract a detector-independent cross-section, the $Z + b$ jets signal in simulation must be extracted at particle level, so that the kinematic phase space of the measurement is defined. This is done by performing a selection on the truth information provided by the event generator that is matched as closely as possible to the detector level selection to avoid introducing theoretical model-dependent corrections. This is then used to determine the C factor, defined as the number of tagged b jets measured in data divided by the number of b jets determined from the Monte Carlo truth information after the particle level selection. Dividing the measured cross-section determined from the b jet yield by this C factor then produces the fiducial cross-section. The particle level selection involves the following steps:

- Truth leptons are corrected by 'dressing' them with all photons within a cone of $R < 0.1$, as these are most likely bremsstrahlung
- The two highest-p_T leptons with the same flavour are required to have $p_T > 20$ GeV, $|\eta| < 2.5$, have opposite charge, and have a dilepton mass such that $76 < m_{ll} < 106$ GeV
- The jet algorithm is run over all remaining truth particles and jets are reconstructed with the anti-k_T algorithm with a distance parameter of 0.4
- Jet selection: $p_T > 20$ GeV and $y < 2.4$. Jets within $\Delta R < 0.5$ of signal lepton are removed
- Heavy flavour matching is performed, so that any weakly decaying b hadron with $p_T > 5$ GeV and with no b hadron daughters is considered. Any jet which matches such a hadron, based on a simple $\Delta R < 0.3$ matching, is considered as a b jet. If there is no b hadron, a charm hadron is searched for and the jet tagged as a c jet if one is found. If neither are found, the jet is labelled a light jet

7.5 Corrections

Specific software packages are provided by the ATLAS combined performance groups to apply scale factors and event reweighting to correct for a number of effects in simulated data. Versions of the common packages used to are shown in Appendix B.

Event vertex definition	vertex with largest $\Sigma(p_T^{trk})^2$
Event vertex quality	≥ 3 tracks assigned to event vertex
Electron selection criteria	$p_T^e > 20$ GeV
	medium quality electron
	crack region $1.37 < \lvert\eta_e\rvert < 1.52$ excluded
	$\lvert\eta_e\rvert < 2.47$
	electron track $z_0 < 1$ mm, $\lvert d_0/\sigma(d_0)\rvert < 10$
Muon selection criteria	STACO combined muons
	$p_T^\mu > 20$ GeV
	$\lvert\eta_\mu\rvert < 2.4$
	$z_0^{PV} < 1$ mm, $\lvert d_0/\sigma(d_0)\rvert < 3$
	isolation: $\Sigma p_{\mathrm{T}}(ID)/p_{\mathrm{T}} < 0.1$ with $p_{\mathrm{T}} = 20$ GeV
$Z \to ee$ selection	2 oppositely charged selected electrons
	no further e or μ in event
	$76 < M_{ee} < 106$(GeV)
$Z \to \mu\mu$ selection	2 oppositely charged selected muons
	no selected e with $\Delta R(e,\mu) < 0.1$
	$76 < M_{\mu\mu} < 106$(GeV)
E_T^{miss} criteria	pass "looser" MET cleaning
(to suppress top background)	MET < 30 GeV, METRefFinal definition
Jet selection criteria	anti-k_T jets built from topo-clusters with $R = 0.4$
	$p_T^{jet} > 20$ GeV
	$\lvert y^{jet}\rvert < 2.4$
	Jet to signal lepton $\Delta R > 0.5$
	$JVF > 0.75$
	pass "looser" cleaning requirements
	jet not in LAr region with faulty readout electronics
	$\geqq 1$ b tag, MV1 weight > 0.404 (75% efficiency)

Table 12: Object and event selection criteria used for reconstructed events. For generator level selection, the same kinematic cuts are applied on truth variables where applicable.

7.5.1 Pileup reweighting

The beam parameters were tuned and optimised throughout the 2011 data taking period to maximise the delivered luminosity. The physical cross-section of the beam was reduced throughout 2011, and this increased the pileup interactions, so that later data periods have a larger average for the number of interactions per bunch crossing, $< \mu >$. This is taken into account in simulation by generating sets of events with different values of $< \mu >$ corresponding to each data period, which must then be reweighted to match the corresponding luminosity in data (similar to the procedure used in Section 6.3.3). The distribution of the number of vertices for events passing the selection is shown in Figure 41.

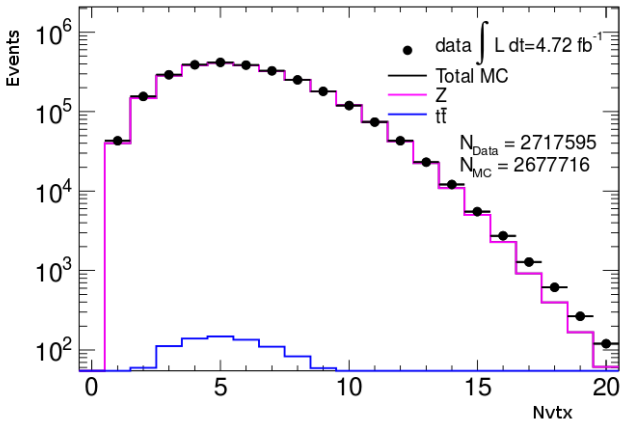

Figure 41: Distribution of the number of vertices in the event with three or more associated tracks.

7.5.2 Vertex z-coordinate reweight

In the 2011 dataset, the primary vertex z-coordinate distribution in simulation was wider than that in the data. This is corrected by reweighting the distribution in simulation to match that in data.

7.5.3 Electron corrections

The energy of electrons reconstructed from clusters in the electromagnetic calorimeter must be corrected to take account of the detector response. This is done by applying energy scale factors derived from well-measured resonances, such as $Z \to ee$, $J/\psi \to ee$, or from E/P studies using isolated electrons from $W \to e\nu$ decays [59]. The cluster energy of the electron is adjusted in data using a scale factor, a, with $|a| < 1$, which varies over the electron η and ϕ coordinates:

$$E_{corr} = \frac{E}{1+a} \tag{27}$$

The resolution of electrons in simulation is corrected by applying a smearing procedure to the electron energy that is calculated with the electron p_T and η. The validity range for these corrections is 10 GeV $< E_{electron} <$ 1 TeV. An electon efficiency scale factor is also applied to correct for the trigger, reconstruction and identification efficiencies. All three efficiencies were measured from experimental data using a tag-and-probe method in $Z \rightarrow ee$ events, with the identification efficiency also measured from J/Ψ events [59]. Trigger efficiency scale factors are also applied to simulation.

7.5.4 Muon corrections

The muon momentum resolution is determined using external constraints measured from the analysis of data recorded with the toroid magnet turned off, and from the dimuon mass resolution at the Z boson mass peak [94]. Muons in simulation are corrected by applying an energy scale shift and a resolution smearing based on the muon p_T. A seperate smearing is applied to the inner detector, muon spectrometer, and combined muon tracks. A muon efficiency scale factor is also applied to correct for the trigger, reconstruction and identification efficiencies. The muon reconstruction efficiencies were measured from experimental data using a tag-and-probe method in $Z \rightarrow \mu\mu$ events [63].

7.5.5 b tagging efficiency scale factors

As described in Section 4.7 and Chapter 6, the b tagging efficiency in data is estimated by correcting the efficiency in simulation. The b tagging efficiency scale factors provided by the ATLAS heavy flavour tagging working group, defined as data-to-MC efficiencies, are derived from a combination of measurements from tag counting and kinematic selection in control samples of $t\bar{t}$ events [71], measurements involving the relative transverse momentum of muons in jets [95], and measurements that use an 8-parameter multivariant technique [74]. These scale factors are parametrised as a function of the jet p_T and η and are applied based on the truth flavour of the jet generated by HERWIG (light+charm or bottom).

7.5.6 Charged particle multiplicity weighting

The $Z + b$ jets cross section measurement is performed using an extended maximum likelihood fit to data, using probability templates derived from simulation. The flavour discriminant chosen to fill these templates is the JetFitterCombNN neural net response that discriminates b jets from c jets, $\ln(pb/pc)$. It is important to check that the shapes of templates in simulation for a given jet flavour accurately represent the shape expected in data, as this ensures the fit results are not significantly systematically biased. This

is investigated using a $t\bar{t}$ control region enriched in b jets, with a muon or electron and four or more jets in the final state, where two jets pass the MV1 algorithm 75 % tagging requirement. The top sample used for this is the same as the top background sample listed in Table 11.

Mismodelling of heavy flavour sensitive variables can originate from the production, decay and reconstruction of b hadron daughters in simulation. The comparison of the distributions of the fit variable, $\ln(pb/pc)$, derived from the outputs of the JetFitterCombNN algorithm in data and simulation show a difference between the p_T of the leading and sub-leading jets, indicating that $\ln(pb/pc)$ has a p_T dependence. This is interpreted as a shape distortion due to mismodelling by the neural network algorithm response in simulation. To identify which variables might contribute to this effect, each input variable was reweighted so the overall distribution in simulation matches that in data, and the agreement between data and simulation for the distributions of $\ln(pb/pc)$ was examined for improvement. The best results were achieved by reweighting the number of reconstructed tracks used in secondary vertex fits by the JetFitter algorithm. The correction weight is mostly sample independent, except for at higher track multiplicities where statistics become limited in both data and simulation. The mismodelling of the number of reconstructed tracks used in secondary vertex fits results from the incorrect modelling of b hadron properties in simulation by outdated decay tables in the HERWIG parton shower program, which gives rise to an incorrect average number of stable charged particles produced by the b hadron decay. It is known that the EVTGEN package has more accurate decay tables [96], and so the distribution for the number of reconstructed tracks used in secondary vertex fits in the ALPGEN+HERWIG samples is reweighted event-by-event to that in EVTGEN. This improves the agreement between the $\ln(pb/pc)$ fit variable in data and simulation. This is seen in Figure 42, which shows the flavour discriminant variable before and after the reweighting procedure. There is much better agreement between data and simulation, particularly for b jets, which have a large value for $\ln(pb/pc)$.

7.6 Estimation of Multi-jet QCD Background

The available Monte Carlo multijet samples have relatively low statistics and large systematics, mainly due to the uncertainty on the modelling of the rate of misidentification of jets as leptons. Since the $Z + b$ jets signal contains two isolated leptons and one or two b tagged jets, there would be very few multijet events in the final selection and hence large statistical uncertainties. In order to avoid this, the contamination from multijet events in the inclusive $Z + b$ jet selection is estimated with a data-driven method. The multijet background is discriminated from the signal, and any other physics processes with

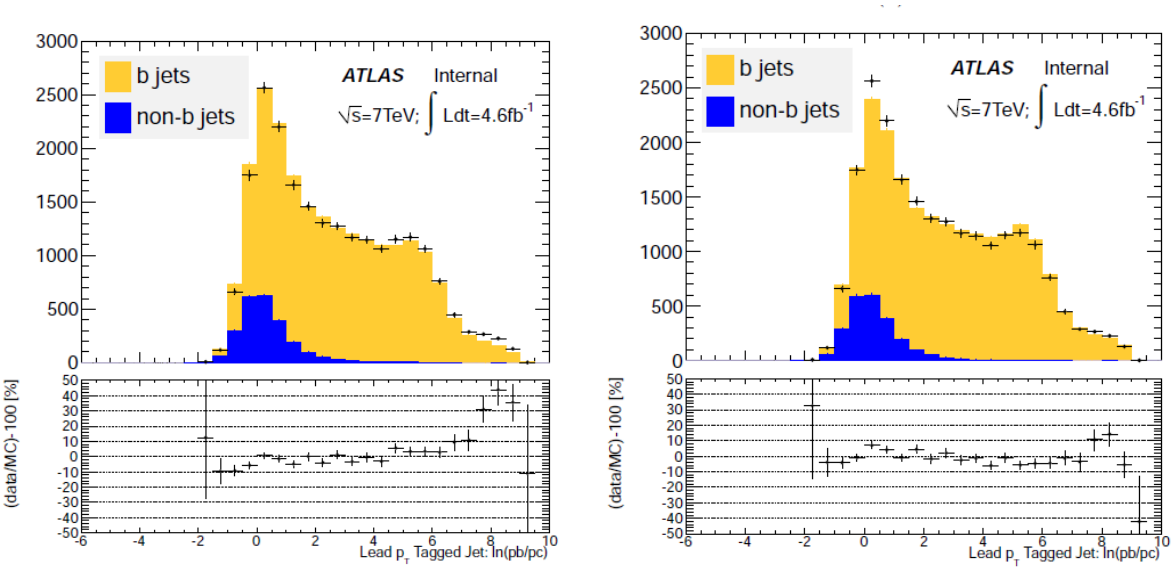

(a) (b)

Figure 42: Distribution of the JetFitterCombNN neural network output, $\ln(pb/pc)$*, used for the flavour templates, (a) before and (b) after the reweighting procedure [96].*

at least one lepton passing the selection, using the shape of the dilepton invariant mass distributions. For both the electron and muon channels, after the full lepton selection, the shape of the di-lepton invariant mass distribution can be modelled with the function:

$$M(m_{ll};\alpha_l, N_{\overline{mj},l}, N_{mj,l}) = N_{\overline{mj},l}\, g_l(m_{ll}) + N_{mj,l}\, f(m_{ll};\alpha_{l,j}) \tag{28}$$

The number of multijet events passing the selection, $N_{\overline{mj},l}$, and the number of signal plus non multijet background events, $N_{mj,l}$, are obtained by fitting the observed m_{ll} distribution in data with Equation 28. The normalised distribution of the signal and non-multijet background events, $g_l(m_{ll})$, is estimated from Monte Carlo samples. $f(m_{ll};\alpha_l)$ is the normalised distribution for the multijet events. The shape of the fake dilepton invariant mass in multijet events is derived from a fit to data in a control region, defined by applying a selection with criteria similar to the inclusive $Z + b$ jet selection, but modified to enrich the sample with multijet background events. For the electron channel, the control region is obtained by removing the b tagging requirement, and only applying the electron quality requirement for one electron. In the muon channel, the impact parameter cuts are relaxed, and both muons are required to be anti-isolated ($\Sigma p_T(\mathrm{ID})/p_T > 0.1$). In both channels, the dilepton invariant mass range is restricted to 70-120 GeV. The analytic expression used for the shape of the invariant mass of multijet events $f(m_{ll};\alpha_l)$ is an exponential decay, with decay parameter α_l, and this has been verified to be valid in several control regions with different background contaminations. Invariant mass fits in the multi-jet enriched nominal

control region for the electron and muon channels in a region with a Z boson and one b tagged jet are shown in Figure 43.

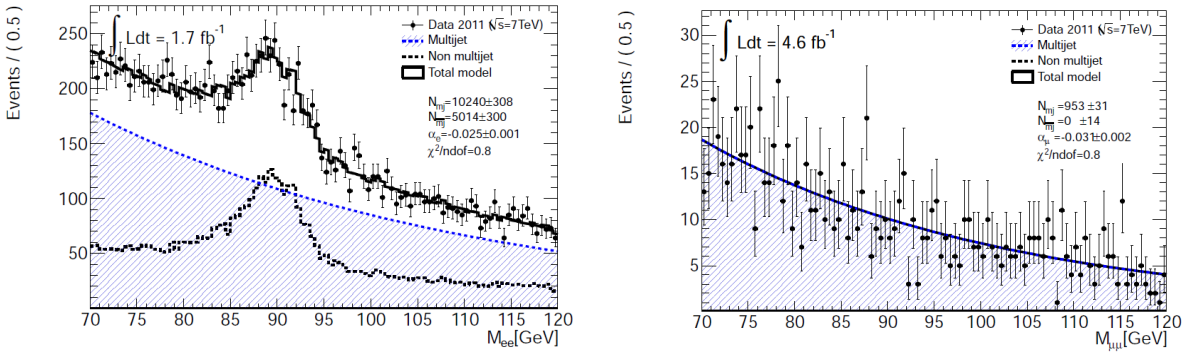

(a) (b)

Figure 43: Invariant mass fits in a multi-jet enriched nominal control region with a Z boson and one b tagged jet for the (a) electron channel, and (b) muon channel [96].

Once the normalisation for the multijet contamination is determined, the flavour template $\ln(p_b/p_c)$ in multijet background events is constructed and used as a fixed input for the template fit to extract the b jet yield in data. The selection used to derive the $\ln(p_b/p_c)$ distribution is based on the selection of the control region with the additional requirement that jets are tagged as b jets.

7.7 Flavour Template Fits

Jets that pass the b tagging requirement are used to fill distributions of the flavour discriminant for the combined electron and muon channels. For this analysis, the flavour discriminant chosen is the JetFitterCombNN neural net response discriminating b jets from c jets, $\ln(pb/pc)$. This variable was chosen since it gave the best discrimination between $l + c$ jets and b jets with a two parameter fit using the number of light plus charm jets, N_{l+c}, and number of b jets, N_b, as free parameters. The template derived to model the QCD background is added to the template constructed with the background samples. The overall normalisation for the template that corresponds to the total non-Z+jets contribution is fixed in the template fit. Figure 44 shows the flavour template before and after the extended likelihood fit.

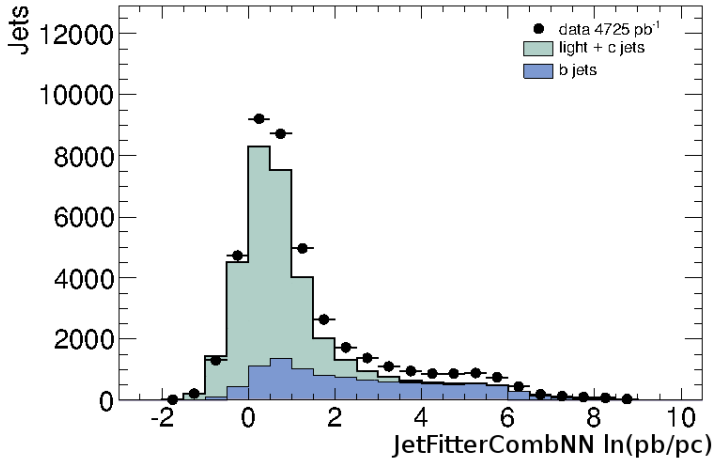

(a)

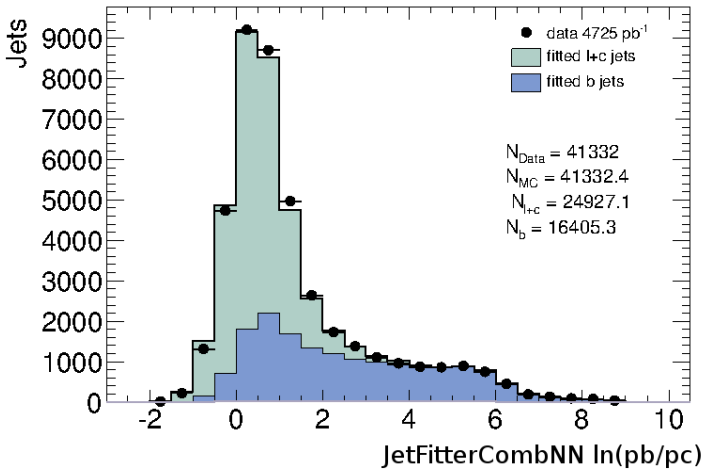

(b)

Figure 44: The flavour discriminant distribution in data and MC (a) before fit and (b) after fit, showing the number of light + charm jets, N_{l+c}, and number of bottom jets, N_b. This produces the b jet yield that is used to calculate the integrated cross section.

7.8 Particle distributions in data and simulation

Shown in Figure 45 are distributions for the electron, muon, Z, jet, and b jet p_T, respectively. The dilepton invariant mass spectra, showing the Z peak, for electron, muon, and combined channels, are show in Figure 46. The rapidity of jets and b jets is shown in Figure 47. The number of jets and number of b jets are show in Figure 48. The MV1 tagging weight distribution used to tag jets as originating from a b quark is shown in Figure 49. All of the control plots shown in this section are constructed after the event, lepton, and jet selection, unless a b tag requirement is stated, and before applying the scaling that results from fitting the simulated flavour templates. This highlights the underestimate of events in the ALPGEN Monte Carlo, particularly for the $Z + b$ jet signal, as seen in the distributions of tagged jets. It can be seen by the shape of these distributions that there is overall a good agreement between data and simulation.

7.9 Systematic uncertainties

Systematic uncertainties are determined by applying various modifications to simulated events. Most systematic effects are studied by directly modifying the reconstructed objects themselves or by applying an event-level weight based on the event properties, which changes the shape of the flavour templates such that the template fit produces a different b jet yield. The size of any given systematic effect is found by taking the difference between the b jet yields produced from fitting the nominal and modified flavour templates. Since applying these modifications can change the number of reconstructed b jets, the effect of the systematic shifts on the correction factor, C, must also be determined. Specific software packages in ATHENA are used to apply each of the systematic shifts (see Appendix B).

7.9.1 b tagging efficiency

The largest systematic effect in this analysis arises from determining the b tagging efficiency. As discussed in Chapter 6 and Section 7.5.5, the number of b jets in data is estimated using the efficiency of tagging b jets derived from simulated data, and a jet-p_T-dependent efficiency scale factor must be applied to correct for differences between data and simulation. The uncertainty resulting from applying these scale factors is found by shifting the scale factors up and down within the uncertainties provided by the b tagging calibration. The tagging efficiency and inefficiency are anti-correlated and so one must be shifted up as the other is shifted down. This is done separately for b jet, c jet and mistag efficiency scale factors.

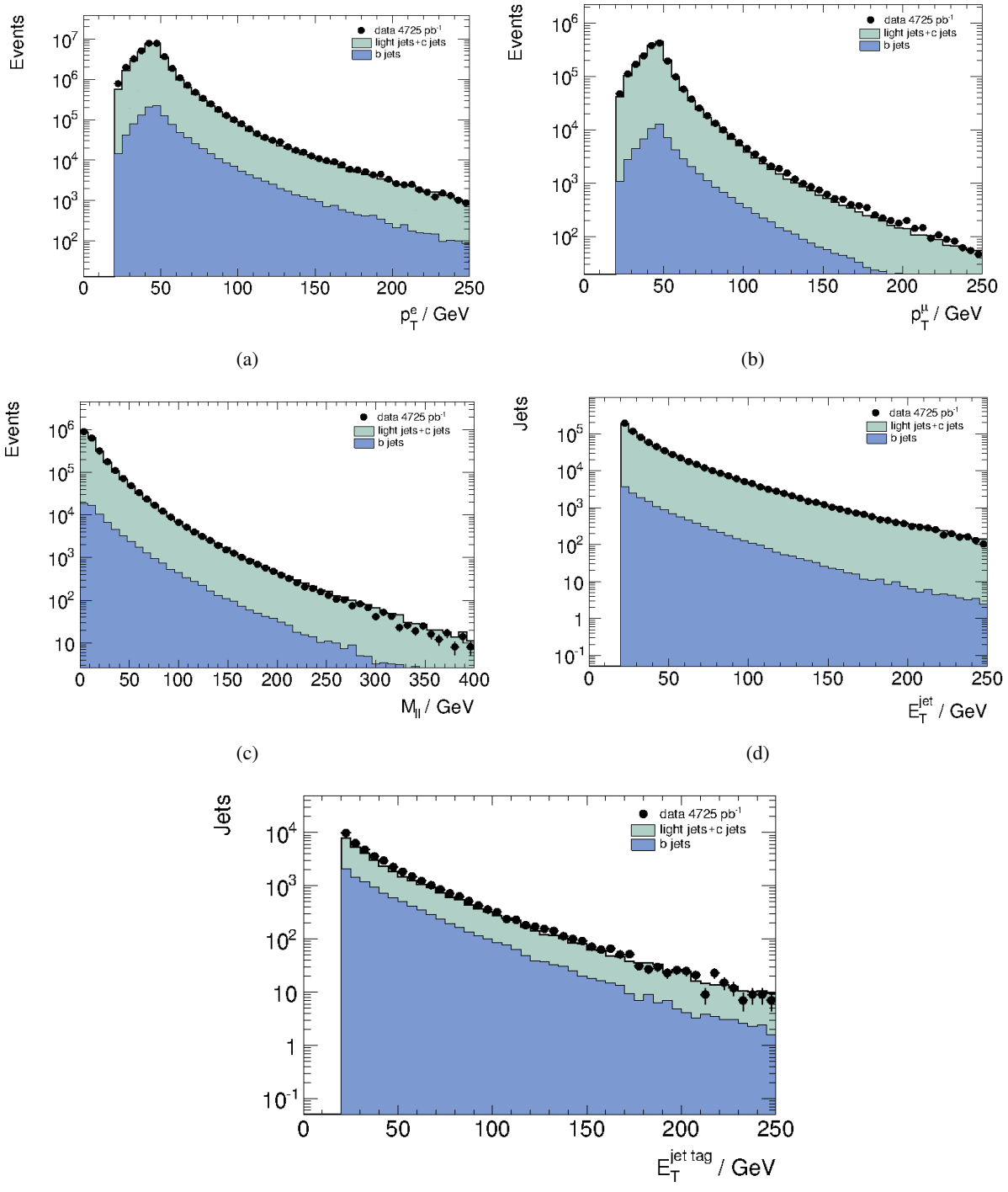

Figure 45: Transverse momenta spectra for (a) electrons, (b) muons, (c) the dilepton system, (d) jets, and (e) b jets.

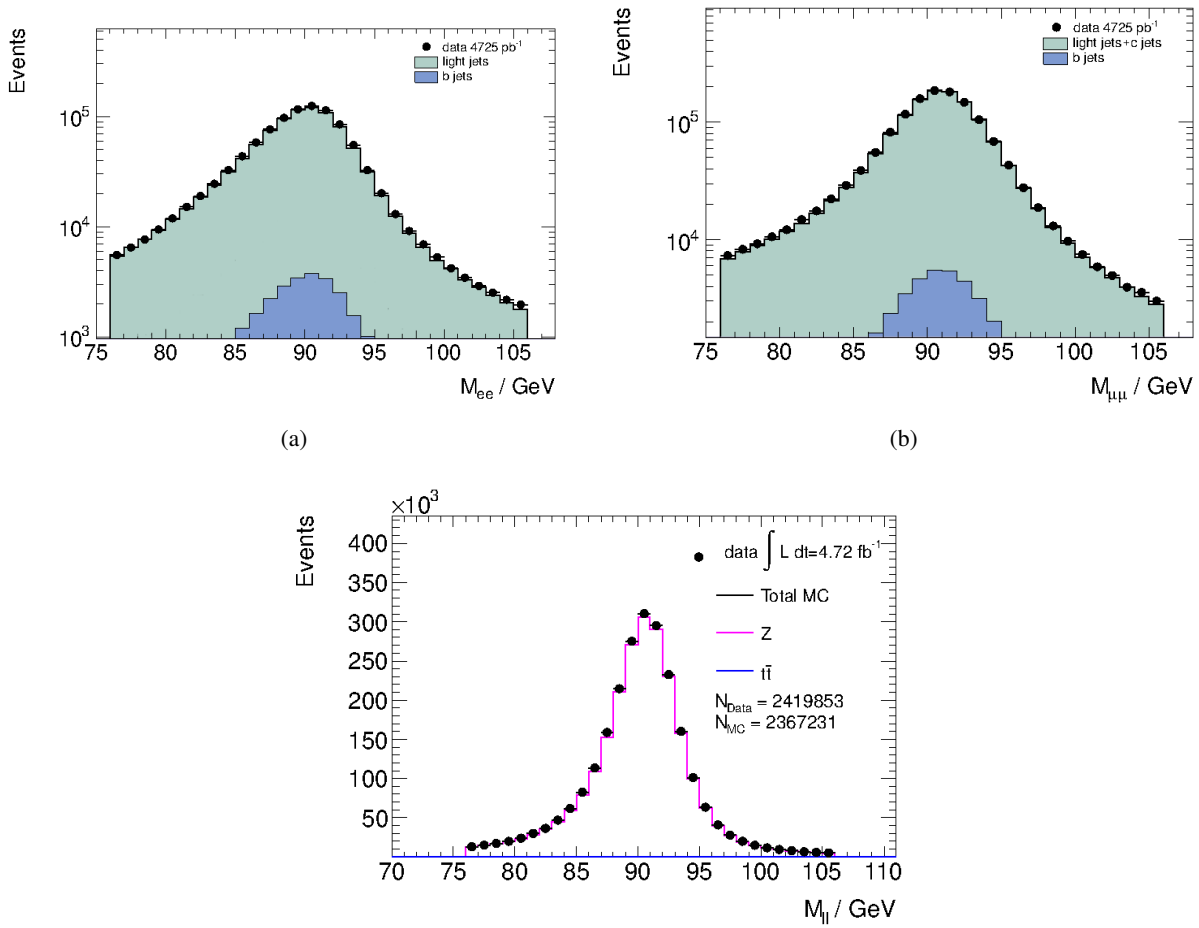

Figure 46: Dilepton invariant mass spectra for (a) combined channels, (b) electron channel, and (c) muon channel

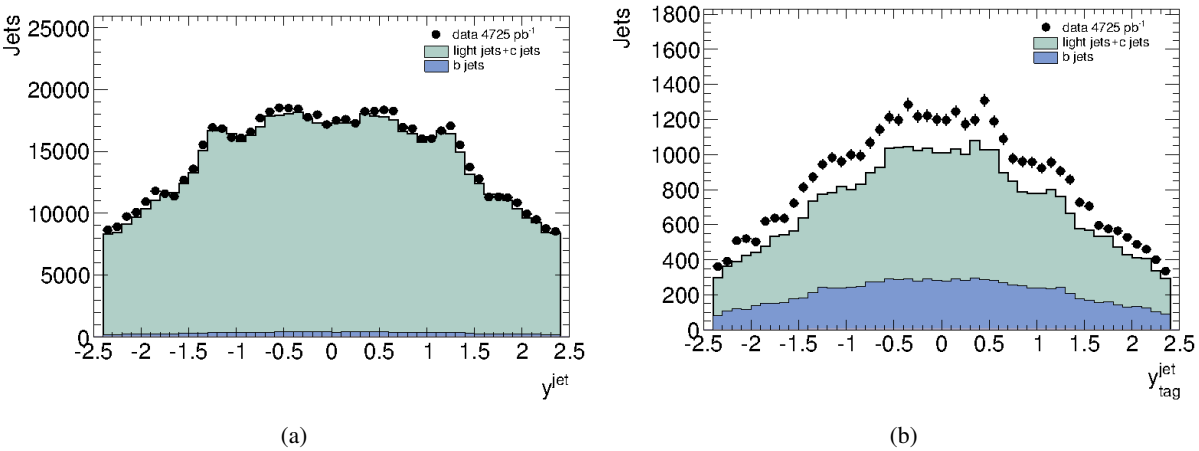

Figure 47: Rapidity distribution for (a) all jets, and (b) jets tagged as b jets with the MV1 algorithm. The difference in normalisation between data and simluation highlights the underestimate of Z + b jet events by the ALPGEN *event generator.*

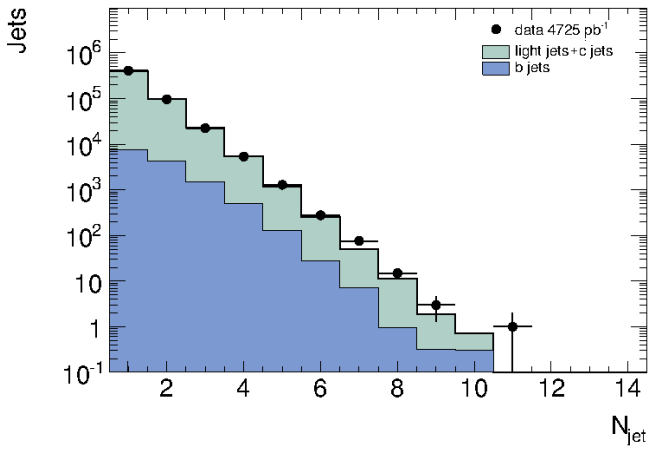

(a)

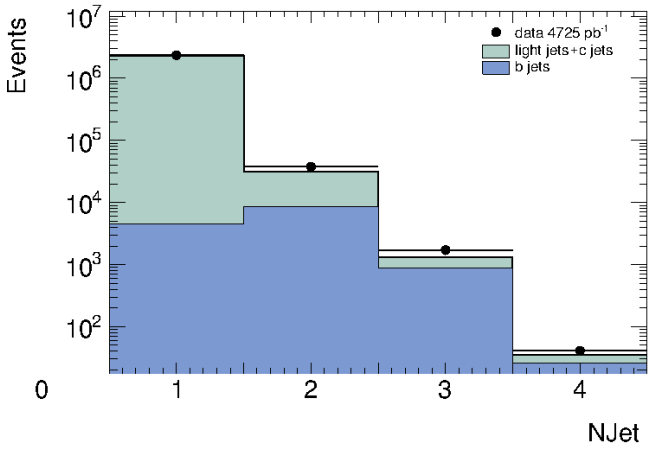

(b)

Figure 48: Control distributions for (a) number of jets, and (b) number of jets tagged as b jets with the MV1 algorithm

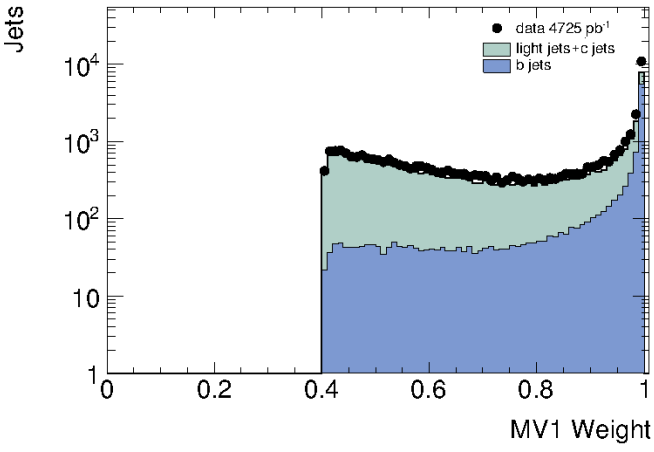

Figure 49: Distribution of the output weight produced by the MV1 neural network b tagging algorithm. Jets are tagged as b jets if $w_{MV1} > 0.404$

7.9.2 Jet Energy Scale (JES)

Another large systematic uncertainty arises from correctly determining the energy of jets. Reconstructed jets are calibrated, as a baseline, to the energy scale measured by the calorimeters, the electromagnetic scale, which is usually established from test-beam measurements for electrons and muons. This energy scale accounts correctly for the energy of photons and electrons, but it does not correct for detector effects such as energy losses in inactive regions and inefficiencies in calorimeter clustering and jet reconstruction. The JES calibration corrects the energy and momentum of the jets measured in the calorimeter. The derivation of the JES calibration and the estimate of its uncertainty are based on the comparison of simulated jets reconstructed from the calorimeter jet constituents with Monte Carlo truth jets built from stable particles excluding muons and neutrinos. The uncertainty on this calibration is calculated by summing in quadrature several components:

- the global JES uncertainty, derived from single-particle response measurements and dijet balance
- flavor composition uncertainty to account for differences between gluon and light quark jets
- flavor response uncertainty
- an additional b jet uncertainty is added to jets that are matched to a b hadron
- close-by jet uncertainty since no requirement on the jet isolation is given

The uncertainty on the jet energy scale is calculated using a tool in ATHENA that is provided by the Jet/Etmiss group. More information on the JES calibration can be found in [98].

7.9.3 Jet Energy Resolution (JER)

It is possible that the jet energy resolution in simulation is mismodelled, and so the p_T of the jets is smeared. To account for a possible underestimate of the jet energy resolution in simulation, an additional smearing is applied to the jets as a function of jet p_T. The resulting change in the cross-section is symmetrised to obtain an estimate of the downward shift in resolution. Details on the JER can be found in [99].

7.9.4 Lepton identification efficiency, energy scale and resolution

The lepton identification efficiencies are applied according to recommendations from the egamma and muon performance groups, obtained with tag-and-probe methods. For both the electron and muon chan-

nels, the efficiency scale factors are varied upwards and downwards by an uncertainty derived as a function of the kinematic properties of the leptons. Additional uncertainties are also applied to the electron and muon momentum scale.

7.9.5 Luminosity

An uncertainty of 1.8% on the delivered luminosity is measured [100].

7.9.6 Backgrounds

The theoretical prediction for the inclusive $t\bar{t}$ production cross section is $\sigma_{t\bar{t}} = 166.8\ ^{+16.5}_{-17.8}$ (stat) (syst) pb [101]. To estimate the impact of this uncertainty on the normalisation, the fit is applied with $\sigma_{t\bar{t}} + \delta\sigma_{t\bar{t}}$ and $\sigma_{t\bar{t}} - \delta\sigma_{t\bar{t}}$. Studies have estimated the uncertainty on the QCD multijet background to be approximately 100% [96], and so to estimate the impact of this uncertainty on the normalisation, the fit is applied with the QCD estimate doubled and with it removed from the background template.

7.9.7 b jet template uncertainty

The event weights applied to simulated events to correct the multiplicities in b hadron decays described in Section 7.5.6 modify the bottom templates of both signal and background from shapes which are known to be poorly modelled to something closer to the expected distribution for b jets in the data. To calculate the uncertainty on this correction, an alternative method for correcting the templates is implemented, and the difference between the alternative and default EVTGEN fits is symmeterised.

7.9.8 Charm fragmentation

The construction of flavour templates from simulated data using the event generator truth information requires the description of light, charm, and bottom quark jets in the simulation to be accurate. The ability to discriminate between charm and bottom jets is particularly important since charm jets are more likely to be mistagged as bottom jets. This requires the modelling of charm jets and the hadronisation in simulation to be well understood. A significant effect that can lead to the distortion of the charm template is the mis-modelling of the meson to baryon hadronisation ratio in HERWIG, which generates the parton shower and thus the hadrons produced in jets. Different hadron types in the charm jet will effect the value of the flavour discriminant $\ln(p_b/p_c)$, which takes as input various jet parameters such as the number of vertices in the jet and the number of tracks in the primary jet vertex. It is known that

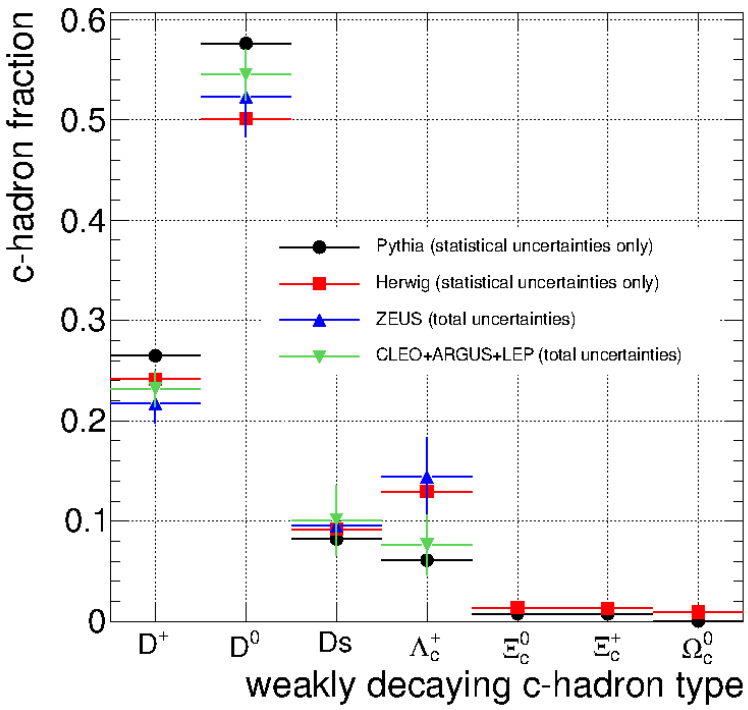

Figure 50: Charm hadron fraction for various event generators compared to experimental measurements.

HERWIG does not accurately reproduce the decay fractions seen in data that have been measured at LEP and ZEUS, whereas other event generators model the meson/baryon ratio more accurately.

To measure the size of this effect, the main contributions to the charm flavour template, which come from the D^0, D^+, D_s mesons, and baryons (mostly Λ_c^+), are reweighted from the HERWIG charm fractions to the PYTHIA charm fractions. Measured values of the charm fractions from real data mostly lie between these two values, as seen in Figure 50, so this reweighting represents a conservative estimate for magnitude of this effect.

Templates for the various charm mesons are built in the following way. Each jet is compared to all truth particles in the Monte Carlo sample and the distance from the jet to the truth particle, dR, is calculated:

$$dR = \sqrt{(\eta_{jet} - \eta_{truth})^2 + (\phi_{jet} - \phi^2_{truth})} \tag{29}$$

The truth particle with a track closest to the axis of the reconstructed jet is chosen as the matched hadron. If it satisfied $dR < 0.3$, distributions of the flavour discriminant value $\ln(p_b/p_c)$ for the associated jet are then produced for the D^0, D^+, D_s mesons and charm baryons. These distributions are then scaled to produce the equivalent charm fractions from PYTHIA. These templates are added to form the total PYTHIA

charm template. At this stage, the light flavour template is added to both the modified PYTHIA charm template and the default HERWIG charm template. The PYTHIA *light + charm* template is then divided by the HERWIG *light + charm* template to produce a ratio distribution that measures the template shape difference between the two generators. The ratio of the two templates is fitted with a linear function. The largest change in template shape is from reweighting the D^0 fraction, and so the linear function obtained from fitting this ratio is applied to the total HERWIG charm template when fitting flavour templates to data to produce an alternative value for the b yield in data. The systematic contribution from the mismodelling of meson and baryon decay fractions in HERWIG is given by the difference between the b yield derived using unmodified HERWIG charm template and the b yield derived using the charm template modified to the PYTHIA decay fractions. Histograms of the various charm templates and template ratios can be found in Appendix D.

7.9.9 Systematic uncertainty summary

The fractional systematic uncertainty from the 7 largest effects described above is shown in bins of the differential variables E_T^{bjet}, y^{bjet} and p_T^Z in Figure 51. The largest uncertainty by a significant amount is that from determining the b tagging efficiency. The second largest effect is due to the jet energy scale uncertainty and resolution. The third largest contribution to the uncertainty comes from the electron and muon efficiencies.

7.10 Integrated $Z + b$ jet measurement

The flavour template fit in Figure 44 produces a scale factor, which is then used to determine the b jet yield in data. The fiducial integrated $Z + b$ jet cross section is then determined using Equation 30.

$$\sigma(Z + b) \cdot \Gamma(Z \to ll) = \frac{n_{b\text{fit}}}{2 \cdot C \cdot \mathcal{L}} \qquad \text{with } ll = \{ \text{ee}, \mu\mu \} \tag{30}$$

where $\mathcal{L}$ is the integrated luminosity and C is defined in Section 7.4.

This jet-level cross-section is measured to be:

$$\sigma^{jet}(Z + bjet) = 5.04 \ \pm 0.17 \text{ stat } \pm 0.83 \text{ syst pb.} \tag{31}$$

The inclusive Z production cross section measured by ATLAS is 0.479 ± 0.003 stat ± 0.005 syst nb [102]. The ratio of the integrated $Z + b$ jet cross section to the inclusive Z production cross section is thus

measured to be:

$$\frac{\sigma^{jet}(Z + bjet)}{\sigma(Z)} = (5.26 \ \pm 0.18 \text{ stat } \pm 0.89 \text{ syst}) \times 10^{-3}. \quad (32)$$

7.11 Differential $Z + b$ jet measurements

An example of the flavour template fit produced to measure the differential $Z + b$ jet cross section in bins of E_T^{bjet}, y^{bjet} and p_T^Z is shown in Figure 52. The full set of fitted flavour templates for the E_T^{bjet} differential measurement are shown in Appendix C. The differential b jet yields produced from the extended likelihood fits to the flavour templates for electron and muon channels are shown in Figure 53.

The fiducial cross section for the $Z + b$ inclusive measurement is determined using Equation 30. The fiducial $Z + b$ jet cross sections in bins of the differential variables E_T^{bjet}, y^{bjet} and p_T^Z are shown, with systematic uncertainties, in Figure 54.

7.12 MCFM prediction

The MCFM theoretical predictions for the fiducial cross-sections presented in Figure 54 use five-flavour CT10 PDF's. MCFM performs parton level peturbative QCD calculations producing final states with partons clustered into jets, which allows the implementation of the kinematic requirements defining the fiducial signal [97]. Leptons and jets must satisfy p_T >20 GeV and $|\eta|$ <2.5, $|y| < 2.4$ respectively, and the dilepton invariant mass window is $76 < m_{ll}$ <106 GeV. The same lepton-jet overlap removal and b hadron matching criteria defined by the particle level selection in Section 7.4 is implemented.

To obtain a full prediction, the results from several sub-processes must be combined. The $Z + b$ cross-section prediction at NLO requires the calculation of final states with one b jet, with two b jets and one of them not in the acceptance or both b quarks merged into one jet by the jet finding algorithm, and with two or more b jets in the acceptance. The renormalisation and factorisation scales are set as the sum in quadrature of the Z boson mass and p_T on an event by event basis.

The uncertainty on the MCFM prediction arises from the choice of the scales used in the calculation, the uncertainty on α_s, and the experimental errors on the PDF input measurements. The dependence on the choice of renormalisation and factorisation scales is estimated by shifting the scales up and down independently by a factor of 2. The calculation is repeated by changing the value of α_s plus and minus one standard deviation both for the matrix element and the PDF set. The uncertainty due to experimental contraints on the PDF set is estimated using the recommended procedure [96].

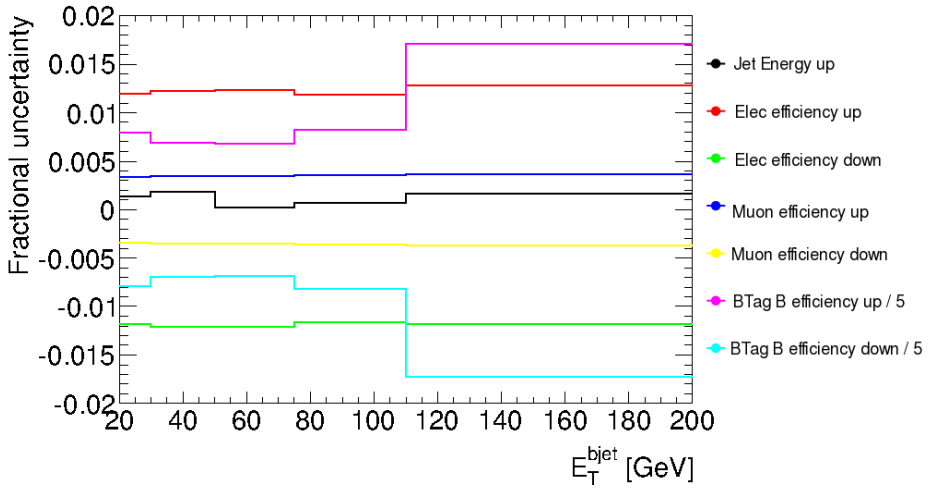

(a)

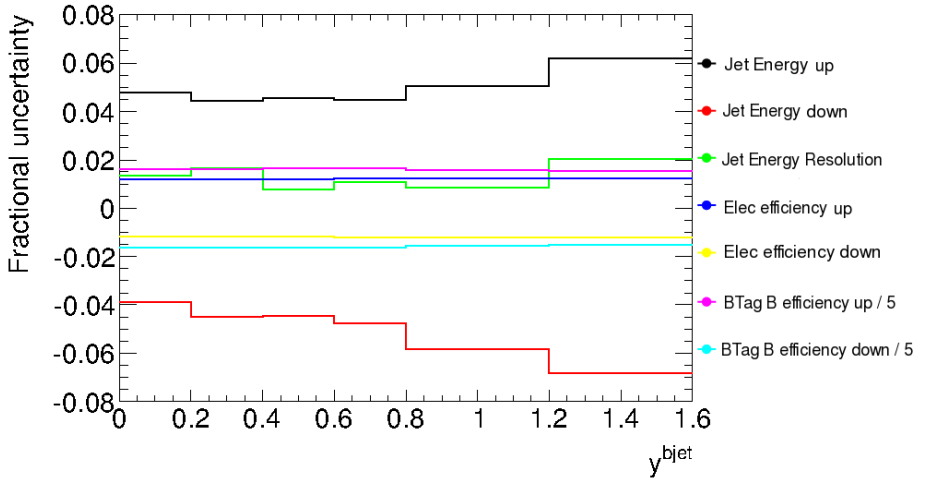

(b)

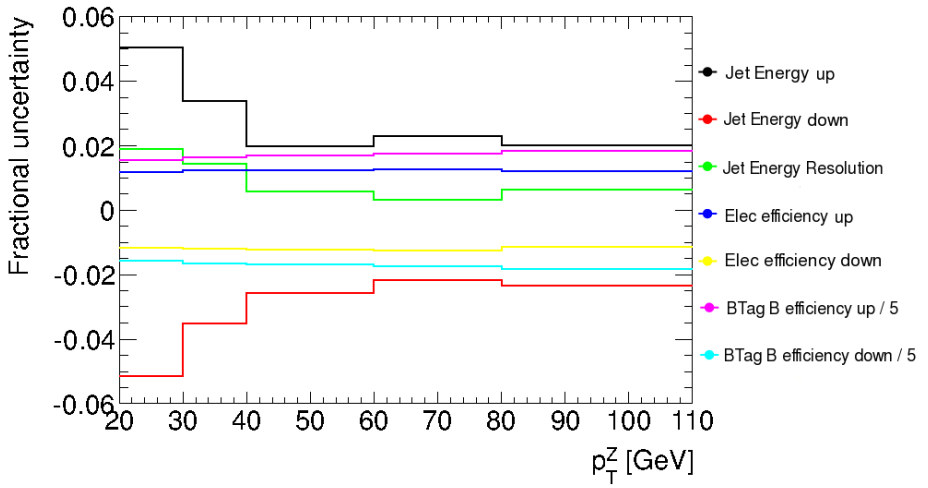

(c)

Figure 51: Relative uncertainty of the 7 largest systematic effects in bins of (a) E_T^{bjet}, (b) y^{bjet} and (c) p_T^Z. The uncertainty on the b tagging efficiency is the dominant contribution.

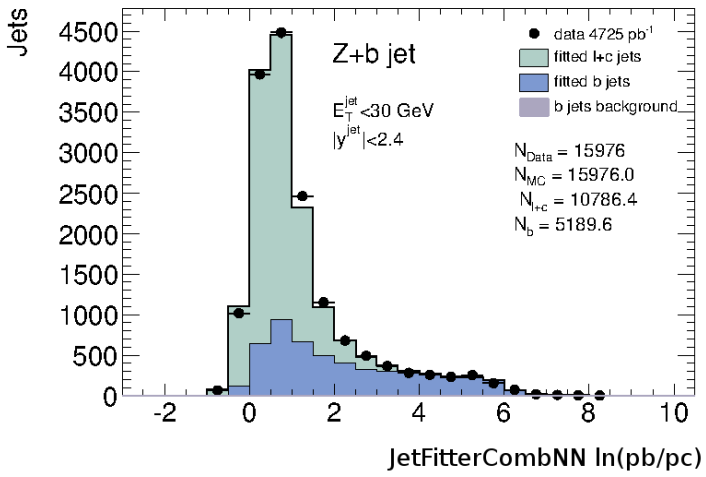

(a)

Figure 52: The fitted flavour discriminant distribution in data and MC for the differential bin 20 GeV < $E_T^{b\,jet}$ < 40 GeV.

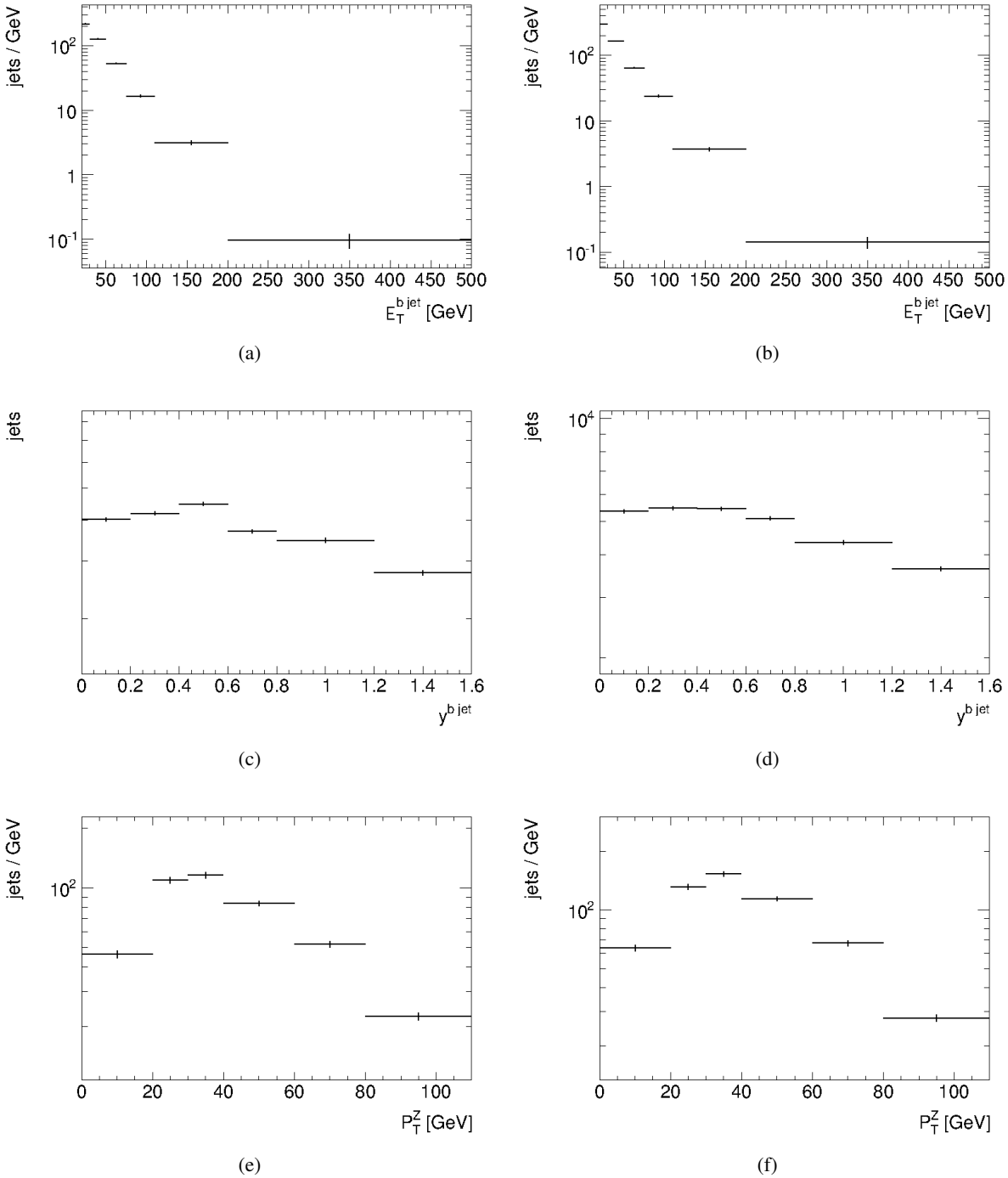

Figure 53: b jet yield produced by the extended likelihood fits to flavour templates for electron (left column) and muon (right column) channels in bins of (a) - (b) E_T^{bjet}, (c) - (d) y^{bjet} and (e) - (f) p_T^Z

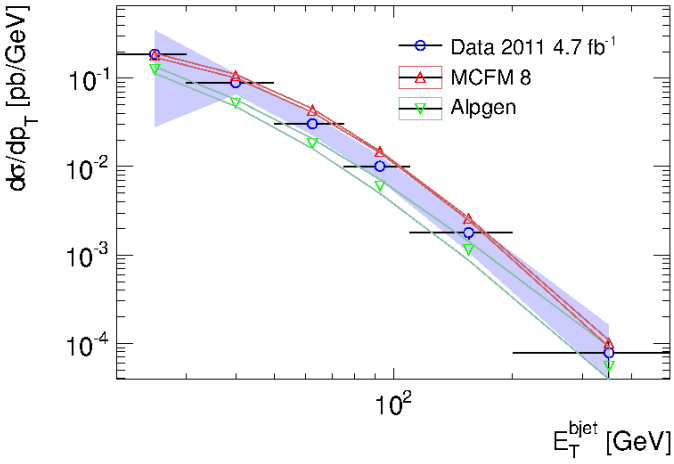

(a)

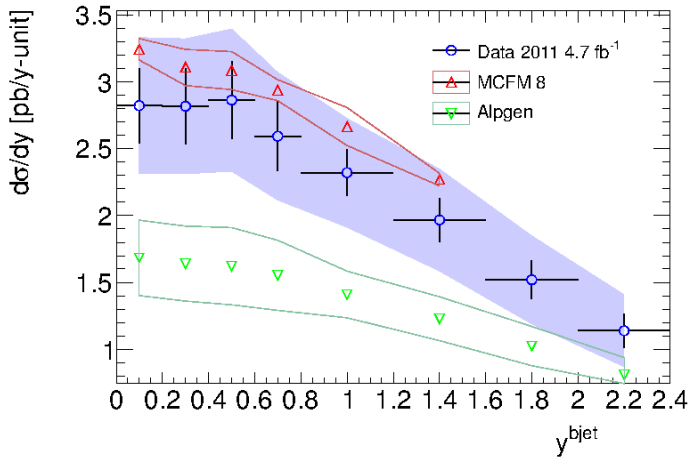

(b)

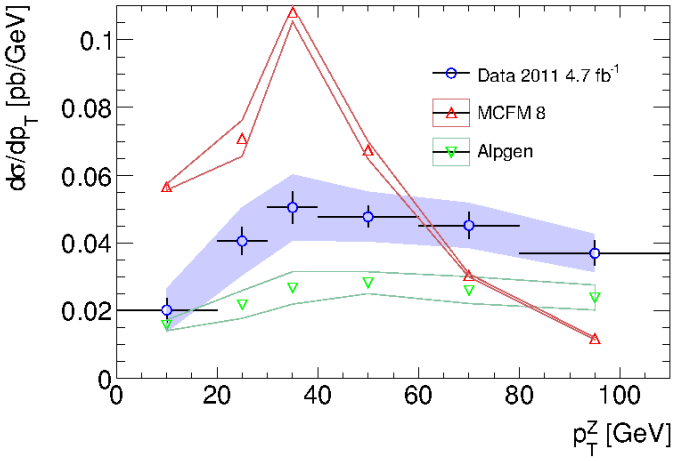

(c)

Figure 54: Fiducial Z + b jet cross-sections in bins of (a) E_T^{bjet}, (b) y^{bjet}, and (c) P_T^Z for 2011 ATLAS data, and for MCFM8 *and* ALPGEN *models. The total systematic uncertainty in data is shown by the purple band. Theoretical uncertainties are shown by the red and green bands for* MCFM8 *and* ALPGEN *respectively.*

7.13 Comparison of data and theory

Current theoretical models require renormalisation and factorisation scales to be chosen and use empirical data with various parameter tunings to estimate the parton distribution functions in order to calculate cross-sections involving b quark production. The comparison of the cross-section measurement for associated production of a Z boson with one or more b jets, shown in Figure 54, made using data recorded by the ATLAS detector in 2011, with the MCFM predictions show that they agree within uncertainties. This suggests that the choice of scales and the PDF sets used for the MCFM prediction describe the data reasonably well. There is, however, an unusual shape to the MCFM prediction for the cross-section differential in p_T^Z, which is currently under investigation. The ALPGEN prediction, however, does not agree as well with data. This could be a result of mismodelling of various event and jet properties by ALPGEN + HERWIG that have a significant effect on the b tagging. The improved agreement between data and MCFM may also result from the inclusion of the b quark into the PDFs and the additional calculation of the leading order subprocesses shown by the top two Feynman diagrams in Figure 5 by the variable flavour scheme used by MCFM. As can be seen in the systematic contributions shown in Figure 54, the precision of the measurement would benefit significantly from reduced uncertainties arising from the b tagging calibration. The work presented in Chapter 6 continues to be updated with the intention of reducing the systematic contribution from the b tagging algorithms, and thus improve the precision of measurements involving b quark jets. For this analysis, only a single set of theoretical cross-sections generated by MCFM were calculated with the factorisation and renormalisation scales equal to the sum in quadrature of the Z boson mass and p_T, thus a scale comparison was not available for 2011 data. It is proposed that for the Z + b jets cross-section measurement with 2012 data, a broader range of theoretical predictions are produced to allow scale comparison.

Chapter 8

Summary

The ATLAS Experiment has so far been highly successful in making a large range of physics measurements. Much work in the first two years involved commissioning and calibration, with extensive efforts to provide the software infrastructure and grid processing facilities to perform physics analysis. In Chapter 5, contributions made to the commissioning of the inner detector by measuring the detector resolution are shown. These studies were used for commissioning the early heavy flavour tagging algorithms. The calibration of these tagging algorithms is studied in Chapter 6, where systematic effects introduced at detector level that lead to different tagging efficiencies in data and simulation are measured. This understanding of b quark identification was utilized in the cross-section measurement for the production of a Z boson in association with b jets in Chapter 7, and comparisons of these measurements with theoretical predictions are shown.

The work detailed in this thesis has been completed for the main purpose of obtaining an improved theoretical description of the properties and interactions of b quarks mediated via the strong nuclear force. The complexity of such an analysis, including the correction of event and particle properties reconstructed by software algorithms, and the correction of event generator parameters in simulation, requires that the causes of differences between data and simulation be thoroughly investigated. Discrepancies between data and theoretical prediction can result from a large range of phenomena, so developing the physics analysis further and improving the tuning of theorectical models will lead to better agreement between data and simulation.

The ATLAS experiment will continue to record collision data for many more years, and its international collaboration of scientists will perform extensive analyses to improve the accuracy of measurements and develop further the theoretical models and predictions. As the experience of these scientists with the ATLAS detector and the software environment used for analysis continues to grow, the efficiency of making such measurements will improve.

This endeavour will no doubt contribute significantly to our understanding of sub-atomic matter and the nature of physical reality for years to come, and will hopefully bring us closer to piecing back together the puzzle of our own existence.

References

[1] "The Bhagavad-Gita", translated by Sir Edwin Arnold, Vol. XLV, Part 4. The Harvard Classics. New York: P.F. Collier & Son, 190914; Bartleby.com, 2001

[2] Lucretius Carus, Titus, 94 BC - 49 BC, "On the Nature of Things", EBook-No. 785. http://www.gutenberg.org/ebooks/785

[3] J. Gogarty, 2012. Founder of www.iheartmandalas.com. http://mandala-jim.deviantart.com/ - Used with permission (December 2013)

[4] D. Galbraith, C. Bugard, http://davidgalbraith.org/portfolio/ux-standard-model-of-the-standard-model/ (2012)

[5] S. Glashow, "Partial symmetries of weak interactions", Nucl. Phys. 22 p4 (1961).

[6] P. Higgs, "Broken Symmetries and the Masses of Gauge Bosons", Phys. Rev. Lett. 13 p16 (1964).

[7] G. Sterman, "An Introduction to Quantum Field Theory", 1st ed, Cambridge University Press (1993).

[8] S. Weinberg, "A Model of Leptons", Phys. Rev. Lett. 19, p12641266 (1967).

[9] UA1 Collaboration, "Experimental observation of lepton pairs of invariant mass around 95 GeV/c^2 at the CERN SPS collider", Phys. Lett. B 126 5, (1983).

[10] UA1 Collaboration, "Experimental observations of isolated large E_T electrons with associated missing energy at $\sqrt{s}$=540 GeV", Phys. Lett. B, 122 1 p24 (1983).

[11] M. L. Perl et al., "Evidence for Anomalous Lepton Production in e^+e Annihilation", Phys. Rev. Lett. 35 p22 (1975).

[12] K. Kodama et al. (DONUT Collaboration), "Observation of tau neutrino interactions", Phys. Lett. B 504 p3 (2001).

[13] M. Gell-Mann, "A Schematic Model of Baryons and Mesons", Phys. Lett. 8 (1964) .

[14] G. Zweig, “An SU(3) model for strong interaction symmetry and its breaking”, CERN reports 8419/TH.401 and 8419/TH.412 (1964).

[15] E.D. Bloom et al., “High-Energy Inelastic ep Scattering at 6 and 10”, Phys. Rev. Lett. 23 p16 (1969).

[16] Fritzsch, Harald, and Gell-Mann, “Current algebra: Quarks and what else?”, eConf C720906V2 (1972) 135-165 hep-ph/0208010.

[17] J. -E. Augustin et al., “Discovery of a Narrow Resonance in e+e- Annihilation”, Phys. Rev. Lett. 33, p14061408 (1974).

[18] S.W. Herb et al.,“Observation of a Dimuon Resonance at 9.5 GeV in 400-GeV Proton-Nucleus Collisions”, Phys. Rev. Lett. 39 p5 (1977).

[19] F. Abe et al. (CDF), “Observation of Top Quark Production in pp Collisions with CDF at Fermilab”, Phys. Rev. Lett. 74 p14 (1995).

[20] ATLAS Collaboration, “Observation of a new particle in the search for the Standard Model Higgs boson with the ATLAS detector at the LHC”, Phys. Lett. B p716 (2012).

[21] ATLAS Collaboration, “Evidence for the spin-0 nature of the Higgs boson using ATLAS data”, Phys. Lett. B 726, pp. 120-144 (2013).

[22] J.C. Collins and D.E. Soper, “Theorems of perturbative QCD”, Ann. Rev. Nucl. Part. Sci. 37 p383 (1987).

[23] Lipatov, L.N., “The parton model and perturbation theory”, Sov.J.Nucl.Phys. 20 p94-102 (1975), Yad.Fiz. 20 p181-198 (1974).

[24] Quantum Diaries, “When Feynman Diagrams Fail”, http://www.quantumdiaries.org/2010/12/11/when-feynman-diagrams-fail/ (2010).

[25] J.M. Campbell, J.W. Huston, W.J. Stirling, “Hard Interactions of Quarks and Gluons: a Primer for LHC Physics”, Rept. Prog. Phys. 70 p89 (2007).

[26] B. Andersson et al., “Parton Fragmentation and String Dynamics”, Phys. Rept. 97 (1983).

[27] B. Webber, "A QCD Model for Jet Fragmentation Including Soft Gluon Interference", Nucl. Phys. B 238 p492 (1984).

[28] ATLAS Collaboration, " Measurement of the cross-section for b-jets produced in association with a Z boson at $\sqrt{s}$ = 7 TeV with the ATLAS detector", CERN-PH-EP-2011-133 (2011).

[29] CDF Collaboration, "Measurement of Cross Sections for b Jet Production in Events with a Z Boson in pp Collisions at $\sqrt{s}$ = 1.96 TeV", Phys. Rev. D79:052008 (2009).

[30] J M Campbell, R. K. Ellis, "MCFM for the Tevatron and the LHC", Nucl. Phys. Proc. Suppl. 205-206 p10-15 (2010).

[31] L. Evans, P. Bryant, "LHC Machine", JINST-3-S08001 (2008).

[32] "Taking a closer look at the LHC", http://www.lhc-closer.es/php/index.php?i=1&s=4&p=6&e=2 (September 2012).

[33] http://belezadafisica.blogspot.co.uk/2011/09/como-e-o-processo-de-acelerar.html.

[34] ATLAS Collaboration, "The ATLAS Experiment at the CERN Large Hadron Collider", JINST-3-S08003 (2008).

[35] CMS Collaboration, "The CMS experiment at the CERN LHC", JINST-3-S08004 (2008).

[36] LHCb Collaboration, "The LHCb Detector at the LHC", JINST-3-S08005 (2008).

[37] "The ALICE experiment at the CERN LHC", JINST-3-S08002 (2008).

[38] ATLAS Collaboration, "ATLAS Detector and Physics Performance: Technical Design Report", CERN-LHCC-97-16 (1997).

[39] F. Lemeilleur, G. Lindstrom, and S. Watts. "Third RD48 status report", CERN-LHCC-2000-009 (2000).

[40] ATLAS Collaboration, "Alignment of the ATLAS Inner Detector Tracking System", ATL-INDET-PROC-2011-021 (2011).

[41] ATLAS Collaboration, “ATLAS pixel detector electronics and sensors”, JINST 3 P07007 (2008).

[42] M. Mikuz, “The ATLAS SemiConductor Tracker”, Nuclear Science Symposium Conference Record, IEEE (2003).

[43] The ATLAS TRT collaboration et al., “The ATLAS Transition Radiation Tracker (TRT) proportional drift tube: design and performance”, JINST 3 P02013 (2008).

[44] ATLAS Collaboration. “ATLAS liquid-argon calorimeter: Technical Design Report”, CERN-LHCC-96-041 (1996).

[45] J. Colas et al. “Position resolution and particle identification with the ATLAS EM calorimeter”, Nucl. Instrum. Meth., A550 p96115 (2005).

[46] P. Adragna et. al, “The ATLAS Hadronic Tile Calorimeter: From Construction Toward Physics”, IEEE Transactions On Nuclear Science 53 3 (2006).

[47] ATLAS Collabortation (G. Aad et. al), “The ATLAS Experiment at the CERN Large Hadron Collider”, JINST 3 S08003 (2008).

[48] ATLAS Collaboration, “ATLAS muon spectrometer: Technical Design Report”, CERN-LHCC-97-022 (1997).

[49] C. Padilla, “The ATLAS Trigger System”, IEEE Transactions On Nuclear Science 57 2 (2010).

[50] ATLAS Collaboration, “ATLAS Computing Technical Design Report”, ATLAS TDR, CERN-LHCC-2005-022 (2005).

[51] D. Costanzo et al., “The Geant4-Based Simulation Software of the ATLAS Detector”, Nuclear Science Symposium Conference Record, IEEE, Volume 1 (2006).

[52] J. Allison et al., “Geant4 developments and applications”, IEEE Transactions on Nuclear Science 53 1 (2006).

[53] T. Cornelissen et al., “Concepts, Design and Implementation of the ATLAS New Tracking (NEWT)”, ATL-SOFT-PUB-2007-007 (2007).

[54] D. Wicke, "A New Algorithm For Solving Track Ambiguities", DELPHI 98-163, PROG 236 TRACK 92 (1998).

[55] E. Bouhova-Thacker et al., "Vertex Reconstruction in the ATLAS Experiment at the LHC", ATL-COM-INDET-2009-011 (2009).

[56] M Tibbets, "Tracking, vertexing and b-tagging performance in ATLAS", ATL-PHYS-PROC-2012-307 (2012).

[57] O. Arnaez, "Electron Reconstruction and Identification with the ATLAS Detector", ATL-PHYS-PROC-2009-118 (2009).

[58] ATLAS Collaboration, "Reconstruction and identification of electrons in ATLAS", SMU-HEP-08-21 (2008).

[59] ATLAS Collaboration, "Electron efficiency measurements in early 2012", ATL-COM-PHYS-2012-783 (2012).

[60] ATLAS Collaboration, "Electron performance measurements with the ATLAS detector using the 2010 LHC proton-proton collision data", Eur. Phys. J. C72 p1909 (2012).

[61] S. Hassani et al. "A Muon Identification and Combined Reconstruction Procedure for the ATLAS Detector at the LHC Using the (MUONBOY, STACO, MuTag) Reconstruction Packages", Nucl. Instr. Meth. A 572 p7779 (2007).

[62] ATLAS Collaboration, "Muons in the Calorimeters: Energy Loss Corrections and Muon Tagging", CERNOPEN-2008-020 (2009).

[63] ATLAS Collaboration, "A measurement of the muon reconstruction efficiency in 2010 ATLAS data using J/ψ decays", ATLAS-CONF-2012-125 (2012).

[64] M. Cacciari, G. P. Salam, and G. Soyez, "The anti-k(t) jet clustering algorithm", JHEP 04 063 (2008).

[65] G. Aad et al., "The ATLAS Experiment at the CERN Large Hadron Collider", JINST 3 S08003 (2008).

[66] ATLAS Collaboration, "Expected performance of the ATLAS Detector, Trigger and Physics", CERNOPEN-2008-020 (2009).

[67] ATLAS Collaboration, "Reconstruction and Calibration of Missing Transverse Energy and Performance in Z and W events in ATLAS Proton-Proton Collisions at $\sqrt{s}$ = 7 TeV, ATLAS-CONF-2011-080 (2011).

[68] The ATLAS collaboration, "Performance of the ATLAS Secondary Vertex b-tagging Algorithm in 7 TeV Collision Data", ATLAS-CONF-2010-042 (2010).

[69] G. Piacquadio, C. Weiser, "A new inclusive secondary vertex algorithm for b-jet tagging in ATLAS", J.Phys.Conf.Ser. 119 032032 (2008).

[70] The ATLAS collaboration, "Commissioning of the ATLAS high-performance b-tagging algorithms in the 7 TeV collision data", ATLAS-CONF-2011-102 (2011).

[71] S. Aoun, et al., "Calibration of b-Jet Tagging Efficiency using the p_T^{rel} Method", ATL-COM-PHYS-2011-043 (2011).

[72] Aad, G. et al., "b-tagging calibration in ttbar final states and ttbar cross-section measurements with ATLAS data at sqrt(s)=7 TeV", ATL-COM-PHYS-2011-048 (2011).

[73] Aad, G. et al., "b-tagging calibration with D*mu reconstructed in 7 TeV collisions with ATLAS", ATL-COM-PHYS-2011-051 (2011).

[74] Aad, G. et al., "b-Jet Tagging Efficiency Calibration 1 using the System8 Method", ATL-COM-PHYS-2011-033 (2011).

[75] G.Cortiana, "Alignment of the ATLAS Inner Detector tracking system", ATLAS Tracking Workshop, CERN (2009).

[76] ATLAS Collaboration, "Tracking studies for b-tagging with 900 GeV collision data with the ATLAS detector", ATLAS-CONF-2010-003 (2010).

[77] C. Amsler et al. (Particle Data Group), Section 27.3.: "Multiple scattering through small angles.", Physics Letters B667 1 (2008).

[78] D.Grandjean, G.Gaycken, "Impact Parameter Resolution Studies", ECFA Workshop Durham (2004).

[79] ATLAS Collaboration, "Calibrating the b-Tag Efficiency and Mistag Rate of the SV0 b-Tagging Algorithm in 3 pb1 of Data with the ATLAS Detector", ATLAS-CONF-2010-099 (2010).

[80] T. Sjostrand, S. Mrenna, and P. Z. Skands, "PYTHIA 6.4 Physics and Manual", JHEP 05 026 (2006).

[81] A. D.Martin, W. J. Stirling, R. S. Thorne, and G.Watt, "Parton distributions for the LHC", Eur. Phys. J. C63 189, arXiv:hep-ph/0901.0002 (2009).

[82] A. Sherstnev and R. S. Thorne, "Different PDF approximations useful for LO Monte Carlo generators", arXiv:hep-ph/0807.2132.

[83] T. Carli and A. Schwarzman, "Jet energy measurement with the ATLAS detector in proton-proton collisions at $\sqrt(s)$ = 7 TeV taken in 2010", ATL-COM-PHYS-2011-978 (2010).

[84] ATLAS Collaboration, "Performance of the ATLAS Secondary Vertex b-tagging Algorithm in 7 TeV Collision Data", ATLAS-CONF-2010-042 (2010).

[85] ATLAS Collaboration, "Tracking Studies for b-tagging with 7 TeV Collision Data with the ATLAS Detector", ATLAS-CONF-2010-070 (2010).

[86] ATLAS Collaboration, "Jet energy scale and its systematic uncertainty in proton-proton collisions at sqrt(s)=7 TeV in ATLAS 2010 data", ATLAS-CONF-2011-032 (2011).

[87] Aad, G. et al., "Track Reconstruction Efficiency in sqrt(s)=7 TeV Data for Tracks with p_T > 100 MeV", ATL-COM-PHYS-2010-363 (2010).

[88] ATLAS Collaboration, "Proposal and Motivations for 2011 Trigger Menu", ATL-COM-DAQ-2011-007 (2011).

[89] M.Bahr et al., "Herwig++ Physics and Manual", Eur.Phys.J.C58:639-707, (2008).

[90] M.Mangano et al., "ALPGEN, a generator for hard multiparton processes in hadronic collisions", JHEP 0307 001 (2003).

[91] http://jimmy.hepforge.org/ (September 2013).

[92] S. Frixione et al., "The MC NLO 4.0 Event Generator", CERN-TH2010-216 (2010).

[93] M. Sanders, "Heavy Flavour Overlap Removal for Alpgen Pythia/Herwig Samples", presentation given at ATLAS MC NLO/Multileg Mini-Workshop, $http://indico.cern.ch/getFile.py/access?resId=0\&materialId=slides\&contribId=0\&sessionId=0\&subContId=0\&confId=197546$, (2012).

[94] ATLAS Collaboration, "Muon Momentum Resolution in First Pass Reconstruction of pp Collision Data Recorded by ATLAS in 2010", ATLAS-CONF-2011-046 (2011).

[95] ATLAS Collaboration, "Calibrating the b-Tag Efficiency and Mistag Rate in 35 pb^{-1} of Data with the ATLAS Detector", ATLAS-CONF-2011-089 (2011).

[96] ATLAS Collaboration, "Measurement of the Zb and $Z\bar{b}b$ cross sections with 4.6 fb^1 of 7 TeV ATLAS data", ATLAS-NOTE (forthcoming Winter 2014).

[97] J. Campbell et al., "MCFM v6.6 A Monte Carlo for FeMtobarn processes at Hadron Colliders Users Guide", $http://mcfm.fnal.gov/mcfm.pdf$ (April 2013).

[98] ATLAS Collaboration, "Jet energy scale and its systematic uncertainty for jets produced in proton-proton collisions at $\sqrt(s) = 7$ TeV and measured with the ATLAS detector", ATLAS-CONF-2010-056 (2010).

[99] ATLAS Collaboration, "Jet energy resolution and selection efficiency relative to track jets from in-situ techniques with the ATLAS Detector Using Proton-Proton Collisions at a Center of Mass Energy sqrts = 7 TeV", ATLAS-CONF-2010-054 (2010).

[100] ATLAS Collaboration, "Improved Luminosity Determination in pp Collisions at s = 7 TeV using the ATLAS Detector at the LHC", ATLAS-CONF-2012-080 (2012).

[101] M. Cacciari, M. Czakon, M. Mangano, A. Mitov, and P. Nason, "Top-pair production at hadron colliders with next-to-next-to-leading logarithmic soft-gluon resummation", Phys.Lett. B710 612622 (2012).

[102] ATLAS Collaboration, "Measurement of the inclusive W and Z cross sections in the e and μ decay channels in pp collisions at $\sqrt(s) = 7$ with the ATLAS detector", Phys. Rev. D85, 072004 (2012).

A Efficiency systematic measurements

Effect	$20 < p_T < 40$ GeV	$40 < p_T < 60$ GeV	$60 < p_T < 90$ GeV	$90 < p_T < 140$ GeV	All p_T
Ratio	$\sigma(\epsilon_b)/\epsilon_b\sigma(R_l)/R_l$	$\sigma(\epsilon_b)/\epsilon_b\sigma(R_l)/R_l$	$\sigma(\epsilon_b)/\epsilon_b\sigma(R_l)/R_l$	$\sigma(\epsilon_b)/\epsilon_b\sigma(R_l)/R_l$	ϵ_b/ϵ_c
d_0 smear	-3.6% -21.5%	+1.4% -23.9%	+1.5% -25.2%	+0.1% -29.9%	5.7+-0.3
z_0 smear	-0.1% -1.0%	+0.2% +0.5%	+0.2% -0.7%	-0.0% -0.2%	6.2+-0.0
shared hits	-2.7% +8.6%	-2.8% +19.5%	-4.9% +28.6%	-6.4% +45.5%	6.3+-0.1
jet axis smear	-2.9% +7.5%	-1.1% -0.7%	-0.9% +0.7%	-1.0% -1.1%	6.0+-0.1
JES - 4%	+6.1% -9.5%	-10.5% +3.2%	+3.2% -6.5%	-0.7% -6.0%	5.4+-0.2
JES + 4%	-4.7% +7.4%	+3.7% -0.6%	-0.6% +1.8%	-2.5% +10.0%	5.9+-0.3

Table 13: Breakdown of systematic effects for the b tagging efficiency in simulation as a function of b jet p_T, where ϵ_b and ϵ_c are the bottom and charm tagging efficiencies respectively.

B Software package versions

Versions of the common packages and standard ATLAS tools used to apply corrections, scale factors and event reweighting to Monte Carlo simulation for MC11c and 2011 data for the $Z + b$ jets cross-section measurement are shown in Table 14.

Purpose	Package - Version
Muon Trigger Recommendations 2011	TrigMuonEfficiency-00-02-32
Muon Efficiency Correction	MuonEfficiencyCorrections-02-01-12
Muon Momentum Corrections	MuonMomentumCorrections-00-08-07
Electron Corrections	egammaAnalysisUtils-00-04-17
Electron Efficiency Correction	ElectronEfficiencyCorrection-00-00-13
Pileup Reweighting	PileupReweighting-00-02-09
Jet Calibration	ApplyJetCalibration-00-02-07
JES Uncertainty Provider	JetUncertainties-00-08-05
JER Provider	JetResolution-01-00-00
Advanced B-tagger	JetTagAlgorithms-00-00-01
B-tag Calibration Interface	CalibrationDataInterface-00-01-02
MET Utility	MissingETUtility-01-01-04-01

Table 14: Versions used of common packages for obtaining scale factors and event reweighting prescriptions, as far as these need to be applied at the analysis stage.

C $Z + b$ differential template fits

Shown in Figure 55 are the extended likelihood fits of flavour templates from simulation to 2011 ATLAS data, differential in E_T^{bjet}, used to measure the jet-level fiducial differential cross-section. Similar sets of fits were produced for measurements differential in y^{bjet} and p_T^Z.

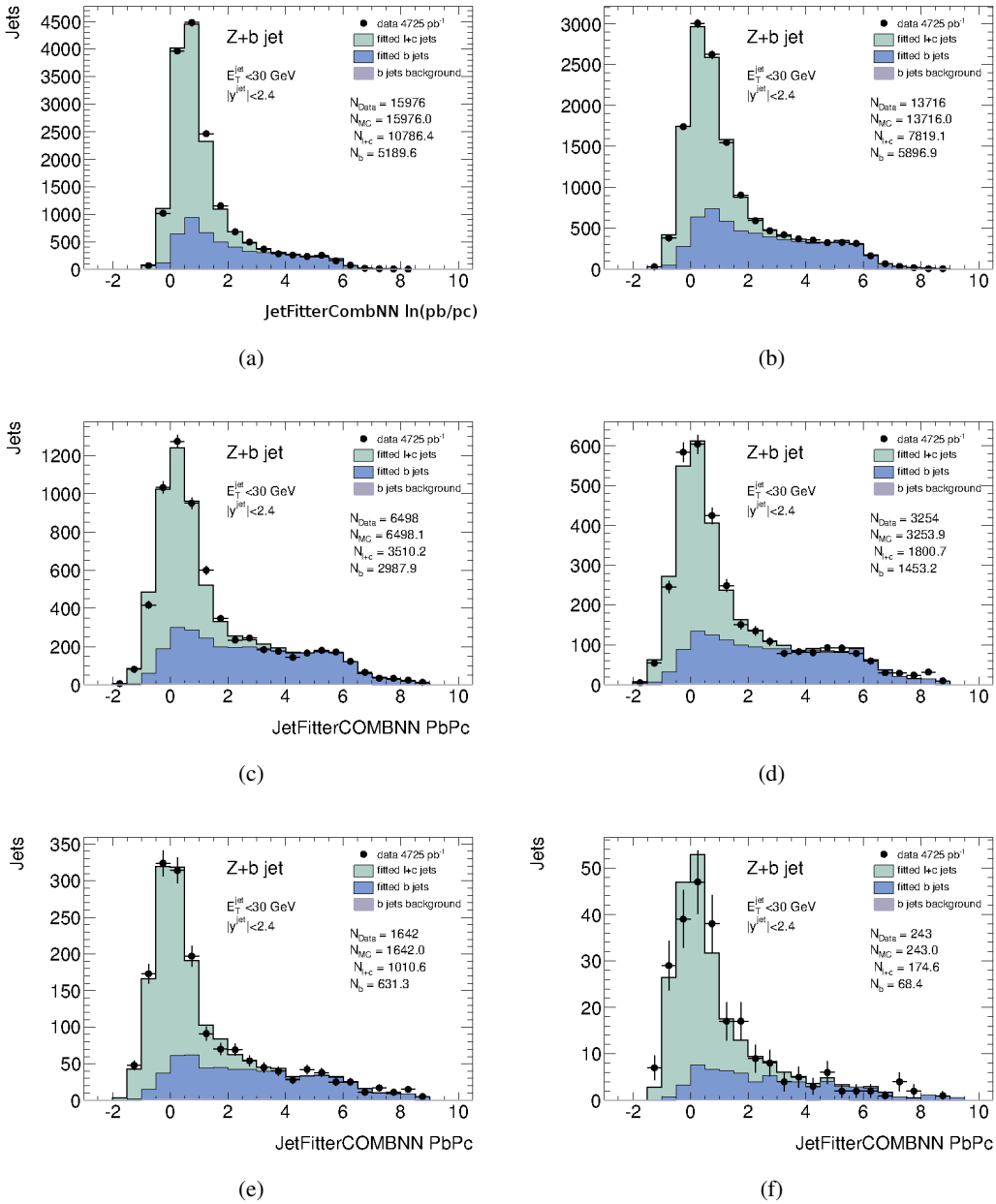

Figure 55: Extended likelihood fits of flavour templates derived from simulation to 2011 ATLAS data, differential E_T^{bjet} for (a) 20-30 GeV, (b) 30-50 GeV, (c) 50-75 GeV, (d) 75-110 GeV, (e) 110-200 GeV, and (f) 200-500 GeV.

D Charm flavour templates

Shown here are the various charm templates and template ratios that were used to estimate the systematic uncertainty on flavour template fits resulting from the mismodelling of the charm decay fractions by the HERWIG event generator.

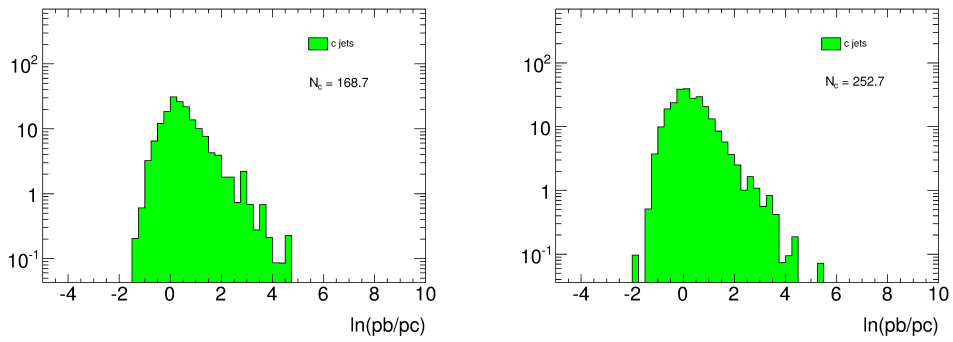

Figure 56: $ln(p_b/p_c)$ template distribution for (a) D^+, (b) D^0, (c) D_s mesons and (d) charm baryons.

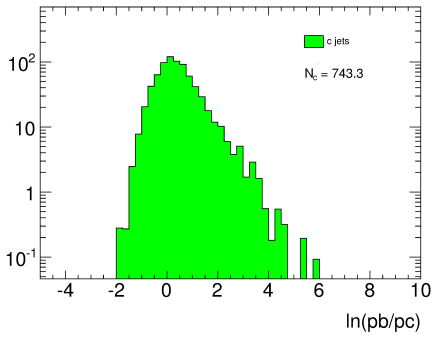

Figure 57: $ln(p_b/p_c)$ template for all charm hadrons

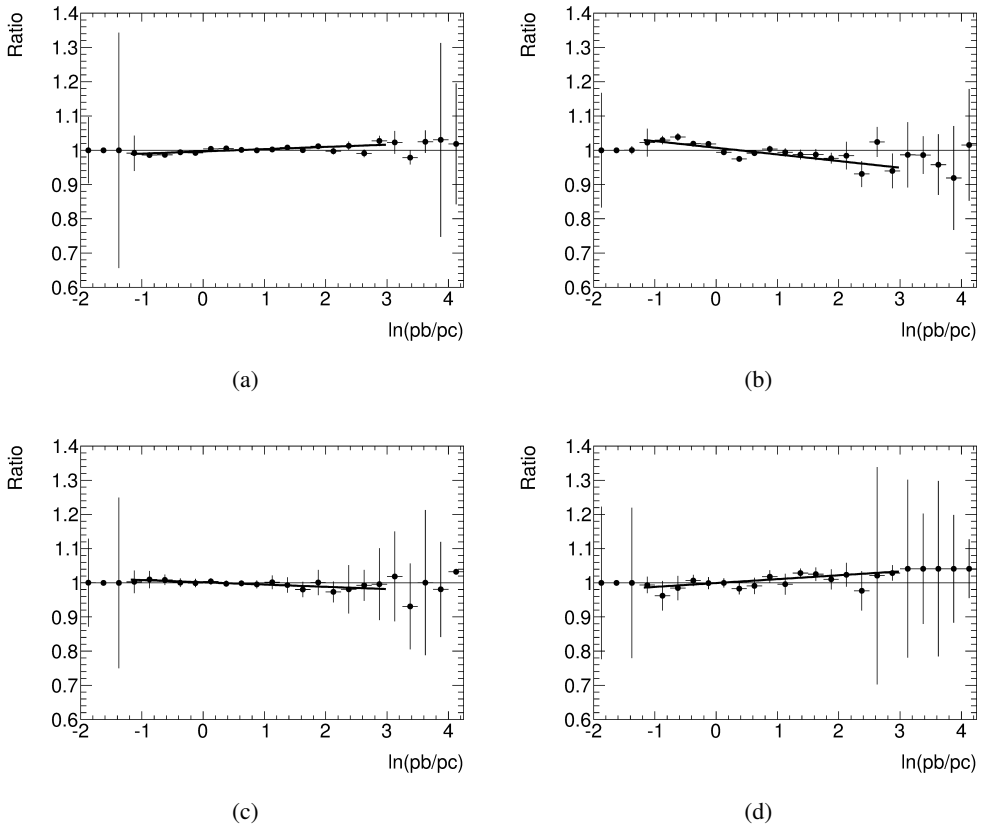

Figure 58: Ratio of charm template with scaled (a) D^+, (b) D^0, (c) D_s and (d) charm baryon fractions to default charm template